NOVEL PHOTOCATALYST OXIDE NANOSTRUCTURES ENGINEERED BY OBLIQUE ANGLE AND GLANCING ANGLE DEPOSITION

by

WILSON SMITH

(Under the Direction of Yiping Zhao)

ABSTRACT

This thesis reports on fundamental aspects of TiO_2 photocatalysis for water purification and water splitting to create hydrogen as an alternative fuel source. Although TiO_2 becomes active only under UV illumination, when coupled with WO_3 the photoactivation can be shifted to the visible region, and photocatalytic performance can be increased due to a charge-separation effect. Our approach has been unique in creating single-layer (TiO_2) and two-layer (TiO_2/WO_3) nanostructures that are uniform and easily reproducible utilizing oblique angle deposition (OAD) and glancing angle deposition (GLAD).

An experimental relationship was developed between TiO_2 surface area and its photocatalytic performance by using OAD to fabricate uniform arrays of TiO_2 nanorods with varying nanorod length. The experimental results showed a direct correlation between the surface area and photodecay rate, and a theoretical first-order reaction model was developed that agreed well with our results.

Using consecutive OAD and GLAD depositions, a series of two layer TiO_2/WO_3 nanostructures were fabricated and their photocatalytic performance was measured. The performance of the two-layer nanostructures was found to depend on the photocatalyst surface

area, the relative crystal structure of each material, and the interfacial area between the TiO_2 and WO_3 layers. The interfacial area between TiO_2 and WO_3 can be maximized by utilizing a modified GLAD technique to create core-shell nanorods, which has shown significant photocatalytic enhancement under UV and visible irradiation.

TiO_2 is also used in photoelectrochemical cells (PECs) to photo-dissociate water for hydrogen production. TiO_2 nanorods have been fabricated by OAD and shown the ability to split water at an applied overpotential of 1.0 V, with photoresponse beginning at λ = 400 nm. In addition, TiO_2/WO_3 core-shell nanorods are utilized in this PEC system and have the ability to dissociate water and create photocurrent with no applied overpotential, and shown a photoresponse out to λ = 600 nm.

In summary, TiO_2 and WO_3 nanostructures fabricated by OAD and GLAD have shown promising results for effective water photo-dissociation and photocatalytic reactions. The unique properties of these nanostructures have great potential for further improvement.

INDEX WORDS: oblique angle deposition, glancing angle deposition, dynamic shadowing growth, nanorod, photocatalyst, electron-hole pair, water photo-dissociation, electronic band structure, photodegradation, core-shell

NOVEL PHOTOCATALYST OXIDE NANOSTRUCTURES ENGINEERED BY OBLIQUE ANGLE AND GLANCING ANGLE DEPOSITION

by

WILSON SMITH

B.S., American University, 2005

A Dissertation Submitted to the Graduate Faculty of the University of Georgia in Partial Fulfillment of the Requirements for the Degree

DOCTOR OF PHILOSOPHY

ATHENS, GEORGIA

2010

NOVEL PHOTOCATALYST OXIDE NANOSTRUCTURES ENGINEERED BY OBLIQUE ANGLE AND GLANCING ANGLE DEPOSITION

by

WILSON SMITH

Major Professor: Yiping Zhao

Committee: Uwe Happek
Jason Locklin
Zhengwei Pan
Susanne Ullrich

Electronic Version Approved:

Maureen Grasso
Dean of the Graduate School
The University of Georgia
May 2010

DEDICATION

This thesis is dedicated to my soon-to-be wife, Lindsey Brooke Walker. None of this work would be possible without her love, support, and understanding during the course of my research.

ACKNOWLEDGEMENTS

I would like to take this opportunity to thank my research advisor, Dr. Yiping Zhao, for all of his support and encouragement throughout the past 5 years. He has led by example with his strong work ethic and success in the lab.

I would also like to thank my labmates John Gibbs, Justin Abell, Yonjun Liu, Yuping He, and Whitney Ingram, who over the past years have helped keep me sane with their conversations and discussions relating to my life inside and out of the lab.

TABLE OF CONTENTS

Page

LIST OF TABLES

Page

LIST OF FIGURES

Page

CHAPTER 1

INTRODUCTION

1.1 Fundamentals of Photocatalysis

1.1.1 Photocatalytic Principles

Photocatalysis is the process where a catalyst induces a chemical reaction at its surface initiated by the absorption of light. Photocatalytic materials can be used to remove harmful toxins from water and air, and also be used as a source of renewable clean energy. This process is governed by the material properties of the photocatalysts, the incident light intensity and frequency, and the specific chemical processes of the catalytic reaction. Photocatalytic materials possess unique structural, optical, and electronic properties that can be exploited for numerous applications, and have been studied extensively for decades. The performance of photocatalysts is governed by several fundamental principles and materials parameters that can drastically alter the performance of the materials, such as the electronic band gap, electron-hole pair generation and recombination dynamics, and the transportation of photogenerated charges. Understanding these parameters individually and how they can be controlled is vital in designing improved and optimized photocatalysts, which can perform more efficiently and effectively than traditional materials. The primary applications of photocatalysis can be summarized into two major categories; (1) photodegradation of organic materials dissolved in water (or another liquid) and (2) photoelectrochemical water dissociation.

The photodegradation of organic material has been studied extensively for the past few decades and has been an effective means to remove contaminant/pollutant material from water or other liquids using light. These reactions begin with a photocatalyst absorbing light, which creates electron-hole pairs within the material. Both of these charge carriers can diffuse to the photocatalyst surface where they can break down organic materials over time. The most prominent material used in these photocatalytic reactions has been TiO_2, due to its non-toxicity, relative abundance, optical properties, and stability in aqueous solutions. However, the most useful light available to perform these photodegradations has typically been UV light which is harmful and dangerous to use, and not very abundant in the solar spectrum. In addition, TiO_2 by itself can only reach a certain photocatalytic efficiency due to its large band gap energy. Currently, there are many research efforts exploring ways to improve the efficiency of photocatalytic materials such as TiO_2 by combining them with other semiconductors or metals to improve the lifetime of the photoexcited electrons and holes, as well as increasing the spectral absorbance range to include visible light. In addition to photodegradations, photocatalytic materials have shown the ability to split water via photolysis in electrochemical cells.

The splitting of water with sunlight to produce hydrogen is one of the most attractive forms of energy production, since both water and sunlight are vastly abundant. Solar harvesting devices such as photoelectrochemical (PEC) cells[5, 6] can be an important source of sustainable alternative energy for the hydrogen economy, and are essential to decreasing the consumption of fossil fuels. The overall water splitting reaction that occurs in a PEC cell is as follows,

$$H_2O + h\nu \rightarrow \tfrac{1}{2}\, O_2(g) + H_2(g) \quad . \tag{1.1}$$

where $h\nu$ is the energy of the incident photon. A diagram of a typical PEC set-up is shown in Figure 1.1.

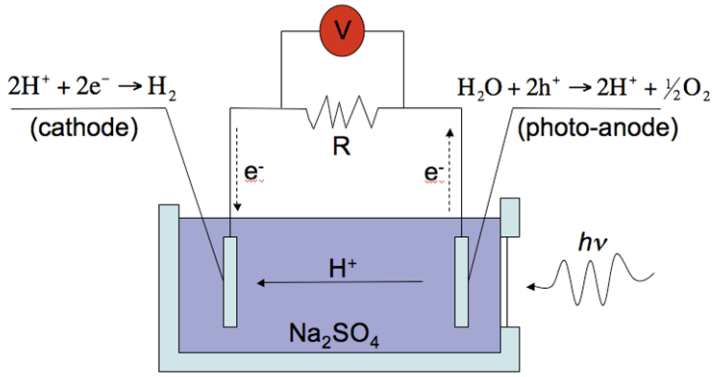

$$H_2O + h\nu \rightarrow \frac{1}{2}O_2 + H_2$$

Figure 1.1 A typical photoelectochemical cell (PEC), including a photo-anode, a cathode, electrolytic solution, and external current carrying pathway

The electrolysis of water is composed of a complicated series of steps that involves current flowing though an electrolytic solution comprised of water and a charge carrying solute. Traditionally, PEC cells are constructed in order to contain all the components to split water including a photoanode, a cathode, an electrolyte solution, and a load for the current to flow across. The first study of photoelectrochemical water splitting on TiO_2 was reported by Fujishima and Honda in 1972[6] and the details of which have been delved into extensively since then.[7-9] Metal oxides such as TiO_2, ZnO and WO_3 have all been investigated for water splitting with various film morphologies and efficiencies typically less than 1%.[10-16] A major obstacle in the use of metal oxides in general is their inherent large bandgaps and lack of absorption in the visible portion of the light spectrum.

The principles that govern the photodegradation of pollutants in aqueous solutions and electrochemical water splitting are the mostly same. They include the generation of photoinduced charges, light, and surface reactions. The differences are that the photocatalytic degradations are localized to the surface of the photocatalyst, while the photoelectrocehmical

water splitting reactions transport photogenerated electrons from the photocatalyst to an anode material to complete the re-dox reactions.

1.2 Charge Dynamics

1.2.1 Electron-Hole Pair Generation

The first process involved in photocatalysis is the absorption of light by a photocatalyst material. The basic principle of the photocatalyst is to use photogenerated charge carriers for chemical reactions, so the process of how the photocarriers are generated is very important. The absorption of light is directly dependent on the band gap of the photocatalyst, which can be explained by the band theory of solids.[1] The band theory classifies materials by their band gap, which is the energy difference between the valence band and conduction band electron orbitals. The valence band is also referred to as the highest occupied molecular orbital (HOMO), which is the highest orbital that an electron is naturally found in a material, while the conduction band is also referred to as the lowest unoccupied molecular orbit (LUMO), because it is the next stable electron orbit that is not already occupied by an electron. The band structures for an insulator, a semiconductor, and a metal are shown in Figure. 1.2 to detail the different electronic structures for these distinctively different materials.

Insulators are characterized by their traditionally large band gaps, which are what give them their intrinsic properties of having poor electron mobility, since the conduction band and valence band are relatively far apart and thus require a large amount of energy to transfer the electrons between bands. Semiconductors have a discrete band gap that is typically much smaller than that of insulators, but is still well defined. Metals have no band gap, but instead have a continuous series of electronic bands throughout the material.

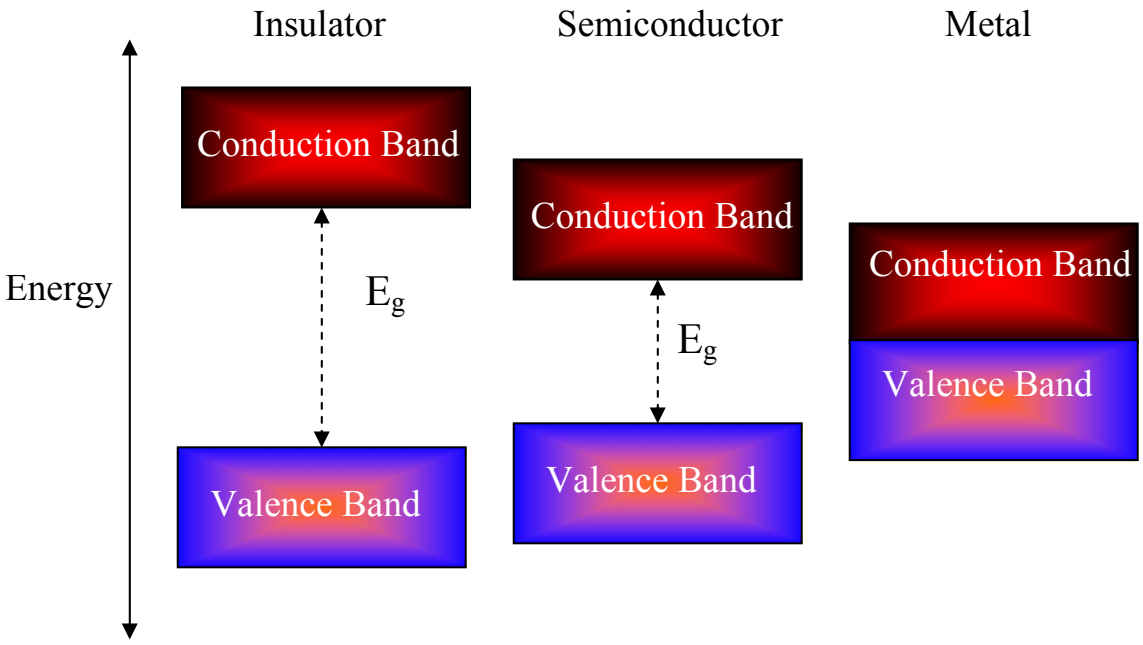

Figure 1.2 Band structure diagram for an insulator, semiconductor and metal.

This continuum of electronic bands give metals their intrinsic properties of being excellent electronic conductors, because the conduction and valence bands are so close that electrons are free to move between bands with little to no energy needed.

Another similar and helpful way to characterize different electronic materials is through a description of their Fermi energy level, E_F. For a semiconductor in thermal equilibrium at absolute zero, the Fermi level is defined as the highest filled level of electrons in the ground state. At some finite temperature above this, the electrons gain kinetic energy and can be excited into states above the Fermi level, leaving available openings below that energy. The discrete energy level above the Fermi level is the conduction band, and the discrete energy level below the Fermi level is the valence band. The forbidden zone of energy in between the bands is the band gap, which is where the Fermi level is found in thermal equilibrium for a pure solid.

In order for an electron to be promoted from the valence band to the conduction band level for semiconductors and insulators, it needs to be excited either thermally, electronically, or optically. Here, we focus on the electronic transition, which for our case is initiated by incident photons. If a photon with energy greater than or equal to the band gap energy of a material is incident on its surface, an electron in the valence band could absorb this photon and could be excited to the conduction band discretely and become a photocarrier. The energy level transition for an electron is governed by Fermi's golden rule, which is a useful way to calculate the transition rate from one energy state to another due to a perturbation, which in our case is photon absorption. The transition rate constant can be calculated by the following equation,

$$W_{i\to f} = \frac{2\pi}{\hbar}\left|\langle f|H'|i\rangle\right|^2 g(h\upsilon) \quad , \tag{1.2}$$

where h is Planck's constant, $\langle f|H'|i\rangle$ is the matrix element for the perturbation H' between the final, f, and initial, i, states, and $g(h\upsilon)$ is the density of electron states in the valence and conduction bands. For photoexcitation, the perturbation is the incident light with frequency υ, where the electron in the initial state can only be excited by the energy equivalent to $h\upsilon$, which is the band gap energy. If the frequency of the incident light is below υ, the electron remains in the valence band.

In an ideal material with no defects, this is the only possible transition for the electron starting in the ground state. For example, with TiO_2, the bulk band gap energy in the anatase phase is E_g = 3.2 eV (E_g = 3.05 eV for the rutile phase), which is the energy between the valence band (corresponding to the Ti 3d orbital), and the conduction band (corresponding to the O 2p orbital).[23] The energy E_g = 3.2 eV corresponds to a wavelength of λ = 388 nm, which is in the UV region of light. UV light has been used extensively to excite TiO_2 to generate photocarriers.

When an electron is electronically excited from the valence band to the conduction band, it leaves behind a positively charged hole that is also mobile and can move throughout the bulk or surface of a material similar to the way electrons can move around the conduction band. Both the electron and hole are used to induce the chemical reactions at the surface of the semiconductor material. Traditionally, the holes act as an oxidizing agent while the electrons act as reducing agents at the surface of the material. Because the electron-hole pair is very active and initiates most of the reactions on the photocatalysts surface, it is beneficial to have a high concentration of these charge carriers, and to also keep them apart for an extended period of time.

The rate of generation of electron hole pairs in a material also depends directly on how much light can be absorbed from a macroscopic point of view, whereas earlier we looked at the generation rate from a quantum mechanical point of view with Fermi's golden rule. The absorbance can be calculated by measuring the intensity of light before and after hitting a material using beer's law, which states,

$$I = I_o e^{-\alpha x} \quad , \tag{1.3}$$

where I is the light intensity at any position, x, defined as the thickness away from the incident interface, α is the absorption coefficient, and I_o is the incident light intensity, or intensity at the top of the surface. The above equation could be used to directly estimate the number of electron-hole pairs being generated in a semiconductor that is illuminated at or above its band gap energy. This can be estimated by assuming that the loss in the intensity of light, (I - I_o) is due to only the absorption of the material, and thus the generation of electron-hole pairs. If this is the case, then the generation rate, G, of electron hole pairs can be estimated at a thickness x from the surface of the material to be,

$$G = \alpha N_o (1\text{-}e^{-\alpha x}) \quad , \tag{1.4}$$

where N_o is the photon flux at the surface of the semiconductor. The importance of these relationships are that they reveal the exponential decrease in light intensity, and thus the generation rate, is a function of the thickness of the material, and how deep light can penetrate into a material. This means that more electron hole-pairs are created closer to the surface of the material than in the bulk. This also implies that there may be a critical thickness of a photocatalyst that the incident light will not reach into, and is thus more or less negligible. It is important to note that these assumptions are for pure generation here in an ideal material, and do not take into effect doping and lattice defects, and impurity states. This information can be used to directly design photocatalysts that minimize useless material, which can decrease the amount of photocatalytic materials needed, and thus minimize cost and improve efficiency.

1.2.2 Electron-Hole Pair Recombination Pathways

Photo-excited electron-hole pairs that are created within a semiconductor have a finite lifetime while they are apart from each other before recombining. From the previous section, we assume that one photon will create one electron-hole pair, so that during the entire generation and recombination processes there is no net gain or loss of charge carriers. Regardless of the overall efficiency of the generation process, recombination effectively limits the activity and power of both charge carriers since the photogenerated carriers will be directly involved with catalytic reactions, so it is advantageous to keep the pair apart for as long as possible. Within the bulk structure of a semiconductor, the predominant mechanism for recombination is a non-radiative form of band-to-band recombination that allows the excited electron in the conduction band to transmit back down to the valence band, thus eliminating an electron-hole pair. For the

system to reach equilibrium, we will assume that the rate of generation will equal the rate of recombination, or $G = R$, where G is the rate of electron-hole pair generation and R is the rate of electron-hole pair recombination. This steady-state relationship can hold true for pure materials with no defects or trap states to impede the recombination process, and can be further described by using Einstein coefficients for simplicity.

Einstein coefficients can be used to describe the three sources of spectral lines resulting from absorption, stimulated emission, and spontaneous emission in an atomic system. The absorption process has been described in detail in the above section. Spontaneous emission is the process of an excited electron decays from a higher energy state in the conduction band to a lower energy state in the valence band without any perturbation and is represented by the coefficient A. Stimulated emission, represented by the coefficient B, is a process where an electron in an excited state, or in the conduction band, is stimulated by an incident photon such that the electron decays into a lower energy level, with two photons exiting the system as a result. Einstein developed a direct relationship between the spontaneous and stimulated emission rates in thermal equilibrium that can be expressed as,

$$\frac{A}{B} = \frac{8\pi h \nu^3}{c^3} \quad , \tag{1.5}$$

where ν is the electron frequency and c is the speed of light in a vacuum. Thermal equilibrium can only be achieved if the ratio of A and B equal the above value, which implies that a population inversion between the two energy bands, such as that in a laser, cannot be achieved. The stimulated emission rate is directly related to the absorption, and equilibrium is only reached when the excitation equals the relaxation.

For both stimulated emission and spontaneous emission, the recombination process is a direct recombination between the conduction and valence energy bands. However, if a material

does not have a perfect or uniform lattice and has defects due to impurities, trap states can exist within the band gap that provide stable energy levels for both electrons and holes. The trap states offer several complicated recombination pathways that can be explained by the Shockley-Read-Hall model. [24,25] For the Shockley-Read-Hall (SRH) model, there are four different pathways the excited charge carriers can be captured within the forbidden band gap zone that are different than the traditional-band to-band recombination, and are shown in Figure 1.3.

The first pathway traps photoexcited electrons that are located in the conduction band and relax into a trap state within the band gap. This process is called electron capture. If the initial electron in the valence band is excited with light at or above the band gap energy, the electron will be promoted to the conduction band, where instead of recombining with its hole counterpart in the valence band again, it will move to a semi-stable location within the band gap. This energy level is situated within the band gap, and its exact energy is related to the nature of the defect or impurity within the material lattice. Once in this trapped state, the electron can then relax back into the valence band and combine with the photogenerated hole that it initially left behind.

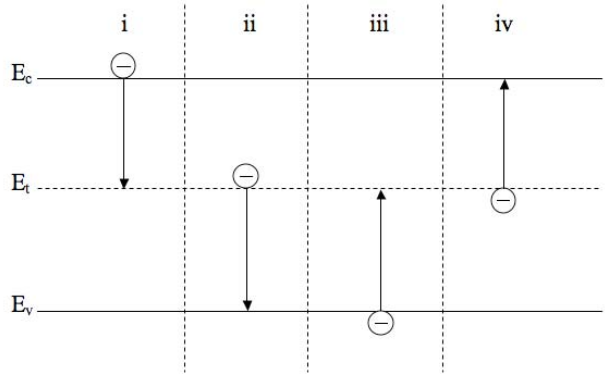

Figure 1.3 Visualization of the four recombination pathways as described by the Shockley-Reed-Hall model including, (i) electron capture, (ii) hole capture, (iii) hole emission, and (iv) electron emission, where the conduction band level is given by E_c, the trap energy level is given by E_t, and the valence band energy is given by E_v.

This process is called hole capture. The change in the energy of the electron is smaller than that when an electron typically recombines from the conduction band to the valence band.

The third process in the Shockley-Reed-Hall model, called hole emission, occurs when an electron is excited with light having an energy less than the band gap energy, and is directly promoted from the valence band to a trapped state within the band gap. For this to happen effectively, the electron will have to be excited by light that is lower than the band gap energy, but higher than the energy level of the trap state. If the incident light energy is less than that of the trap state, then the electron will remain in the valence band. The last Shockley-Reed-Hall process, called electron emission, occurs when an electron in the trapped state is excited by light that is equal to or greater than the difference between the trapped energy state and the conduction band level. In this case, the electron is promoted to the conduction band, where it stays for a short period of time before either being trapped again in the trapped state, or recombining in a band-to-band transition in the valence band. The electron lifetime in the trapped state is very short, (1~100 ns), so the incident light energy needed for this process has to be almost immediate or concurrent with the initial hole emission process.

If we examine the time constants for the various recombination processes, it is easier to see the relationship the impurity levels have compared to the direct band recombination process. If we still assume that the generation rate is equal to the recombination rate for each recombination process (the semi-equilibrium condition), we can evaluate several interesting factors. For direct recombination, the recombination rate can be expressed as $R = N_c / \tau_D$, where N_c is the number of photogenerated electrons that are in the conduction band, and τ_D is the recombination time for a direct recombination process. Similarly, we can evaluate the recombination rates and constants for the trap states. However, it is very difficult to estimate the

overall lifetime of the recombination process while taking into account the Shockley-Reed-Hall recombination because the number of conduction band electrons, valence band electrons and holes, and density of the trap states would need to be known. Each of the four processes has a characteristic lifetime that is governed by the density of states in each energy level that is part of the transition. Therefore the overall recombination rate and lifetime of each particular state is hard to determine because the density of states for three levels needs to be known, and the addition of the four Shockley-Reed-Hall recombination to the absorption and direct recombination processes combine to make seven different forms of interband transitions that need to be accounted for.

1.2.3 Charge Separation

When electron-hole pairs are generated by photoexcitation, they are typically separated for a finite and pre-determined amount of time that is an intrinsic property of the material, and crystalline structure of the material that is being excited. The primary mechanism for describing charge separation is a variation of Fermi's golden rule, as described earlier in this chapter. In particular, we are concerned with the forward and back transition rates for electrons going to and from the conduction and valence energy bands, described by the equations,

$$k_f(r) = W_f e^{\left[(R_f - r)/a_f\right]} \quad , \tag{1.6}$$

and,

$$k_b(r) = W_b e^{\left[(R_b - r)/a_b\right]} \quad , \tag{1.7}$$

where the subscripts *f* and *r* denote the forward and back processes, *k* is the transition rate, *W* is the transition probability determined by Fermi's golden rule, *r* is the interparticle distance, and *R* and *a* are constants used to parameterize the distance scales of each transition and fall-off of the

electronic wave function of the states, respectively. These forward and back transition rates can help to determine the probability of finding an electron or hole in a particular state via the following relationships,

$$\frac{dp}{dt} = k_f(r)n_f(r,t) - k_b(r)p(r,t) \ , \tag{1.8}$$

and,

$$\frac{dn}{dt} = -k_b(r)n_b(r,t) \ \ , \tag{1.9}$$

where p is the probability of finding a hole, n is the probability of finding an electron. From these relationships we can see two trends. First, for the change in the probability of finding a hole is dependent on both the forward and backward transitions. This makes sense because the holes are only produced via excitation (the forward reaction), and are then consumed by the backward reaction (recombination). The other trend is for the change in the probability of finding an electron in a given state, which is dependent only on the back reaction kinetics. Again, this makes sense because unlike the photogenereated holes, the electrons are present at all times within the material. The dependence on the back reaction relates to the lifetime of both the electron and holes, because the rate that the electrons fall back to the initial state will determine the annihilation the holes.

Since the photogenerated holes (and sometimes electrons) are the predominant driving mechanism in photocatalysis, it is advantageous to keep the charges separated for as long as possible. While the intrinsic recombination time, τ, is determined by the crystal structure of a material, there are several ways to increase the recombination time by changing the material properties, and adding other semiconductors or metals to the primary material. This process is called charge separation.

Charge separation initially occurs by photoexcitation, but can be extended by creating hetero-junctions between two materials. For instance, in a TiO_2-Ag system, electrons can be excited via photon absorption in TiO_2, and then transferred to Ag due to the difference in Fermi energy levels between the semiconductor and the metal. The difference in the Fermi energy levels and the vacuum energy level characterizes the work function for each material, and is equivalent to an electric potential. The contact between the two materials creates a junction, called a Shottky barrier, where there is an appreciable difference in Fermi energy levels, and thus a difference in the work functions. The difference in the work functions creates an effective electric field that drives electrions toward the metal, and holes toward the semiconductor creating an effective charge separation. Similarly, if another semiconductor is combined with TiO_2 the differences in each material Fermi level creates an electric field due to the different work functions, and also creates an effective charge separation. Using a two-semiconductor system requires the second material to have a higher work function, and thus a lower Fermi energy level than the first material, so each must be chosen carefully to satisfy these conditions.

A pictorial representation of the band structure of a single photoactive material as well as a two types of hetero-structures, two semiconductors and one semiconductor and one metal, are shown in Figure 1.4, below. Assuming that the TiO_2 is in a stable crystal phase with a well-defined band gap, the amount of defect states within the band gap will be very small. This leaves the primary charge carrier movements to be the excitation, or generation, and the band-to-band recombination. However, if we add another semiconductor, such as WO_3, to the TiO_2, it is possible to keep the charges apart for a longer amount of time. In order for this effect to happen, the band structure of the secondary semiconductor needs to be close to the primary material, but have a different Fermi energy level.

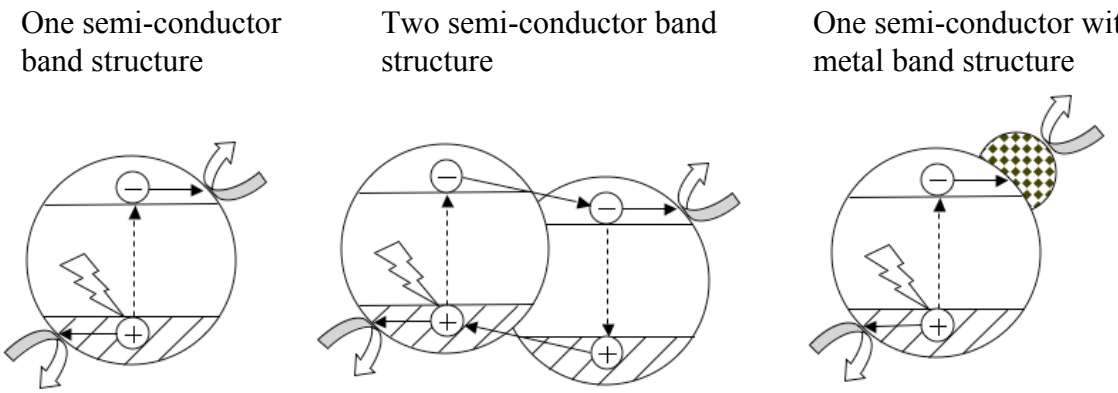

Figure 1.4 Electronic band structure for a single semiconductor, a two semiconductor system, and a semiconductor combined with a metal.

Specifically, the Fermi energy level of the secondary material needs to be slightly lower than that of the primary material, so that there is a difference in work functions at the junction between the two materials to create an effective electric field. When this is the case, photoexcited electrons in the conduction band of the first material have the ability to transfer to the conduction band of the secondary material. This pulls the electrons away form the primary material, and keeps the photogenerated holes free for a longer amount of time to continue breaking down reactants, and improve photocatalytic performance. A similar explanation can be used to explain a metal-semiconductor system.

The above mentioned situations apply to binary systems that are created with two materials in direct contact with each other, such as TiO_2 coated with Ag nanoparticles, or with WO_3. However, effective charge separation can also be achieved through the lattice doping within TiO_2. For example, when TiO_2 is prepared in the amorphous state, it has shown poor photocatalytic activity. This can be explained by the electronic and optical properties of amorphous materials, which dictate that they have no defined band gap. That means that there can be several valence and conduction band energies, with no preference or higher density of one

state of energies. This, in effect, creates defect energy levels within a defined band gap, so that electrons can be promoted and recombine at several energy levels. With several stable energy levels that are very close together, photoexctied electron-hole pairs are given many opportunities to recombine, and have a shorter distance, or lower amount of energy, to travel to do so. However, when TiO_2 is prepared in the anatase, or even rutile phase, the photocatalytic performance has shown significant enhancement. The reduction of defects allows the electron-hole pairs to stay apart for a longer time than if there were defect. While the reduction of defects can remove recombination and trap centers within the band gap, the electron-hole lifetime is still governed by the energy separation of the band gap of TiO_2.

When selected atoms with different numbers of valence electrons or different bond strengths are intentionally placed within the lattice of TiO_2, called doping, it is also possible to increase the lifetime of photogenerated charge carriers. When TiO_2 is doped, electrons or holes may be free to move around more freely around the doped atoms than the native atoms, which can increase the amount of photogenerated charge carriers available for conduction. With doped atoms directly inserted into a host lattice, they create bonds with the host atoms, which have different strength than the initial homogeneous bonds. These new bonds can change the electron/hole conductivity drastically in a local space around the defects, and create a new distribution of electronic energy levels that can keep photogenerated charges apart from each other for a larger amount of time.

1.2.4 Charge Transport

Another important characteristic property that determines the performance of photocatalytic materials is the charge transport of photogenerated charge carriers throughout the

material. Since the photocatalytic reactions occur at the surface of the material, it is important for the photogenerated charges to be able to diffuse to the surface before recombining with each other. There are two important factors that can affect the transport of charge throughout a material. The first factor is the crystal structure of the material. If an electron-hole pair is created within the bulk of a material, it needs to travel to the surface to complete the chemical reaction. Its path from the bulk to the surface is much simpler and easier if the crystal structure of the material is uniform, so that the charge carriers can transfer throughout the lattice easier. The electron mobility is determined by their mean free path, which is larger in an ordered crystal lattice than a defect heavy lattice. This is made easier from a highly ordered crystalline material, because the crystal order correspond to stable and uniform energy levels surrounding each atom in the crystal lattice. This allows the photogenerated charge carriers to smoothly move from atom to atom by not having to change energy levels and gaining or losing energy. If the crystal structure of the material is not uniform, and has many defects, the mobile charge carriers can be trapped or recombine much more easily as they move throughout the crystal lattice. These unintended recombinations have been described above as the Shockley-Reed-Hall mechanics.

Another factors that can affect charge transport within a material is the morphology of the structure. For example, for a thin film, when electron-hole pairs are created within the bulk material, their motion is determined by a random-walk mechanism. This means that once the charge carriers are generated, they move randomly throughout the thin film, and have no preference to go to the surface, or be extracted in a photoelectrochemical cell. However, if the material is fabricated in a porous morphology, such as O-D or 1-D nanostructures, the charge transport can be improved. An additional issue for films with interconnected zero-dimensional (0-D) nanoparticles in charge transport, is often limited because of the lack of continuous

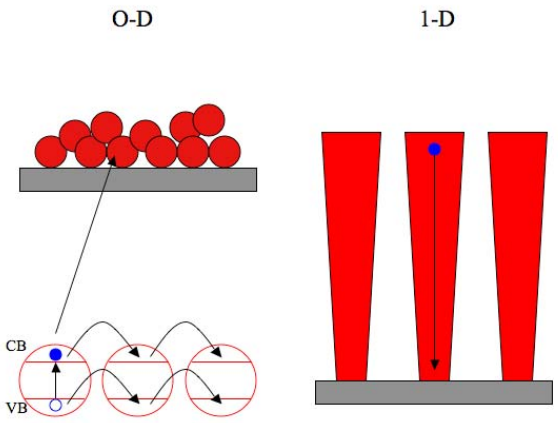

Figure 1.5 Schematic diagram for electron transport in 0-D and 1-D nanostructures

conducting pathways, with electrons moving by a hopping mechanism due to energy barriers between particles.[20]1-D nanostructures are expected to have improved charge transport properties compared to 0-D nanostructures[21-23] because of the direct conduction pathways in nanorods versus electron hopping in nanoparticle systems.[24,25] A representative scheme showing the electron mobility in 0-D and 1-D nanostructures is shown in Figure 1.5.

In a successful utilization of 1-D nanostructures, Paulose *et al*. demonstrated hydrogen generation utilizing 6 μm long TiO_2 nanotube arrays and attained a hydrogen rate of ~ 180 μLhr^{-1} via photolysis.[26] However, the use of 1-D metal oxide nanostructures as photoelectrodes in PEC for hydrogen generation is still limited and requires further research.

1.2.5 Surface Reactions

There are two predominant mechanisms that have been attributed to the photocatalytic degradation of organic materials at the surface of photocatalysts. The first is direct photo-hole oxidation. The pathway for this reaction is as follows; initially, photons absorbed by a

photocatalyst, such as TiO_2, and the electrons in the valence band are excited to the conduction band,

$$TiO_2 + h\nu \rightarrow e^- + h^+ \quad , \tag{1.10}$$

where $h\nu$ is the incident photon energy, e^- is the photogenerated electron, and h^+ is the photogenerated hole. After the electron pair is created, the electrons and holes are effectively separated, and the holes migrate to the surface of the photocatalyst. At the surface, they can directly oxidize organic material,

$$h^+ + R \rightarrow R^+ \quad , \tag{1.11}$$

or,

$$h^+ + R \rightarrow R^* \quad , \tag{1.12}$$

where R is the reactant, and R^+ and R^* are the subsequently formed products after the hole induced oxidation. While the photogenerated hole is in the conduction band, it is at a high enough energy level to break down certain reactants, and can do so directly before recombining with the electron back in the valence band. This scheme then implies that the larger surface area the photocatalyst has in contact with the reacting solution should increase the rate of photocatalytic activity, due to the increased amount of holes that can be found at the surface. On the photocatalyst side, the efficiency of the system depends on how many photogenerated holes can be generated, and then can reach the surface to breakdown the reactants. The electron/hole transport from the bulk of the material to the surface is determined by the purity of the lattice. If there are little to no defects in the crystal lattice, the photogenerated charges can drift to the surface relatively easy. However, if there are many defects or impurities the charge carriers have a greater chance of being trapped or recombining before reaching the surface, as discussed earlier.

Once the reactants are broken down, products are formed at the surface and can take away the valuable active surface area needed to continue the reaction effectively. Thus, another important factor in the photocatalyst efficiently breaking down reactants must deal directly with the diffusion of unreacted particles to the photocatalyst surface, as well as the diffusion of the reactant products away from the photocatalyst surface.

The other mechanism for photocatalysis still involves the photogenerated holes, but only in a secondary manner. This mechanism supposes that the holes break down water molecules into hydrogen (H^+) and hydroxy radicals (OH^*) as follows,

$$H_2O + h^+ \rightarrow H^+ + OH^* \quad . \tag{1.13}$$

From there, the hydroxyl radicals, which have a very high oxidation potential, can break down organic molecules,

$$OH^* + R \rightarrow OH + R^* \quad . \tag{1.14}$$

This reaction scheme is more complicated than the first and requires a two-step process to degrade the dissolved organic materials. While the first mechanism relies on the diffusion of the holes to the photocatalyst surface as well as the diffusion of the reactants to the surface and the products away from the surface, this second scheme has several more steps. The diffusion of the holes to the surface should be the same as the first scheme, since the photocatalyst is the same regardless of which reaction scheme we use. However, when the holes break down the water molecules into hydrogen and hydroxyl radicals, the radicals must then find the reactant molecules to break them down. Hydroxyl radicals are not very stable, and have relatively short lifetimes before forming more stable products such as water or hydrogen peroxide. This scheme requires that the radicals find a reactant molecule and break it down before they become stable themselves, which is a difficult and delicate process.

Both of these schemes have been used to describe the effect of active photocatalysts to breakdown organic materials at their surface. While the exact mechanism, or number of steps involved is different between the two schemes, there are some similarities that are apparent. Those similarities are that the reaction is driven primarily by the photogenerated holes, and the higher amount of surface area of the photocatalyst will allow for more holes to reach the surface and either directly breakdown the reactant, or break down water molecules to engage the degradation reactions. This information is vital for creating optimized photocatalysts that can take advantage of this mechanism, and a higher performance should be seen in samples with higher surface area.

1.3 Measuring Photoactivity

The direct photocatalytic activity of photocatalysts, such as TiO_2 is traditionally measured by observing the decay rate of some solute in an aqueous solution, or dissolved in another solvent. The most common way to measure this activity is through spectroscopy. Traditionally, the absorbance[23,24] or raman[25,26] spectra are taken of a solution containing the desired contaminant particles. Then, the photocatalyst material is placed within that solution, and irradiated by UV or visible light for regular time intervals, and the respective spectra are taken after each interval. When using absorbance or raman spectroscopy, there is usually a characteristic peak for the solute that will decrease over time during irradiations. The peak height is then plotted as a function of time, and fitting this curve can give a slope that can be interpreted as the decay rate of the solution. The direct derivation of this process for methylene blue (MB) will be described in detail in Chapter 2.

1.4 TiO_2 and WO_3 as Photocatalysts

Semiconductor materials have proven to be very active and reliable with numerous technological applications based on their unique electronic, optical, and structural properties. Among the most promising applications that have been studied with semiconductors is in the field of heterogeneous photocatalysis. Using semiconductors as active photocatalysts in heterogeneous reactions has shown immense promise for both environmental detoxification as well as for energy production. Among the most attractive and widely used semiconductors that have shown promise for these applications is titanium dioxide (TiO_2). TiO_2, or titania, is such an appealing material of choice because it is non-toxic, relatively abundant, non-corrosive in water, and has attractive optical and electrical properties. In addition to the beneficial material properties of titania, it has also shown to be useful in numerous applications including self-cleaning windows, an additive in sunscreen, water and air purification, and water splitting for the production of hydrogen to be used as a renewable energy. All of these applications require photo-excitation of TiO_2 to activate its photocatalytic properties. Typically, UV light has been used to excite the TiO_2 surface because it is easily absorbed by most of the existing TiO_2 materials. However, UV light is harmful to humans, and is not readily abundant in the solar spectrum which is mainly comprised of visible and IR light, so it is not a suitable choice for the long-term use of TiO_2. Therefore, significant research has been conducted to change the optical properties of TiO_2 to try and have it absorb and react under visible light, which is not harmful to humans, as well as making the material more active under less powerful UV light. In addition, TiO_2 can be combined with many different materials, particularly other semiconductors and metals, to enhance the photocatalytic activity due to a charge separation effect.

The initial photo-induced water splitting reaction by TiO_2 was observed by Fujishima and Honda in 1972,[1] which began the study of TiO_2 as active photocatalyst. This pioneering experiment initiated the interest in the fundamental research for the mechanisms of the photoactiviation of semi-conductors, the photo-oxidation and photo-reduction of adsorbates, and the resulting product formation. The applications of TiO_2 have grown immensely during this time, with devices including TiO_2-coated self-cleaning building materials including ceramic tiles, glass windows, textiles, and aluminum siding, as well as photocatalytic air cleaners.[2] Due to the strong applicability of TiO_2 based materials, the technology and fundamental understanding of the photocatalytic reactions is necessary to improve on the existing technology and elucidate the photocatalytic mechanisms that give TiO_2 its unique power.

1.5 Ways to Improve Photocatalytic Performance

TiO_2 and WO_3 have been used as active photocatalysts in water splitting and water purification reactions extensively, as discussed earlier in this chapter, and the methods for fabricating various TiO_2 and WO_3 structures are just as extensive as their applications. Traditionally, TiO_2 has been fabricated via physical and chemical techniques, including sol-gel, hydrothermal, combustion synthesis, electrochemical synthesis, physical vapor deposition, chemical vapor deposition, and spray pyrolysis.[42,45] While these techniques are diverse and can create a series of TiO_2 structures, they typically can be used to only manufacture thin films and particle aggregations. Among the micro and nano-porous samples that are fabricated, a common theme in the literature is that the increase in photoactivity in nanostructured photocatalysts is much greater compared to the bulk materials. However, TiO_2 by itself can only reach a certain level of photocatalytic efficiency due to the quick recombination of the photo-

generated electron-hole pairs. It has been shown that the photocatalytic efficiency of TiO_2 can be improved by reducing defects, increasing surface area, and extending the lifetime of electron-hole pairs. When TiO_2 is prepared by physical vapor deposition (PVD) methods or other methods, it may be in the amorphous phase and has many structural defects. Those defects form trapped states that could reduce the lifetime of the photogenerated electron-hole pairs, thus deteriorating the photocatalytic activity. By annealing TiO_2 at temperatures above 200 °C, the crystal structure changes from amorphous to anatase, and the number of defect sites is reduced, thus helping to improve the photocatalytic efficiency.[43,44] In addition, photocatalytic effects always occur at the surface of the photocatalytic materials. For example, both hydrogen generation from water splitting and the decomposition of organic dyes in aqueous solutions occur at the solid-liquid interface between TiO_2 and the solution.[47,48] By increasing the surface area of TiO_2 via porous structures, more photogenerated electrons or holes can be in contact with the reactants, thus the photocatalytic efficiency will also increase.

While these aforementioned fabrication techniques can accurately produce samples repeatedly for photocatalyst materials, the studies examining the activity do not allow for a detailed and systematic study for the increase in photocatalytic activity, and only suggest the increase is a result of an increase in the photocatalyst surface area. The main problem with these techniques is that random aggregations of nanoparticles clump together and form very complicated pathways and overlap frequently. This makes it extremely hard to calculate the exact surface area between the photocatalyst and the solution it is submersed in. Also, the porous channels between nanoparticles create very windy pathways for the solution and products to move through, so it may make the diffusion of the reactants and products to move to and from

the photocatalyst surface, which could also affect the performance, and measurement of performance for these materials.

To further improve the photocatalytic performance, combining TiO_2 with another semiconductor with a similar position in their conduction bands or metal nanoparticles, can produce a so-called charge separation effect to extend the lifetime of the electron-hole pairs, as discussed earlier,[49,50] This is possible because the photo-generated electrons that are excited to the conduction band in the first material, can move to the conduction band of the second material and delay the recombination with the photo-generated holes. Typically metals such as Ag, Au, and Pt have been used to scavenge photo-generated electrons and have shown significant charge-separation enhancement,[51,52] The most common method to prepare these structures is to coat the TiO_2 layer with metal nanoparticles on top,[53,54] and this metal nanoparticle surface coverage reduces the surface area between TiO_2 and the liquid, which then decreases the area of the catalytically active sites. TiO_2/WO_3 coupled structures are one such composition that holds great promise,[55,56] since WO_3 (E_g = 2.8 eV) has a similar conduction band level to TiO_2 (E_g = 3.2 eV) . Several methods have been used to create these combo-structures such as ball milling,[57] hydrothermal synthesis,[58] and sol-gel processing,[59] These methods produce a random mixture of TiO_2 and WO_3 nanoparticles. Although these structures have improved the overall photocatalytic behavior, due to the small band gap of WO_3, and the randomness of the particle orientations, the optical absorbance efficiency of the structure is not optimized. It has been reported by Miyauchi *et al*. that by having TiO_2 facing the incident UV-light instead of WO_3 leads to enhanced photocatalysis.[22] This is because the addition of the WO_3 layer causes the charge-separation in TiO_2, and results in more electrons accumulating in the WO_3 layer, and more holes accumulating in the TiO_2 layer. This enhances the

photocatalytic properties because the holes in the TiO_2 layer have a strong oxidation potential and can breakdown the organic material adsorbed on the surface, so with a surplus of holes accumulating in the TiO_2 layer, this leads to an overall enhancement of its photo-degradation abilities. It has also been reported by Irie *et al*. that the interfacial area between the TiO_2 layer and WO_3 layer plays an important role in charge separation, and thus affecting the photocatalytic activity.[23] By increasing the contact area between the TiO_2 and WO_3 surfaces, more separated electron-hole pairs can stay open longer due to the charge separation effect. In addition, the crystal phase of both the TiO_2 and WO_3 layers play an important role in the overall photocatalytic performance. Higashimoto *et al.* has reported that a two-layer TiO_2/WO_3 system yields higher efficiency in photo-electrochemical experiments with the TiO_2 layer being crystalline and the WO_3 phase being amorphous than with both layers being crystalline.[24,25] The explanation for this effect is that the amorphous WO_3 has its conduction band level closer to that of TiO_2, and thus allows for easier charge-carrier transfer. It is expected that by combining the large surface and interfacial area, proper crystalline structure, and ordered layer structure, one could greatly enhance the photocatalytic activity. However, the current nanofabrication techniques can only partially meet those requirements.

While TiO_2/WO_3 nanostructures have been fabricated and studied in some detail, there are two major problems that impede the progress of their research. The major reason is that the traditional fabrication methods do not allow for a great deal of flexibility in the morphological combination of materials. This is detrimental for understanding the physical and chemical pathways that enhance photocatalysis with heterostructured systems, since it is hard to accurately estimate structural parameters such as the active surface area and the interfacial area between materials. In addition, due to the rigid nature of many of the fabrication techniques, it is hard to

control the heterojunctions between materials, in terms of interfacial area, thickness, and uniformity. These parameters are vital to control in order to theoretically explain the photocatalytic phenomenon as well as experimentally devise a systematic series of experiments to vary individual morphological/structural parameters that could shed light on the fundamental mechanisms for improved photocatalysis. Due to these reasons, a robust fabrication technique is required in order to carefully control the morphology of the individual materials, as well as give control to the structural properties of multi-layered nanostructures in order to investigate the delicate effects of hetero-nanophotocatalysts, and build a complete model to explain the phenomenon.

1.6 Oblique Angle Deposition and Glancing Angle Deposition

Although wet chemistry methods have been very popular in creating TiO_2 based photocatalysts, physical vapor deposition (PVD) methods have also received attention recently. Of the several PVD methods, electron beam evaporation and sputtering depositions have been the most popular in creating nanostructured TiO_2. While these methods do give increased control over the morphology of nanostructured films, the studies of these samples has not focused on the exact photocatalytic mechanism, nor have they built a direct relationship between the morphology and the photocatalytic response. For example, Zywitzki et. al. created various TiO_2 nanostructures by a sputtering deposition method, and found that as the morphology of the samples changed so did the photocatalytic activity.[23] This study measured the photocatalytic decay of MB over the surface of TiO_2 and how the different morphologies reacted differently with the solution. One important conclusion was that the anatase phase TiO_2 performed better than the rutile phase TiO_2 due to the different band gap energies and band level positions.

However, they did not measure the specific surface area of the different samples made at different pressures, and did not directly correlate the increase in surface area to the increase in photocatalytic activity.

Therefore, a more robust method for fabricating TiO_2 nanostructures is needed in order to create systematically different structures whose surface area and photocatalytic activity can be precisely measured to make a strong correlation between the two. One such method is oblique angle deposition (OAD). OAD is a modified PVD technique that can be implemented on almost any PVD system with a simple modification of the substrate holder. When the substrate is positioned so that its surface normal is parallel with the evaporation direction, a uniform thin film is formed across the surface. However, by positioning the substrate holder at a large angle ($\theta < 70^o$) with respect to the evaporation direction, a thin film is not formed. Instead, the initial molecules from the evaporation source hit the substrate surface at random spots, and form small nucleation islands. These initial growth spots act as shadowing centers for the further deposition material, and effectively block a small area behind them due to a geometric shadowing effect, shown in Figure 1.6.

The initial islands act as growth centers for the resulting deposition, and over time these islands form into column-like shapes that grow along a specific direction, or angle (β) from the substrate that is a function of the incident vapor deposition angle (α), also shown in Figure 2.1. The porosity of the nanorod array, as well of the density and diameter of the nanorods can be changed by varying the incident vapor angle, while the length of the nanorods can be controlled by increasing or decreasing the deposition time.

If the substrate is kept at a constant angle and is not rotated during an OAD deposition, the nanorod array will be formed tilted in the direction of the incident vapor.

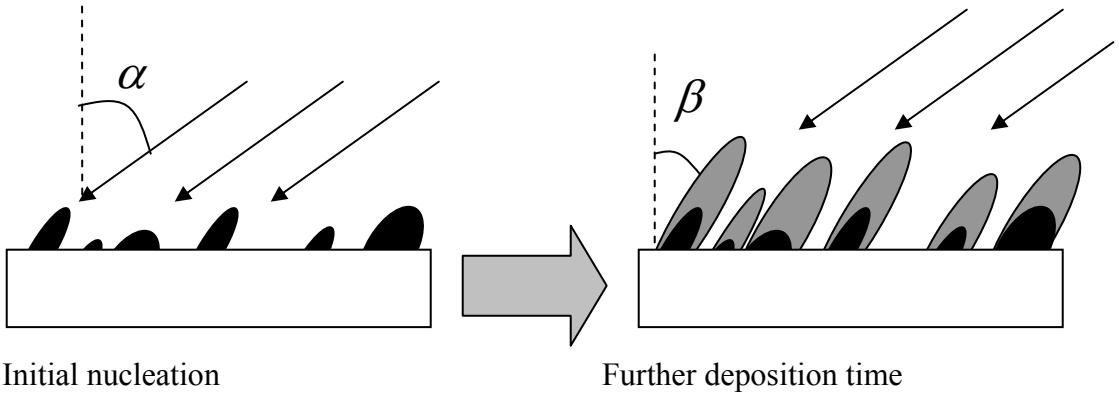

Figure 1.6 A schematic diagram of the initial growth mechanism of OAD fabrication.

However, if the substrate is rotated at a constant rate during the deposition, the nanorod array created can be aligned vertically, and this technique is called glancing angle deposition, or GLAD.GLAD utilizes the shadowing mechanism of OAD, but when the substrate is rotated azimuthally the incident vapor hits all the sides of the initial nucleation island, and vertical posts are formed (Figure 1.7). The density and porosity of the nanorod array can be controlled by varying the rotation speed of the substrate, as well as the diameter of the individual nanorods. Furthermore, hierarchal structures can be created such as zigzag, helical, and spring structures by carefully controlling the substrate rotation direction and frequency. For example, making successive OAD depositions after rotating the substrate in 90^{o} increments will create a step like structure that looks like a boxy helix, whereas a slow, constant rotation speed can make a smooth winding spiral structure.

In addition to the freedom that OAD and GLAD give in controlling the morphology of nanostructures, another major advantage is that these techniques can be applied to several materials in succession, creating multi-layered structures.

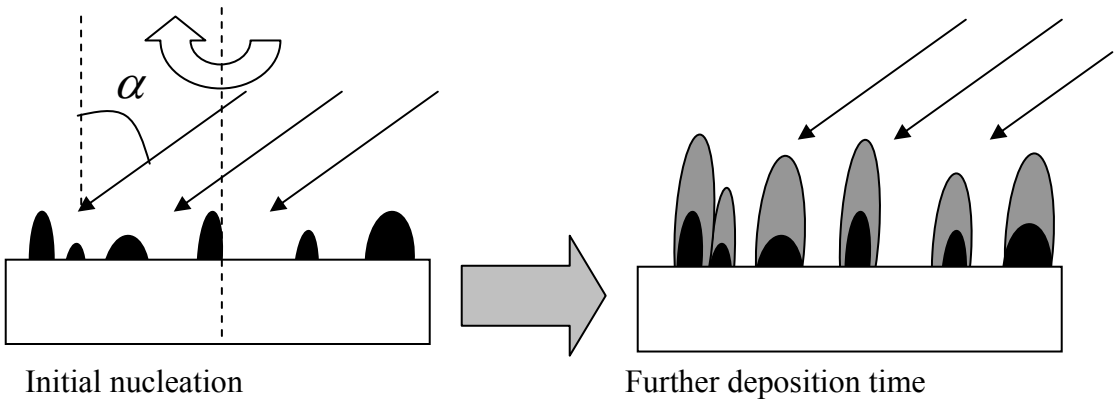

Figure 1.7 A schematic diagram of the initial growth mechanism of GLAD fabrication.

By simply depositing one material directly following the deposition of another material, a hetero-structure can be formed whose morphology is dependent on the individual parameters of the sequential depositions. For example, Figure 1.8 shows a cross-sectional SEM image of a WO_3 OAD and GLAD nanorod arrays deposited on top of a TiO_2 OAD and GLAD nanorod arrays, with the same incident vapor direction, $\alpha = 86^o$.

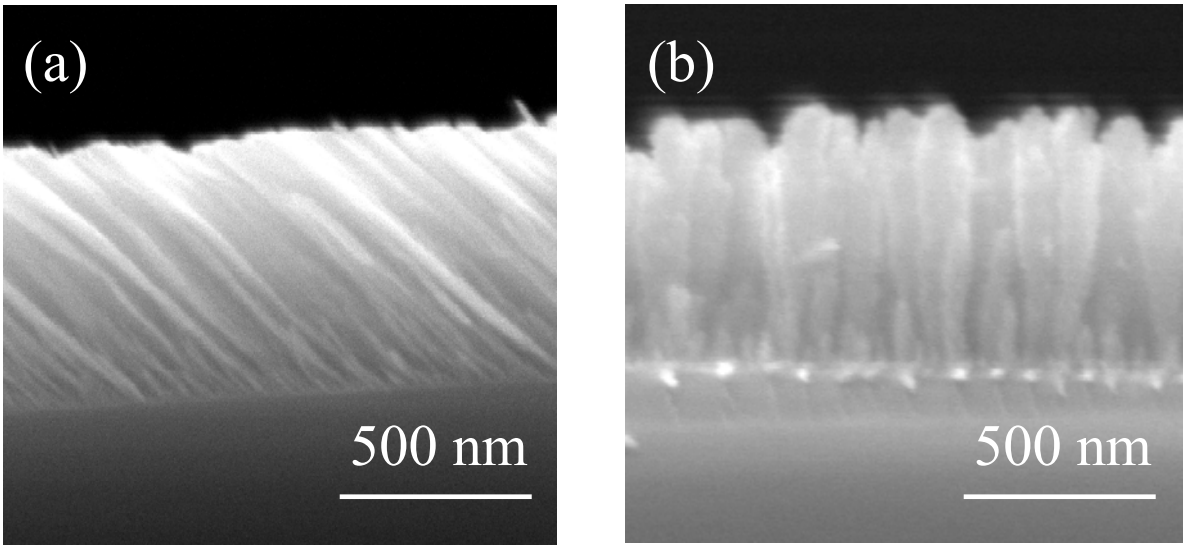

Figure 1.8. Cross-sectional SEM image of (a) a two-layer OAD nanorod structure. TiO_2 was deposited first, and compromises the bottom half of the nanorod array, and WO_3 was deposited second and makes up the top half of the nanorod array, and (b) a two-layer GLAD nanorod structure made with identical deposition conditions.

1.7 Conclusions

In summary, TiO_2 nanostructures have shown an excellent ability to degrade organic material dissolved in water, and effectively split water into hydrogen and oxygen due to its unique photocatalytic properties. While TiO_2 has proven to be an effective photocatalyst by itself, when combined with metals and other semiconductors, its photocatalytic performance can be enhanced by a charge separation effect, that keeps photogenerated electrons and holes apart for a longer than normal time. There are several fabrication techniques that have created TiO_2 and TiO_2-metal/TiO_2-semiconductor nanostructures, but most of these techniques do not offer a reasonable degree of flexibility in controlling individual structural parameters. Utilizing oblique angle deposition and glancing angle deposition techniques, it is possible to create well-aligned arrays of nanostructures whose morphological and structural properties can be easily controlled, so as to maximize the beneficial properties of TiO_2 and its heterostructured binary materials.

CHAPTER 2

PHOTOCATALYSIS OVER TiO_2 NANOSTRUCTURES

2.1 Introduction

Utilizing OAD and GLAD to create TiO_2 nanostructures for photocatalytic reactions is not a new idea. In fact, Suzuki et. al. fabricated TiO_2 nanorods arrays and studied the effect of changing the deposition parameters had on their photocatalytic properties.[33] That group created tilted nanorods arrays using OAD, and varied the substrate deposition angle for successive nanorod arrays, as well as creating hierarchal structures such as zig-zag nanorods and nano-helixes. By testing the photocatalytic properties of each sample created, they found that the optimal photocatalytic activity was found for the OAD samples fabricated at a deposition angle of $\alpha = 70^{o}$. The analysis of these results inferred that the improvement in photocatalytic activity was due in part to the increased porosity of those samples, though a rigorous or detailed correlation was not given. In this chapter, our aim to fabricate a series of TiO_2 nanostructures including thin films, OAD, and GLAD nanorods, and compare their photocatalytic behavior to their structural and morphological properties. Furthermore, we aim to create a series of OAD nanorods that keep the deposition angle constant, and vary the time of deposition, and thus the length of the nanorods. Then, we will carryout photodegradation experiments on each sample, and try to establish a direct relationship between the surface area and structure of the TiO_2 nanostructures and their photocatalytic performance. Lastly, we will look at the dependence of

the photocatalytic decay rate on the intensity of incident UV light using a series of identical TiO_2 nanostructures.

2.2 Experimental Methods

TiO_2 nanostructures were fabricated in a custom-built electron beam evaporation system (Torr International, New Windsor, NY). The source material used to deposit was TiO_2 (99.99%, Kurt J. Lesker) with no other gases present in the chamber during depositions. Prior to depositing, the chamber was evacuated to a background pressure of $1\sim2 \times 10^{-6}$ Torr. Cleaned Si (100) wafers were used for SEM and morphological characterization, while cleaned glass slides were used for the photocatalytic experiments. Substrates of both materials were cut into 9.0×30.0 mm^2 rectangular shapes before being placed on the substrate holder. For thin film depositions, the substrate normal was positioned parallel with the incident vapor flux. For OAD depositions, the substrate was positioned at an angle of 86^o with respect to the vapor incident direction for depositions. For GLAD depositions, the substrate was again positioned at 86^o with respect to the incident vapor direction, and the substrate was rotated azimuthally at a constant speed of 0.5 rev/sec. The growth rate and thickness of the depositions were monitored by a quartz crystal microbalance (QCM) directly facing the incident vapor flux direction. For the first study comparing the thin films, OAD, and GLAD nanostructures, the deposition rate was fixed at 0.4 nm/s, and depositions were made until the QCM thickness reached 500 nm. For each of the OAD length dependent depositions, the rate was fixed 0.4 nm/s and depositions were made for samples with QCM thickness readings of d = 1.0 μm, 1.5 μm, 2.0 μm, 2.5 μm, 3.0 μm, 3.5 μm, 4.0 μm, 5.0 μm, respectively. For the light intensity dependent experiments, OAD nanorods were fabricated uniformly, with a fixed deposition rate of 0.4 nm/sec, and a QCM thickness of 1

μm. After the depositions, all of the samples were annealed at 500°C for 2 hours in air to obtain the anatase crystal phase, which is well known to maximize photocatalytic reactions (15,16 in paper). The morphology of the samples was characterized by a field-emission scanning electron microscope (SEM, FEI Inspect F). To test the photocatalytic performance of each sample, the annealed substrates were placed into a clear methacrylate cuvette with dimensions 10 × 10 × 45 mm^3 filled with approximately 4.0 ml of an aqueous solution (65 μM) of methylene blue dye (MB:$C_{16}H_{18}ClN_3S$, Alfa Aesar). The samples were then irradiated by a UV-lamp (UVP LLC, Model B-100AP, ~10 mW/cm^2 power) emitting a maximum intensity at λ = 366 nm, for 20 minute intervals with the same illumination area of 270 mm^2. The optical absorbance of the MB solution at different irradiation intervals was measured by a UV-Vis spectrophotometer (JASCO V-570), and the absorbance at λ = 664 nm for the MB solution was used as a measurement for photodegradation.

2.3 Photodegradation Behavior of TiO_2 Nanostructures

The morphological properties of the TiO_2 thin film, OAD and GLAD samples were measured and compared to each other. The deposition parameters for each nanostructure fixed the QCM thickness reading to 500 nm, so that the amount of deposited material would be the same for each sample. To determine the actual thickness of each sample, SEM measurements were taken, and the cross-sectional SEM images of the thin film, OAD, and GLAD nanostructures are shown in Figure 2.1.

The thin film of TiO_2 was found to be approximately 500 ± 15 nm thick. The OAD TiO_2 samples had an estimated density of $\eta \cong 30 \pm 5$ rods/μm^2, an average vertical thickness of $h \approx$ 500 ± 25 nm, an average diameter of $D = 40 \pm 10$ nm, and a tilting angle $\beta = 50^o$. The surface

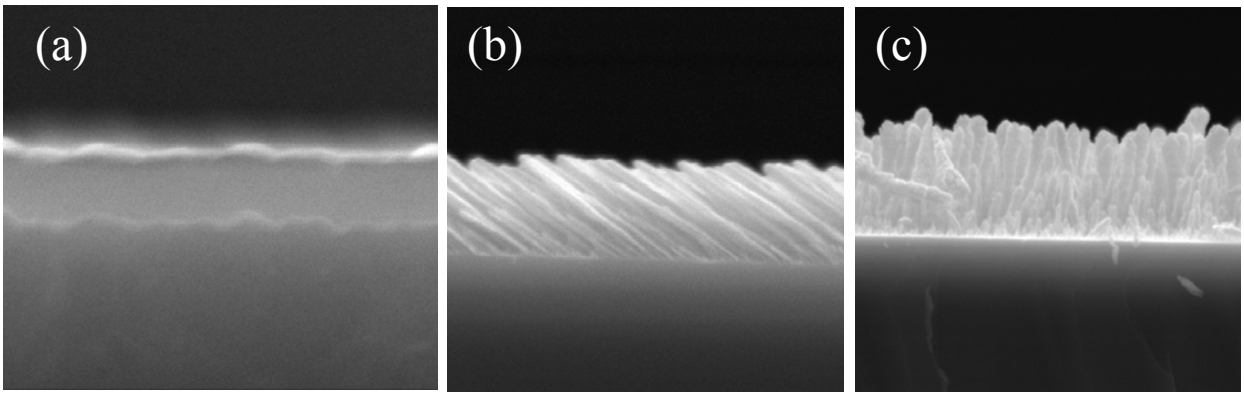

Figure 2.1 Cross-sectional SEM image of (a) a TiO_2 thin film, (b) a TiO_2 OAD nanorod array, and (c) a TiO_2 GLAD nanorod array.

area for this nanorod array is 3 times the projected area. The GLAD TiO_2 nanorod array had an estimated density of $\eta \cong 10$ rods/μm^2, an average length of $l = 400 \pm 20$ nm and an average diameter on top of $D = 65$ nm. The surface area is estimated to be roughly 2 times the projected area. To determine the photocatalytic performance of each nanostructured sample, the normalized absorbance peak ($\alpha(\tau)/\alpha(0)$) at $\lambda = 664$ nm for MB was measured at different time intervals after UV irradiation. After the UV irradiation, a photodegraded sample was left out in the open air and in darkness, and its absorbance was measured for several hours. No absorbance peak emerged, confirming that we had completely and irreversibly decomposed the MB molecules, and did not reduce it to its leuco-methylene blue (LMB) form. For all the samples, as the irradiation time increases, the absorbance for the MB decreases. However, the rate of the decay is different for different samples. The decay rate was estimated by fitting the absorbance versus time curve with a first-order decay rate equation,

$$\alpha(\tau)/\alpha(0) = e^{-\kappa t} \quad , \tag{2.1}$$

where $\alpha(t)$ and $\alpha(0)$ are the absorbance at time t, and $t = 0$, and κ is the photodecay rate. The photodecay rate, k, in Table I for the TiO_2 single layer structures has exhibited two trends.

The first trend that is present in the above table is the surface area effect. With increasing surface area of the TiO_2 samples by making the thin film samples more porous with OAD or GLAD, the decay rate is also found to increase, confirming our earlier predictions. The decay rate for the as-deposited TiO_2 thin film sample was estimated to be $\kappa = 6.15\times10^{-5}$ min^{-1}. The OAD sample had a decay rate of $\kappa = 6.47\times10^{-4}$ min^{-1}, which is about 10 times higher than that for the thin film. The GLAD sample had a decay rate of $\kappa = 4.33\times10^{-4}$ min^{-1}, which is about 7 times larger than the thin film sample. The increase in photo-degradation rate for as-deposited sample is found to be proportional to the increase in surface area for the nanorod structures, i.e. 3-fold for the OAD samples and 1.8-fold for the GLAD samples.

The second trend is the effect of the annealing. Each sample was annealed at 2 different temperatures, and their crystal structure was measured by XRD to confirm the structure, shown in Figure 2.2. The trend for each sample is very similar. The as-deposited samples for each morphology showed no crystalline peaks, confirming their amorphous structure. However after annealing each sample at 300°C and 400°C, sharp peaks arose that corresponded to the anatase phase of TiO_2. The samples annealed at 400°C showed slightly higher peaks than at 300°C, showing that the samples were in a more uniform crystal phase at the higher temperature.

Table 2.1 shows that for different morphologies of TiO_2, the photo-degradation decay rates increase with increasing annealing temperature. The samples annealed at $T_a = 300$ °C have a higher decay rate than the as-deposited samples, and the gains are proportional to the increase in surface area. For the OAD sample annealed at $T_a = 300$ °C, the OAD rate is 2.5 times the rate for the thin film sample, with a surface area roughly 3 times that of the thin film. For the GLAD sample annealed at $T_a = 300$ °C, the decay rate is 2.0 times the rate for the thin film, with a surface area approximately 1.8 times as large.

Table 2.1 Comparison of the decay rate for TiO_2 nanostructures annealed at different temperatures

		As-deposited	**T_a = 300°C**	**T_a = 400°C**
Single layer samples	Thin Film	6.15×10^{-5} min^{-1}	3.22×10^{-4} min^{-1}	3.25×10^{-3} min^{-1}
	OAD	6.47×10^{-4} min^{-1}	8.08×10^{-4} min^{-1}	3.34×10^{-3} min^{-1}
	GLAD	4.33×10^{-4} min^{-1}	6.75×10^{-4} min^{-1}	1.80×10^{-3} min^{-1}

The samples annealed at T_a = 400 °C have a higher decay rate than the samples annealed at T_a = 300 °C. However, this annealing temperature effect is not proportional to the surface area. The degradation rate of the thin film after annealing at T_a = 400 °C is comparable to that of the OAD nanorods annealed at the same temperature, and is even larger than that of GLAD nanorods. Clearly, after annealing, the crystalline structure of the TiO_2, rather than the surface area, plays the dominant role for determining the decay rate. The amount of crystalline phase changes from amorphous to anatase in OAD and GLAD nanorods are significantly less than that in the thin film, which causes the fast increase in decay rate for thin film sample.

2.4 TiO_2 OAD Nanorod Photocatalysis: Morphology Dependence

One of the most critical components in establishing a fundamental aspect of TiO_2 photocatalysis, is to rigorously find a relationship between the surface area of TiO_2 nanorods with their photocatalytic behavior. This can be achieved only if it is possible is to accurately estimate the precise surface area for each nanorod array. In order to calculate the effective surface area of each sample, SEM images were used to calculate the average density, length, and diameter of the nanorod arrays. Representative SEM images of a short TiO_2 nanorod array (d = 1 μm), and the longest sample (d = 5 μm) are shown in Figure 2.2.(a) and (b), respectively.

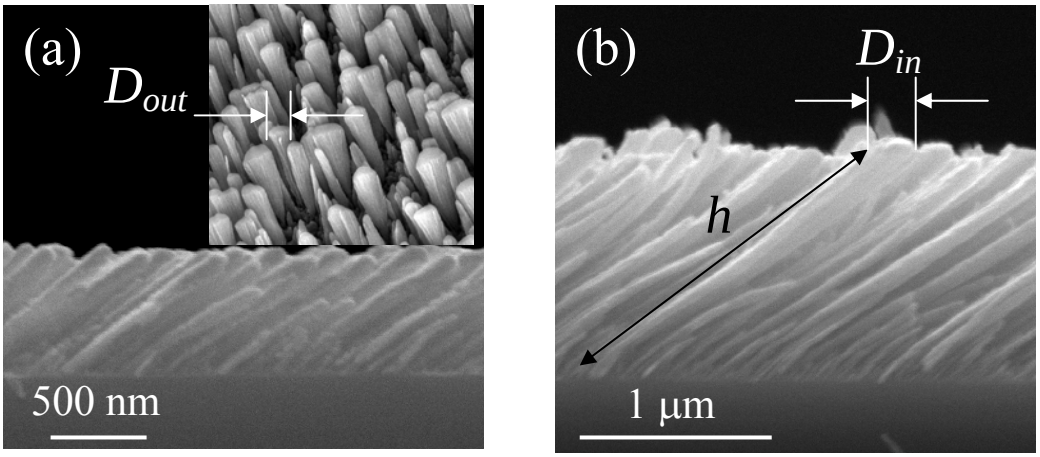

Figure 2.2 Cross-sectional SEM images of the TiO_2 nanorod arrays with (a) d = 1 μm, and (b) d = 5 μm. The inset in (a) is the top-view SEM image of the nanorod array.

From these images we can estimate the average length h, in-plane diameter D_{in}, out-of-plane diameter D_{out}, the nanorod tilting angle β with respect to the surface normal, and the density η of the nanorod arrays. We observed that as the length of the nanorod increases, so do the in-plane and out-of-plane diameters.

However, the diameter of the nanorods does not grow circularly or uniformly, rather they grow more elliptically. Here, we define the diameter of the nanorod parallel to the incident vapor plane as D_{in}, and the diameter in the perpendicular direction as D_{out}. D_{in} can be measured from the cross-sectional SEM images, while D_{out} can be measured from the top-view SEM images, as shown in Fig. 2.2. For example, the nanorods with d = 1 μm (Fig 2.1 (a)) have an actual length h = 750 ± 40 nm, with D_{in} = 80 ± 5 nm and D_{out} = 190 ± 50 nm at the top, which is indicative of the so called fan-out effect that has been reported for several OAD fabricated nanorod arrays.[17] The nanorods deposited with length d = 5 μm (Fig 2.1 (b)), have an actual length h = 2.5 ± 0.1 μm, with D_{in} = 150 ± 7 nm and D_{out} = 420 ± 200 nm at the top. The diameter at the bottom, D_B, is consistent for all the samples, with an average value D_B = 40 ± 5

nm (we could not measure D_B in the out-of-plane direction due to the SEM measurement configuration), and we assume it is the same for both the in-plane and out-of-plane directions. In addition, the tilting angle β for all the samples does not change, and is estimated as $\beta = 44^o \pm 2^o$.

The trend of the diameter increasing as the length of the nanorods also increased was evident for all 8 substrates that were fabricated. Figure 2.3 (a) shows a log-log plot of the length of the nanorods, h, versus the in-plane diameter, D_{in}, and out-of-plane diameter, D_{out}, for all the samples. The overall trend shows that both the in-plane and out-of-plane diameters grow as the length of the nanorods increases, and they obey a power law $D_{in,out} \propto h^{Pin,Pout}$, where the scaling exponents $p_{in} = 0.58 \pm 0.06$ and $p_{out} = 0.6 \pm 0.4$. These values for the scaling exponents are very close to the average value, $p = 0.5$ reported by Karabacak et. al.,[18] It is interesting to note two things about the in-plane and out-of-plane diameters found at different nanorod heights. First, the diameter in the out-of-plane direction, D_{out}, is generally larger than the in-plane diameter, D_{in}. This tendency reveals that there is significantly more mobility of the deposited TiO_2 atoms perpendicular to the evaporation direction after hitting the nanorod surface.

Another trend to note is the range of the diameters in each direction, where D_{out} has a much larger variance than D_{in}. This implies that there is more mobility for the deposited atoms in the horizontal direction than in the in-plane direction during OAD depositions for TiO_2.
While the diameter does not increase as a function of height uniformly, i.e. D_{in} does not equal D_{out} at a given height, it is useful to calculate the circumference, C, as a function of the nanorod height in order to get a better estimate of the overall surface area of the nanorod array. We can calculate the circumference $C \approx 2\pi\sqrt{\frac{D_{in}^2 + D_{out}^2}{2}}$ in relation to the in-plane and out-of-plane diameters, which is in the form of the generalized circumference for an oval. In Figure 2.3 (b), we plot the circumference as a function of the nanorod height, and find another power law

scaling relationship, $C \propto h^p$, where $p = 0.6 \pm 0.3$. If we know the height of an individual nanorod, this relationship can help us to calculate the actual surface area of a given rod.

In order to estimate the surface area of the whole nanorod array, the density of nanorods per unit area is also needed. Using the top-view SEM images of each nanorod array, the density was calculated, and the density at different nanorod heights is also plotted in Figure 2.3 (b). The

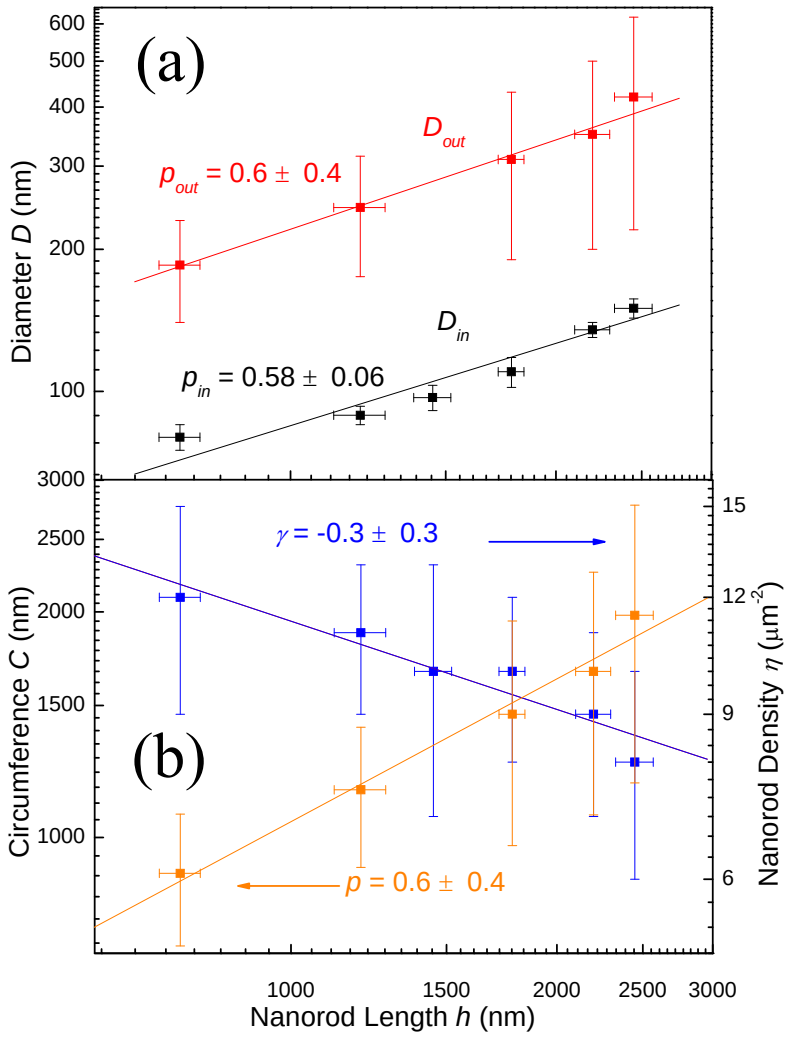

Figure 2.3 The log-log plots of (a) the in-plane diameter D_{in} and the out-of-plane diameter D_{out} versus the nanorod length h and (b) the circumference of the nanorods C and density η of the nanorod array versus the nanorod length h. They all obey power laws.

density, η, was found to decrease as the nanorod length increased due to the naturally competing growth of nanorods by the shadowing effect, and the density scaled in a power law fashion with the nanorod length $\eta \propto h^{\gamma}$, where γ = -0.3 ± 0.3 is the scaling exponent. Therefore, knowing how many nanorods are in a given projected area, and the surface area of an average single nanorod, it is possible to estimate the effective surface area of TiO_2 deposited by OAD on a substrate with a known nanorod length.

The UV-Vis absorbance spectra were measured for all of the samples with different nanorod lengths, and are shown in Figure 2.4. The shape of the spectra stays almost the same for nanorod arrays with different lengths, which means the overall spectral response of the samples is the same, and the absorption edge begins around λ = 400 nm. The absorbance in the wavelength region λ > 320 nm increases with the nanorod length. To better see this trend, the absorbance at a fixed wavelength, λ = 366 nm, is plotted as a function of the thickness, t (t = $h\cos\beta$), of the nanorod samples and is shown in the inset of Fig. 2.3.

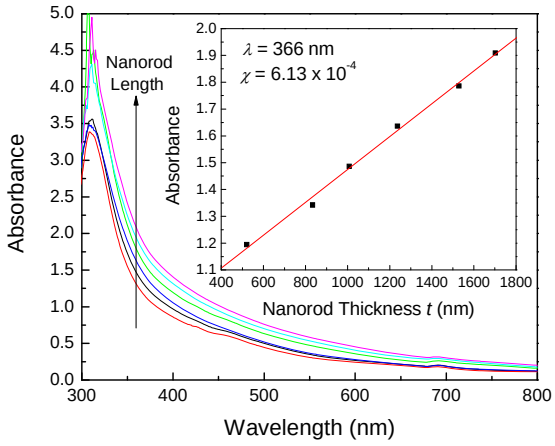

Figure 2.4 The optical absorbance spectra for the nanorod arrays with length h = 750 nm, 1200 nm, 1450 nm, 1780 nm, 2200 nm, and 2500 nm. The inset of this figure shows the absorbance value for each nanorod array at λ = 366 nm as a function of the nanorod thickness.

The absorbance of the nanorod samples at λ = 366 nm shows a linear increase with the nanorod thickness, and we obtain the absorption coefficient, χ, to be $\chi = 6.13 \times 10^{-4}$ nm^{-1}. The small absorption coefficient and the small thickness of the nanorod samples (t < 1700 nm) imply that the nanorod samples absorb the 366 nm UV light uniformly across the entire layer

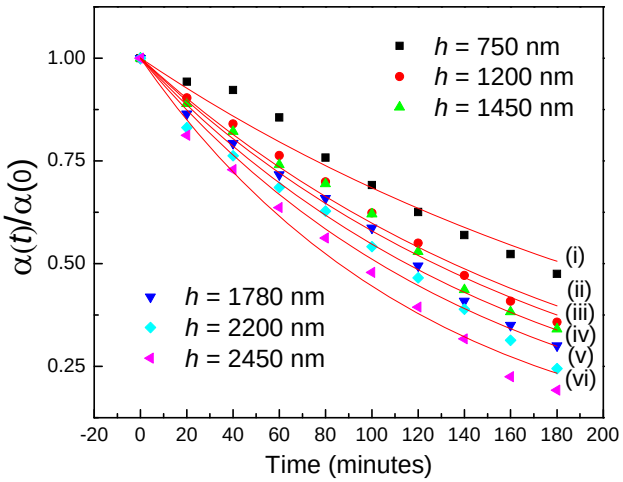

Figure 2.5 The plot of the normalized absorbance peak $\alpha(\tau)/\alpha(0)$ of MB at λ = 664 nm for all samples with different nanorod lengths.

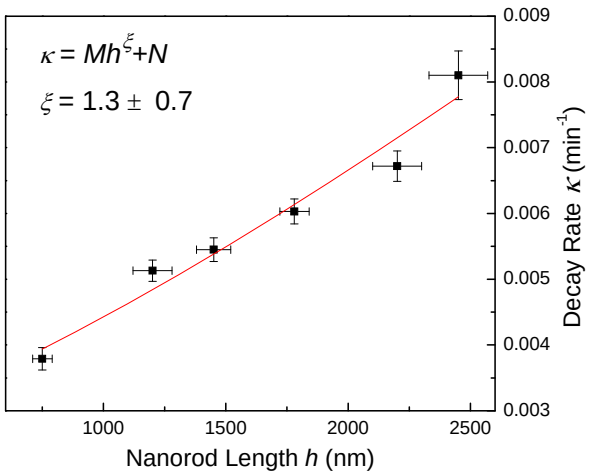

Figure 2.6 A plot of the photodecay rate κ versus nanorod length h, fit with the equation $\kappa \propto Mh^{\xi}+N$.

In addition to the morphological and optical characterization of TiO_2 OAD nanorod arrays, the photocatalytic performance of each array was tested and compared to each other. The decay rate κ versus the nanorod length h is plotted in Figure 2.5. This figure shows that as the nanorod length increases, the photodegradation of MB occurs faster, and the normalized absorbance is lower at longer nanorod lengths.

2.5 Modeling the Photodecay Rates for TiO_2 Nanorod Arrays

To quantify this relationship between the nanorod length and the photodecay rate, the decay rate was plotted against the nanorod length in Figure 2.6, and a simplified first order equation was used to fit the data. The photodecay rate increases monotonically with the nanorod length, and can be fit with a power law, $\kappa \propto Mh^{\xi} + N$, where $M = 1.9 \times 10^{-6}$, $N = 0.002$, and $\xi = 1.0 \pm 0.5$. It is interesting to explore the photodecay mechanism to see whether this scaling behavior is linked directly to the morphological scaling of the TiO_2 nanorods.

For the photodegradation of MB, the most popular mechanism proposes that the incident UV-photons create electron-hole pairs in the TiO_2 nanorods that can decompose the water and create active oxygen radicals according to the following reaction,[19]

$$H_2O + 2h^+ \rightarrow 2H^+ + O \quad . \tag{2.2}$$

These oxygen radicals then breakdown the MB molecules through the following irreversible reaction,[20]

$$C_{16}H_{18}ClN_3S + 51O \rightarrow HCl + H_2SO_4 + 3HNO_3 + 6H_2O + 16CO_2 \quad . \tag{2.3}$$

This reaction is quite complicated, and is involved with many intermediate steps.[21] To simplify the photoreaction, we propose a phenomenological first-order reaction model (which also fits the experimental behavior) that directly links the hole concentration to the product,

$$MB + h^+ \rightarrow C \quad , \tag{2.4}$$

where MB is the reactant, and C is the product of the reaction. Here, we use a simplified first-order reaction model to interpret the photodegradation of MB. This assumption is based on the argument that the rate limiting step in MB photoreduction is controlled by the MB surface adsorption and the surface hole generation and transportation. During the overall photoreaction of MB, there are many intermediate reactions that take place with the photo-generated holes and electrons at the surface of the TiO_2 that involve MB and several intermediate products, as detailed by Housas et. al.[21] They argue that these intermidiate products do not cover a substantial enough area of the TiO_2 surface to cause a significant decrease in MB's ability to get to the surface. At low MB concentrations (they used 75 μM compared to our 65 μM), the MB adsportion onto the TiO_2 is one of the rate-limiting steps, and it follows the langmuir isothermal equation,[21] which is one of the assumptions we used. On the other hand, the photogeneration of electron-hole pairs is the other rate-limiting step. If we only consider these two rate limiting steps, and ignore the intermediate steps, we could use the above phenomenological first-order reaction equation to describe the photoreaction process in which a first-order time-dcay relationship can be obtained, which is consistent with most experimental observations.[22~24]

For this model, we assume that the concentration of MB molecules in the cuvette is [MB]. During the photoreaction, ΔN molecules of MB are broken down at the surface of the TiO_2 during a time interval, $\Delta\tau$. Thus the overall change in the concentration of the MB solution with time is given by,

$$\frac{d[\mathrm{MB}]}{d\tau} = \frac{-\Delta N}{V\Delta\tau} \quad , \tag{2.5}$$

where V is the total volume of the solution and stays constant throughout the reaction. The MB molecules are only consumed by the photocatalyst surface reaction according to Eq. (2.4), therefore at the TiO_2 surface, the change of the surface concentration of MB can be written as,

$$\frac{d[\mathrm{MB}]_s}{d\tau} = -\kappa_s \sigma_h \theta \quad , \tag{2.6}$$

where $[MB]_s$ is the surface concentration of MB at the TiO_2-solution interface, κ_s is the surface catalytic chemical reaction rate, σ_h is the effective surface concentration of photo-excited holes, and θ is the surface coverage of MB molecules. Due to the small absorbance and small thickness of the nanorod arrays as discussed in Fig. 2.4, we assume that the σ_h is independent of the nanorod height. The surface coverage, θ, can be assumed to follow the Langmuir-Hinshelwood isothermal equation,

$$\theta = \frac{k_\theta b[\mathrm{MB}]}{1 + b[\mathrm{MB}]} \quad , \tag{2.7}$$

where k_θ is the adsorption rate and b is an adsorption constant.[25,26] Under the assumption that $b[\mathrm{MB}] << 1$, the above expression can be simplified as,

$$\theta \approx k_\theta b[\mathrm{MB}] \quad . \tag{2.8}$$

Using this expression for the surface coverage, Eq. (2.3) can be simplified as,

$$\frac{d[\mathrm{MB}]_s}{d\tau} = -\kappa_s \sigma_h k_\theta b[\mathrm{MB}] \quad , \tag{2.9}$$

or,

$$\Delta[\mathrm{MB}]_s = -\kappa_s \sigma_h k_\theta b[\mathrm{MB}] \quad . \tag{2.10}$$

The number of reacted MB molecules ΔN is proportional to the TiO_2 surface area. Since the nanorod substrates do not exhibit uniform growth along the vertical direction, and consists of multi-length and varied diameter nanorods and initial nucleation islands as shown in Figure 2.7.

The total number of MB molecules ΔN reacted in time $\Delta\tau$ can be expressed as:

$$\Delta N = \int_{h=0}^{h=\bar{h}} -\kappa_s k_\theta b \sigma_h [\mathrm{MB}] \Delta\tau \cdot C(h)\eta(h) A dh - \kappa_s k_\theta b \sigma_h \Delta\tau A_o [\mathrm{MB}] \quad , \tag{2.11}$$

where A is the projected surface area of the substrate, A_o is the TiO_2 island surface area, $\eta(h)$ is the density of the nanorod array, and $C(h)$ is the circumference of the nanorods at height h. The first term on the right of Eq. (2.11) represents the surface reaction due to all the nanorods, and the second term represents the reaction by the nucleation islands between the nanorods that were shadowed by the growth (cannot see from SEM cross-sectional view). Since $\eta \propto h^{\gamma}$ and $C \propto h^{p}$, we have,

$$\Delta N = -D\kappa_s k_\theta b \sigma_h A [\mathrm{MB}] \Delta\tau \frac{1}{1+p+\gamma} h^{1+p+\gamma} - \kappa_s k_\theta b \sigma_h [\mathrm{MB}] \Delta\tau A_o \quad , \tag{2.12}$$

where D is a proportional constant coming from C-h and η-h dependence. Considering Eq. (2.5), we can estimate the overall reaction rate κ to be,

$$\kappa = Mh^{1+p+\gamma} + N \quad , \tag{2.13}$$

where $M = \frac{\kappa_s k_\theta b \sigma_h A}{(1+p+\gamma)V}$, and $N = \frac{\kappa_s k_\theta b \sigma_h A_o}{V}$. Equation (2.13) shows that the photodecay rate κ is proportional to the chemical reaction rates κ_s and k_θ, the surface hole density σ_h, and that κ also monotonically increases with the illumination area A, and is directly related to the nanorod length h and scaling exponents p and γ. The chemical reaction rates rates κ_s and k_θ, are associated with the temperature and the detailed chemical pathways. The photo-generated hole surface density σ_h, is determined by the UV light intensity and the detailed carrier dynamics of the TiO_2 nanorods. In terms of the morphological dependence, Eq. (2.13) gives $\xi = 1 + p + \gamma$. Using our experimentally determined $p = 0.6 \pm 0.3$, and $\gamma = -0.3 \pm 0.3$, we obtain $\xi = 1.3 \pm 0.6$,

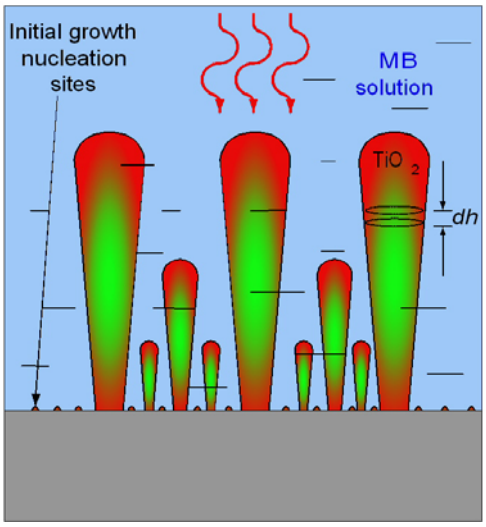

Figure 2.7 The interfacial reaction model for the nanorod array substrate

which agrees well with the experimental value. Thus, the photocatalytic decay rate is closely related to the nanorod morphology.

2.6 Conclusions

In summary, we find that the photodecay rate κ of MB scales directly with the TiO_2 surface area, and is also affected by the crystal structure. TiO_2 nanorod arrays grown by OAD and GLAD showed considerable photocatalytic improvement over thin films, with the OAD nanorod arrays exhibiting the highest photodecay rate for MB solution due to its maximum surface to volume ratio. The photoactivity of the thin film, OAD, and GLAD samples was also measured for the as-deposited samples as well as samples annealed at T_a = 300°C and T_a = 400°C, and for all morphologies the samples annealed at T_a = 400°C showed maximum photocatalytic performance. In addition, the photodecay rate was measured for OAD nanorods grown at systematically different lengths, and the decay rate was found to scale directly with the nanorod length h, $\kappa \propto Mh^{\xi} + N$. This scaling relationship is determined by the morphological

scaling of the nanorod length through a first-order interfacial reaction mechanism. Both our experimental data and theoretical model fit very well. Our theoretical model also gives a detailed relationship between the photodecay rate κ and other experimental parameters such as UV light intensity and illumination area. We believe this quantitative model could be used for other photocatalyst systems with nanostructured morphologies.

CHAPTER 3

DESIGNING NOVEL TIO_2-AG HETERONANOSTRUCTURED PHOTOCATALYSTS BY OAD

3.1 Introduction

It is well known that combining TiO_2 with a metal with different Fermi energy levels, a charge separation effect can occur. The fundamentals of this process have been described extensively in Chapter 1. We attempted to study the specific effect of combining Ag nanoparticles coated on top of uniform TiO_2 nanorods in order to determine the relationship between the loading of Ag (wt.%) on the photocatalytic performance, and built a theoretical model to explain this behavior. Although adding Ag to the TiO_2 surface produces a charge separation effect to increase the lifetime of photogenerated charge carriers, there will be less active catalytic reaction sites available to perform the chemical reactions. Therefore, there must be a trade-off to reach the maximum photocatalytic performance to combine the beneficial charge separation effect and the loss of active surface area due to adding Ag to TiO_2 In this chapter, we will examine the effects of coating TiO_2 with several loadings of Ag nanoparticles, and compare the photocatalytic properties of each sample. In addition to the experimental findings, we will build a theoretical model to accurately explain the observed results based on

basic physical and chemical principles, and examine the delicate balance between the charge separation and loss of surface area effects from adding Ag nanoparticles to TiO_2 nanorods.

3.2 TiO_2/Ag Heterostructured Photocatalysis

The TiO_2 nanorod arrays were fabricated by the OAD method in an electron beam evaporation system, identical to the previous chapter. In brief, the nominal TiO_2 deposition rate was fixed at 0.4 nm/s with a thickness of d = 1 μm. After the deposition, the samples were annealed at 500 ^oC for 2 hours in air to obtain the anatase crystal phase, which is well known to maximize photocatalytic reaction rates (see Chapter 2). Then, aerosol Ag nanoparticles (Ag NPs) were produced through physical vaporization of a solid Ag precursor wire (99.999% purity, ESPI Inc.) using a mini-arc plasma generated between a tungsten cathode and a graphite anode, with the specific details described in other reports.[10] The Ag nanoparticle coatings were carried out at the University of Wisconsin-Milwaukee under the direction of Dr. Junhong Chen. Different loadings of Ag nanoparticles were controlled by varying the deposition time during the ESFDA process with fixed nanoparticle sizes.

Figures 3.1 (a) and (b) show two representative SEM images of TiO_2 nanorod arrays coated with 0.09 wt.% and 0.32 wt.% Ag nanoparticles.

While it appears that there are only a few Ag nanoparticles on the TiO_2 surface for the lower wt.%, the Ag nanoparticles are much easier to see covering the surface of the TiO_2 for the higher Ag loading (0.32 wt.%) sample. For all the samples, the density of the Ag nanoparticles is found to be greater at the tip of the nanorods than it is further down toward the base of the nanorods.

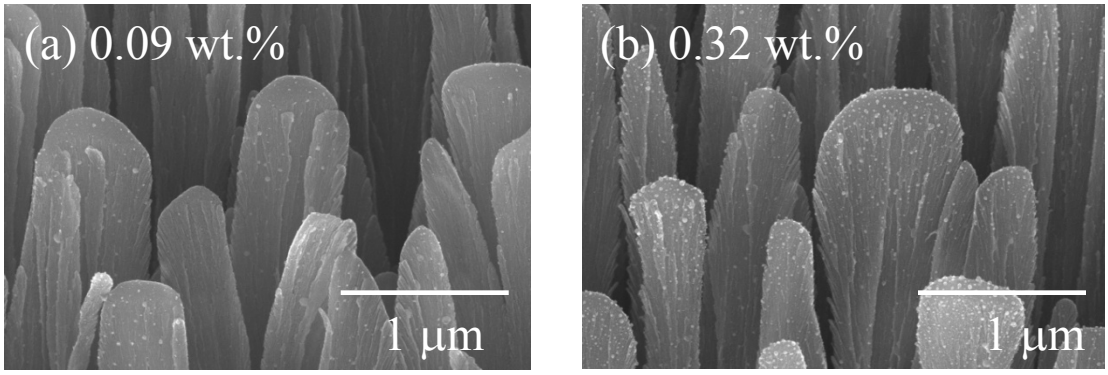

Figure 3.1 Representative SEM images of Ag-coated TiO_2 nanorod arrays, with (a) 0.09 and (b) 0.32 wt.% Ag loading. The images show TiO_2 nanorods covered by Ag nanoparticles, (white spots).

The weight percentage of Ag is calculated by counting the number of Ag nanoparticles on an average TiO_2 nanorod since we cannot use energy-dispersion X-Ray spectroscopy (EDX) to estimate the Ag concentration due to its low surface coverage. In order to get different loading percentages of Ag on the TiO_2 nanorods, we deposited Ag for different time intervals. We deposited Ag for 187.5 s, 225 s, 262.5 s, 300 s, 345 s, and 390 s, to get Ag weight percentages of 0.09 wt.%, 0.11 wt.%, 0.18 wt.%, 0.23 wt.%, 0.25 wt.%, and 0.32 wt.%, respectively. To estimate the average Ag covering a typical TiO_2 nanorod, we first estimated the average size of the nanoparticles. To do this we counted ~ 30 Ag nanoparticles from the high-resolution SEM images for different Ag loadings. The selective size distributions are plotted in Figure 3.2 for Ag loadings of 0.11 wt.%, 0.23 wt.%, and 0.32 wt.%. For all the Ag coated samples, the diameter of the Ag nanoparticles was found to vary from 5 nm to 20 nm, and as shown in Figure 3.2, the Ag nanoparticles of different samples almost follow the same size distribution.

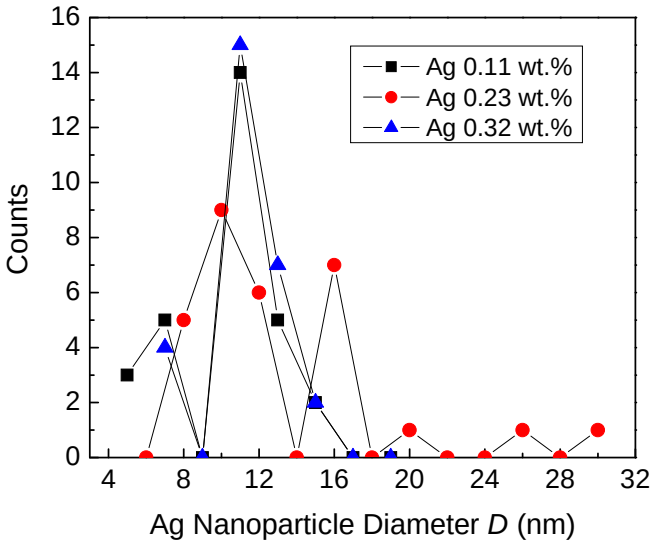

Figure 3.2 Selective Ag nanoparticle size distributions for samples with 0.11, 0.23, and 0.32 wt.% Ag loading, respectively.

For TiO_2 nanorods coated with Ag 0.09 wt.%, 0.11 wt.%, 0.18 wt.%, 0.23 wt.%, 0.25 wt.%, and 0.32 wt.%, we measured the average Ag nanoparticle diameter to be 10.8 nm, 10.8 nm, 11.5 nm, 12.8 nm, 11.9 nm, and 11.3 nm, respectively, i.e., the average diameter is about a constant, 10-12 nm. Although the size and density of the nanoparticles varies along each nanorod, in order to obtain quantitative information about the Ag loading percentages, the number of Ag nanoparticles were counted on most of the TiO_2 rods in the SEM images for each sample (typically 14-18 nanorods), and the numbers were averaged to obtain an estimate of the amount of nanoparticles on a given nanorod. Then, the volume of TiO_2 nanorods was estimated from their morphological parameters. From the cross-sectional SEM images, the average TiO_2 nanorod length is measured to be 730 ± 70 nm. The nanorods are not perfectly cylindrical, so the diameter at the top is different for the in-plane and out-of-plane directions.[4,11] We find an average diameter at the top of D_{in} = 75 ± 5 nm and an average diameter at the bottom of D_B = 40

± 5 nm. The diameter of the top of the nanorods in the out-of-plane direction was found from the top view SEM images to be D_{out} = 250 ± 30 nm. The average density of the nanorods is η = 8 ± 2 rods/μm^2. Using the atomic weight of Ti, O, and Ag, and assuming the bulk densities for Ag nanoparticles and TiO_2 nanorods, we were then able to estimate the Ag wt.% for each of the samples, which ranged from 0.09 wt.% to 0.58 wt.%.

The UV-Vis absorbance spectra of the uncoated TiO_2 nanorods and Ag-coated samples were also measured to confirm the Ag loading trend, and are plotted in Figure 3.3. From the spectra we can see that as the Ag loading increases, the absorbance across a broad wavelength range increases. The insert in Figure 3.3 shows this trend at a fixed wavelength of λ = 350 nm, 400 nm, and 450 nm, respectively. For these wavelengths the absorbance increases monotonically

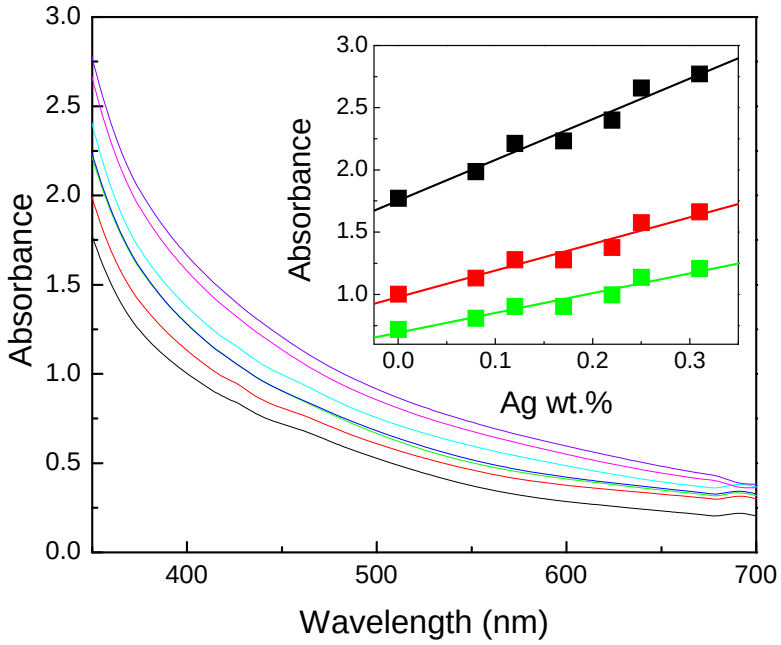

Figure 3.3 The absorbance spectra for the uncoated TiO_2 nanorod array and nanorods coated with 0.09 wt.%, 0.11 wt.%, 0.18 wt.%, 0.25 wt.%, 0.32 wt.% Ag., respectively. The insert shows the absorbance at λ = 350 nm(■), 400 nm(■), and 450 nm (■) with respect to the Ag loading.

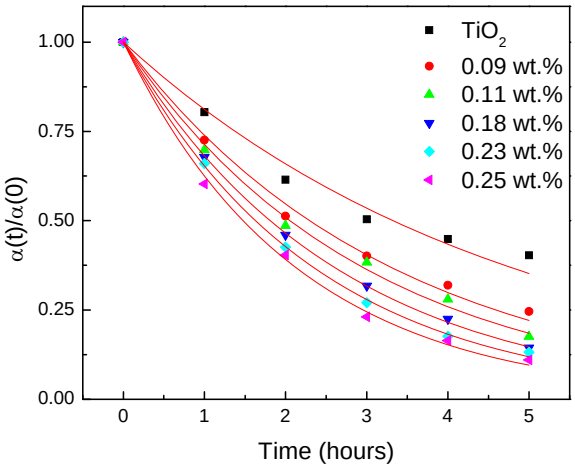

Figure 3.4 The normalized absorbance of MB at the $\lambda = 664$ nm peak is plotted against time (hrs) for 0.09 wt.%, 0.11 wt.%, 0.18 wt.%, 0.25 wt.%, 0.32 wt.% Ag nanoparticle-coated TiO_2 nanorod samples.

with a slope of 3.3 ± 0.3 wt%$^{-1}$, 2.1 ± 0.2 wt%$^{-1}$, and 1.6 ± 0.2 wt%$^{-1}$, respectively. Since the shape of the spectra does not change for different Ag loadings, the increase in absorbance is primarily attributed to the increased scattering and absorbance of Ag nanoparticles on TiO_2 nanorods.

The photodecay rate κ for MB is estimated using the normalized absorbance spectra ($\alpha(t)/\alpha(0)$) of MB, and some representative decay rates are plotted in Figure 3.4. The overall trend for each of the spectral peaks at $\lambda = 664$ nm declines exponentially to the first order, and is different for each sample with different Ag loadings. To determine a relationship between the Ag loading percentage and the photocatalytic decay rate, the decay rates κ for TiO_2 nanorod arrays coated with different amounts of Ag are plotted as a function of the Ag wt.% loading percentage in Figure 3.5. It is apparent that nine of the ten Ag-coated samples show improved photocatalytic behavior compared with the TiO_2 nanorod array by itself. The decay rate for the

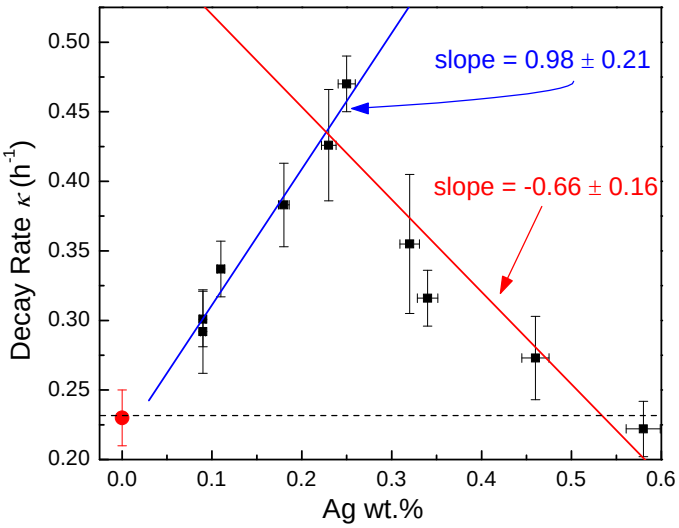

Figure 3.5 The photodecay rate κ (h^{-1}) versus Ag loading (wt.%): the black squares represent the data points from the Ag-coated samples, and the red circle and dashed line represent the decay rate for uncoated TiO_2 nanorod array.

Ag-coated TiO_2 nanorod arrays initially increases linearly with the Ag loading percentage and reaches a maximum at 0.25 wt.%. When more Ag is coated, the decay rate begins to decrease, almost linearly, but is still higher than that of the TiO_2 alone (for the last sample, the decay rate is lower than that of the bare TiO_2 nanorod sample). From the two linear portions in Figure 3.5, we can obtain a slope of $D = 0.98 \pm 0.21$ for the first part, and $F = -0.66 \pm 0.16$ for the second part.

3.3 Modeling the Photocatalytic Performance of Ag coated TiO_2 Nanostructures

The photodegradation of MB by TiO_2 is a very complicated process that involves several steps. First, the incident UV-photons create electron-hole pairs in the TiO_2 nanorods. Electrons are elevated from the valence band to the conduction band in TiO_2 and leave behind positively charged holes. Both the electrons and holes can reduce and oxidize water and create active oxygen radicals.[12] These oxygen radicals then breakdown the MB molecules through an

irreversible photoreaction.[12] While the highly oxidative holes primarily react with the water molecules directly, they can also react with the intermediate products of the initial reaction. Although these reactions are not as common or frequent as the primary reaction, they tend to occur regularly in environments with a low pH, or in the presence of sacrificial electron donor's (SED's),[12] which are not present in our system. Adding these SED's lowers the pH of the MB solution, and adds many more intermediary reactions that consume the oxygen radicals used in the irreversible photodegradation of MB. These reaction conditions also reduce MB to leuco-methylene blue (LMB), which can then be reversibly oxidized back to form MB in the presence of oxygen. For our photoreaction, adding oxygen to the solution after the degradation did not reproduce MB, so we believe that our reaction mechanism is dominated by the irreversible photomineralisation of MB. Overall, methylene blue has proven to be a valuable dye molecule to determine the photocatalytic activity of numerous compounds, and specifically TiO_2 based systems, for visible light photocatalysis[13,14] and UV photocatalysis.[4,15]

Most of the research on TiO_2 nano and microstructures used to photodegrade MB have determined that the main mechanism for the dye removal is the redox reaction occurring at the interface between the solution and the photocatalyst. The primary driving force for the overall photo-reaction is the holes that react with water molecules at the surface of the catalyst, although the holes may also react with other intermediaries as described above. In this regard, the amount of holes at the surface dictates the amount of oxygen radicals that are formed, which then dictates the amount of MB molecules that can be consumed during the reaction. A surface reaction mechanism is formulated in Chapter 2 based on the Langmuir isothermal and hole generation for such a photoreaction for intrinsic TiO_2 nanorod arrays.[11] This proposed mechanism relates the overall decay rate of the MB solution to the amount of oxidizing holes

that can come in contact with the MB molecules, which is directly proportional to the amount of active surface area and the charge density,

$$\kappa \propto N_h \propto A\sigma_h \,, \tag{3.1}$$

where N_h is the amount of photogenerated holes at the nanorod surface, A is the real surface area of the nanorod array, and σ_h is the surface hole density. While there are other factors that play a part in the overall photo-reaction such as the electron-hole diffusion, MB molecular diffusion, and light absorption, we believe these aforementioned parameters are the primary components for determining the overall decay rate of the reaction. As we stated above, the first-order reaction model is based on the two rate limiting steps, the MB molecule absorption on the TiO_2 surface and the hole generation process, and ignored other intermediate steps during the photodegradation of MB, which is consistent with most experimental observations.[16~19] With Ag nanoparticles covering the TiO_2 nanorod, the surface density of holes that are near the surface of the TiO_2 nanorods is different from that without Ag coating. Since the photoreactions occur at the surface of the TiO_2 nanorod, either by direct hole oxidation, or by hole induced hydroxyl oxidation, we are only concerned with the total amount of charge that is at the surface that drives the reaction. We assume that the electron-hole pairs generated on the surface of the TiO_2 nanorods are the same, with or without the Ag coating. For a pure TiO_2 surface, the hole generation rate G is given by, $G = \sigma_h/\tau_1$, where τ_1 is the effective lifetime of the photogenerated holes in the TiO_2 nanorod. Here, τ_1 could be determined by many different recombination processes such as direct electron-hole recombination, defect state trapping, surface trapping etc. For example, we can express the effective lifetime of the photogenerated holes as,

$$\frac{1}{\tau_1} = \frac{1}{\tau_h} + \frac{1}{\tau_t} + \frac{1}{\tau_{cs}} \tag{3.2}$$

where τ_h is the hole lifetime due to direct band recombination, τ_t is due to electron and hole trapping, and τ_{cs} is the lifetime due to charge separation. For the system with pure TiO_2, we can assume that there is negligible charge separation, and this is a rather simple but straightforward assumption for complicated charge dynamics in systems like TiO_2. However, for surfaces close to an Ag nanoparticle, silver acts as an electron sink, the photogenerated holes could have a much longer effective lifetime, $G = \sigma_h'/\tau_2$, where σ_h' is the surface charge density around the Ag nanoparticle, and τ_2 is the hole lifetime, where $\tau_2 > \tau_1$. Hirakawa *et. al.* found that combining Ag with TiO_2 allowed electrons to accumulate in the Ag layer, and more holes were available at the surface of the TiO_2.[20] Examining equation (3.2), we assume that the hole lifetime, and trapping lifetimes stay the same, since the Ag is not doped into the TiO_2 where those processes occur. However, due to the charge separation effect of the Ag nanoparticles, we can assume that τ_{cs} is larger for this sample compared to the bare TiO_2 sample. The increased charge separation lifetime then increases the overall effective lifetime of the photogenerated holes, which is why we assume $\tau_2 > \tau_1$.

In addition, we assume that the Ag nanoparticles are spheres with an average radius r and part of the nanoparticle volume is embedded into the TiO_2, shown as a simple model in Figure 3.6. The interfacial area between the nanorod and each Ag nanoparticle can be approximated as the cross-section of the half-sphere nanoparticles. This is a very crude assumption but is valid due to the nucleation process of Ag nanoparticles on the TiO_2 nanorods. However, the estimated exact value may vary depending on the contact area assumption, or πr^2. Under this assumption, the maximum Ag nanoparticle surface coverage is 0.97% at 0.25 wt.%. Also, we assume that the Ag nanoparticles affect the hole density in the immediate surrounding area, creating a bell ring of a Schottky barrier a distance d away from the edge of the particle (Figure 3.6). If the uncoated

TiO_2 nanorod has a surface area of A_o, we can estimate the total number of holes at the surface of the nanorod when coated with N_{Ag} Ag nanoparticles,

$$N_h = [A_o - N_{Ag}\pi(r+d)^2]G\tau_1 + N_{Ag}\pi[(r+d)^2 - r^2]G\tau_2 \ . \quad (3.3)$$

Equation (3.3) can be simplified to a linear form, $N_h = C + DN_{Ag}$, where $C = A_oG\tau_1$, and $D = \pi(r+d)^2G(\tau_2-\tau_1)-\pi r^2G\tau_2$. When more Ag nanoparticles are added to the TiO_2 surface, the exposed TiO_2 surface to the MB solution decreases. Eventually, the area effected by the Ag nanoparticles ($\pi(r+d)^2$) will be greater than the available TiO_2 surface area, and will then decrease the amount of active catalytic reaction sites. This maximum critical Ag nanoparticle amount can be estimated to be $N_{Ag} = A_o/\pi(r+d)^2$. When the amount of Ag nanoparticles is higher than N_{Ag}, the total number of holes on the TiO_2 nanorod surface can be estimated as,

$$N_h = A_oG\tau_2 - \pi r^2N_{Ag}G\tau_2. \quad (3.4)$$

Again, this equation can be simplified to a linear form $N_{surface} = E - FN_{Ag}$, where $E = A_oG\tau_2$, and $F = \pi r^2G\tau_2$. Equations (3.3) and (3.4) fit very well with our experimental results (Figure 3.5) because they show an initial linear increase in the photodecay rate, then at a certain point the decay rate begins to decrease linearly, corresponding to a positive slope in Eq. (3.3) and a negative slope in Eq. (3.4), respectively. Furthermore, we can see in Figure 3.5 that the slope of the linear increase in the decay rate should be greater than the (absolute value) slope of the linear decrease, which suggests that,

$$d > r\left(\sqrt{1+\frac{(\tau_2+\tau_1)}{(\tau_2-\tau_1)}}-1\right). \quad (3.5)$$

If the model is correct, we can estimate the relationship between the effective hole lifetimes τ_1 and τ_2. From Equation (3.3) and (3.4), the ratio of $C/E = \tau_1/\tau_2$. From our linear fitting of Figure 4(b), $C = 0.21 \pm 0.01$, and $E = 0.58 \pm 0.07$, thus $\tau_2/\tau_1 = 2.76 \pm 0.15$, or that the effective hole

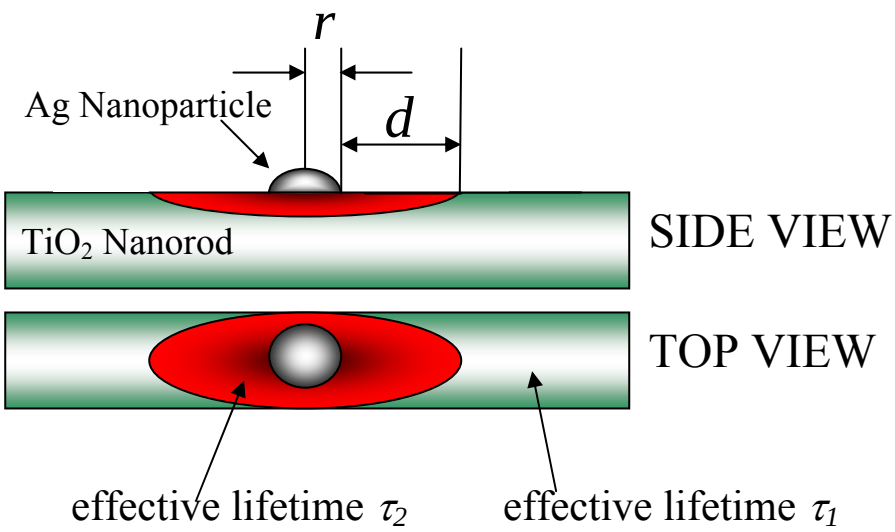

Figure 3.6 A model representation of a TiO_2 nanorod covered with a single Ag nanoparticle, with top view and side view images. The radius of each Ag nanoparticle is given by r, and the distance that the photogenerated lifetime is affected by the Ag particle is d away from the edge of each particle. The effective lifetime due to the TiO_2 nanorod is shown as τ_1, and the effective lifetime due to the Ag nanoparticles is shown as τ_2.

lifetime affected by the Ag nanoparticle coating is almost three times that of the TiO_2 alone. Then from Eq. (3.5), we can determine the distance affected by each nanoparticle to be $d = 0.77r \approx 3.85$ nm (r=5 nm). This infers that the distance affected by the Ag nanoparticles d is less than the radius of each particle r.

3.4 Conclusions

In conclusion, we have systematically studied the effects of Ag nanoparticle loading on TiO_2 nanorods and how they enhance the TiO_2 photocatalysis. An optimal loading percentage was found at 0.25 wt.% Ag, and loading above this amount leads to a decrease in photocatalytic activity due to the reduced active TiO_2 surface area. We have established a theoretical model to predict this behavior based on the major rate limiting process in the photoreaction and effective lifetime of the photogenerated holes. Although those assumptions are simple, they have captured the essential physical and chemical processes of the photocatalytic reaction, and the theoretical

prediction is consistent with our experimental results. Using this model, we could estimate the effective area of the charge dynamics that an Ag nanoparticle could affect on the TiO_2 surface, and the effective lifetime of photogenerated holes due to the trapping of the Ag nanoparticle on the surface of TiO_2 nanorods is approximately three times that of pure TiO_2 nanorods. This simple model could help us to design different photocatalysts and could be applied to other nanostructured metal-semiconductor photocatalytic systems.

CHAPTER 4

DESIGNING NOVEL TIO_2/WO_3 HETERONANOSTRUCTURED PHOTOCATALYSTS BY OAD AND GLAD

4.1 Introduction

Combining TiO_2 with metals has proven to be an effective way to enhance photocatalysis. In addition to metals, combining TiO_2 with other semiconductors with similar energy band positions can also create a charge separation effect in order to enhance photocatalytic reactions. In this chapter, we will examine the combination of TiO_2 with WO_3 in various morphologies to see how it affects the overall photocatalytic performance. We will start from large-scale thin films and work toward complicated multi-layered nanorod arrays. In addition, we will compare the photocatalytic activity of these multi-layered samples to their single-layer counterparts to examine the effect adding WO_3 has on enhancing the photocatalytic performance of TiO_2.

4.2 Experimental

Three different two-layer structures, thin film, tilted nanorods, and vertical nanorods, were fabricated by a normal deposition, oblique angle deposition, and glancing angle deposition. A custom-built electron beam evaporation system was used to deposit the two-layer TiO_2/WO_3

nanostructures. The source materials used to deposit were TiO_2 (99.9%, Kurt J. Lesker) and WO_3 (99.8%, Alfa Aesar) with no other gases present in the chamber during depositions, and chamber background pressure was at 1-2×10^{-6} Torr. To prepare the WO_3 source material for deposition, WO_3 powder was pressed into 1" diameter pellets at a pressure of ~10,000 psi by a hand press. After creating the WO_3 pellets, they were subsequently annealed in a furnace at T_a = 1000°C for 2 hours in open air. After annealing, the hardened pellets were crushed into smaller pieces and used directly as the evaporation source material. Both Si wafers and glass microscope slides were used as substrates for different characterizations. For thin film deposition, the substrate normal was faced parallel to the direction of the incident vapor flux. For OAD and GLAD, the substrate normal was positioned 86° from the vapor incident direction as shown in Figure 4.1 (a) and (b).

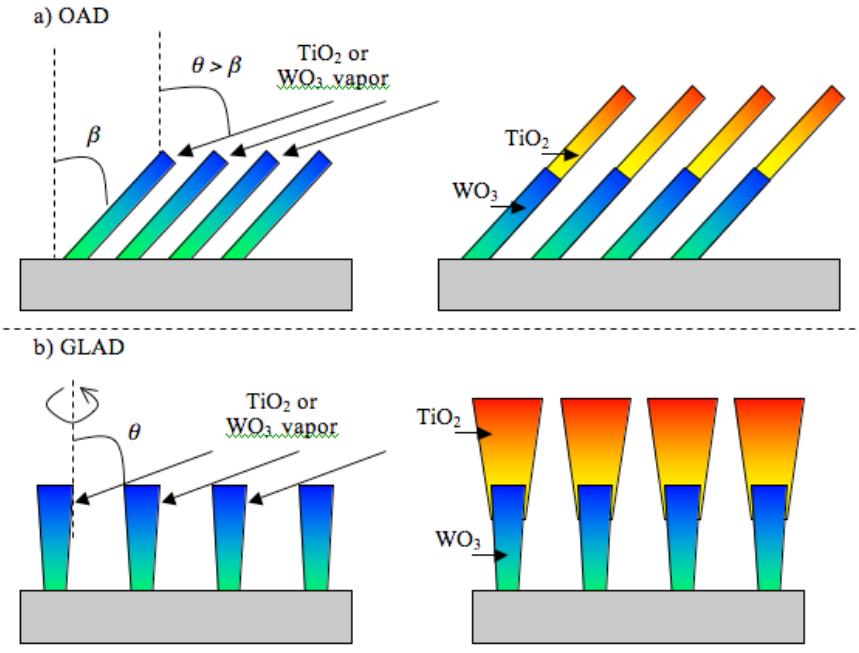

Figure 4.1 The growth geometry sketches for (a) OAD and (b) GLAD. Due to different azimuthal rotation of the substrate, the GLAD nanorod arrays have enhanced TiO_2/WO_3 interfacial area.

For GLAD, the substrate was also rotated azimuthally at a constant rate of 0.5 rev/second (Fig. 4.1 (b)). The growth rate and thickness of the deposition were both monitored by a quartz crystal microbalance (QCM) facing the vapor flux direction directly. For both WO_3 and TiO_2 depositions, the rate was fixed at 0.3 nm/s and each layer was deposited until a reading of 500 nm was reached on the QCM. After the depositions, the samples were annealed in air for 2 hours at T_a = 300 °C, and T_a = 400 °C, respectively.

4.3 Morphological and Structural Characterization

Each two-layer sample was made by first depositing roughly 500 nm of WO_3, on top of which roughly 500 nm of TiO_2 was added. The cross-sectional SEM image of the TiO_2/WO_3 thin films sample is shown in Figure 4.2 (a). The two layers can be seen by different shades of gray in the SEM image, with a thickness of each layer approximately d = 500 nm. As a comparison, in Figure 4.2 (b), the cross-sectional SEM image of the TiO_2/WO_3 OAD nanorod samples is shown. The surface consists of an array of aligned nanorods with the rods tilted towards the direction of the incident vapor. The nanorod array has a density of $\eta \cong 40$ rods/μm^2, an average length of l = 1.33 μm, an average diameter of D = 45 nm, and a tilting angle of β = 55°. The actual surface area is about 7.5 times the projected area. The TiO_2 layer area is about 3.75 times the area of the projected TiO_2 surface (assuming half the nanorod length is from TiO_2). To confirm the composition of the nanorods, the component of the cross-section OAD nanorod array was mapped by EDX, with the resulting Ti and Si compositional mappings shown in Figures 4.2 (c) and (d). The EDX peaks for W (M-α, 1.775 eV) and Si (K-α, 1.740 eV) cannot be resolved by the energy analyzer, so the mapping for Si was used since its signal was more apparent from the substrate. From these images it can be seen that composition of Si (W)

is found to be more dense towards the bottom (surface) of the substrate, while the mapping of Ti is found to be more dense towards the top of the image, confirming our expected composition. The integrated composition profiles from EDX for both Si (W) and Ti as a function of distance (from substrate to the top of the two-layer nanorod array) are shown in Figure 4.2 (e). These results confirm that the top layer is Ti rich with a vertical thickness of $h \approx 500$ nm. The cross-sectional SEM images of a TiO_2/WO_3 GLAD sample (Figure 4.2 (f)), shows an array of vertically aligned nanorods, and they have a density of $\eta \cong 10$ rods/μm^2, an average length of l = 800 nm and an average diameter on top of D = 80 nm. The estimated actual surface area is about 3 times the projected area. The TiO_2 layer is about 1.5 times the projected TiO_2 surface area. Compared to the OAD nanorods, the GLAD nanorods are shorter, wider, and less dense.

The crystalline structures of these three two-layer structures were characterized by x-ray diffraction (XRD) and Raman spectroscopy. Figure 4.3 shows the XRD patterns of the two-layer

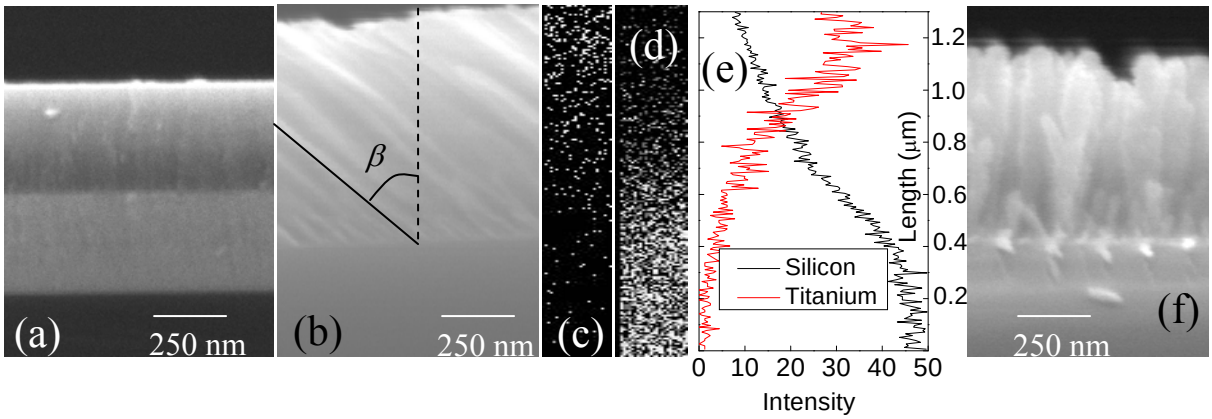

Figure 4.2 (a) Cross-sectional SEM view of the as-deposited two-layer TiO_2/WO_3 thin film. (b) Cross-sectional SEM view of the as-deposited TiO_2/WO_3 OAD nanorod array, and their EDX mapping: (c) Titanium, and (d) Silicon (W). The relative EDX intensity profiles of Titanium and Silicon are plotted against nanorod length (e). (f) Cross-sectional SEM view of the as-deposited TiO_2/WO_3 GLAD nanorod array.

thin film at various temperatures. The as-deposited two-layer thin film sample showed no distinct XRD peaks, which corresponds to the amorphous phase. After annealing the samples at T_a = 300 °C for 2 hours, three sharp peaks at θ = 25.5°, 33°, and 48°, corresponding to the (101), (112), and (200) orientations of the anatase phase of TiO_2, were observed. After annealing at T_a = 400 °C for 2 hours, new XRD peaks appear at θ = 22°, 24°, 28°, 34°, and 53°. Those peaks correspond to the (200), (002), (112), (120), (300), and (420) crystal orientations of the orthorhombic phase of WO_3. The XRD patterns of the as-deposited OAD two-layer nanorod samples, shown in Figure 4.3 (b), are also amorphous. After annealing at T_a = 300 °C for 2 hours, the XRD patterns show peaks corresponding to the crystal orientations of the anatase phase of TiO_2. After annealing at T_a = 400 °C for 2 hours, XRD peaks of the orthorhombic phase of WO_3 were observed, similar to the two-layer thin film sample. However, the GLAD two-layer samples exhibited different structural changes (Figure 4.3 (c)). The as-deposited GLAD sample is still amorphous. After annealing at T_a = 300 °C for 2 hours, no detectable XRD peaks are present, again revealing the amorphous phase for both TiO_2 and WO_3. However, after annealing at T_a = 400 °C for 2 hours, peaks corresponding to both the anatase phase of TiO_2, and the orthorhombic phase of WO_3 were observed. Compared to the OAD two-layer structure, the GLAD TiO_2 nanorods became more orientated, while the WO_3 nanocrystals oriented more randomly.

The XRD pattern for the single layer TiO_2 structures was also investigated and found to correspond directly with the TiO_2 layer of the two-layer structures. These results show the phase transition temperatures for TiO_2 remain the same in both single-layer, and two-layer morphologies.

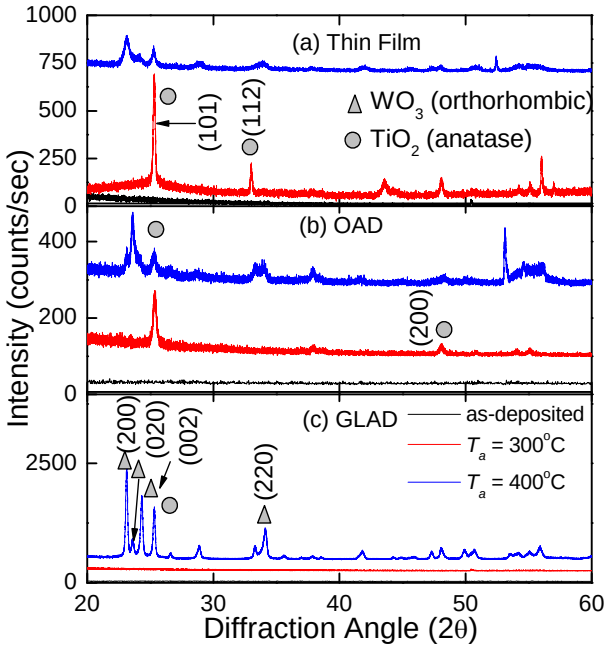

Figure 4.3 The XRD spectra of the as-deposited and annealed two-layer TiO_2/WO_3 samples: (a) thin film, (b) OAD nanorods, and (c) GLAD nanorods.

The structural changes for the two-layer samples at different annealing temperatures were also investigated by Raman spectroscopy. The results confirm the XRD results and show distinct peaks for both anatase TiO_2 and orthorhombic WO_3. For the thin films samples shown in Figure 4.4 (a), the as-deposited spectrum shows only the Raman peaks from the silicon substrate at $\Delta\nu = 300$ cm^{-1}, $\Delta\nu = 510$ cm^{-1}, and $\Delta\nu = 925$~1025 cm^{-1}, confirming an amorphous phase for the deposited materials. The sample annealed at T_a = 300 °C shows distinct peaks at $\Delta\nu = 150$ cm^{-1} and $\Delta\nu = 625$ cm^{-1} corresponding to the anatase phase of TiO_2.[46] The peak at $\Delta\nu = 150$ cm^{-1} is known to be the O-Ti-O vibrational mode of anatase TiO_2.[47,48] After annealing at T_a = 400 °C, the Raman spectra shows a new peak at $\Delta\nu = 800$ cm^{-1}, corresponding to the O-W^{6+}-O vibrational mode of the orthorhombic phase of WO_3.[49,50] For the OAD two-

Table 4.1. Crystal phases for two-layer TiO_2/WO_3 samples at different annealing temperatures

Two-layer sample	**As-deposited**		**T_a = 300 °C**		**T_a = 400 °C**	
	TiO_2	WO_3	TiO_2	WO_3	TiO_2	WO_3
Thin film	Amorphous	Amorphous	Anatase	Amorphous	Anatase	Orthorhombic
OAD	Amorphous	Amorphous	Anatase	Amorphous	Anatase	Orthorhombic
GLAD	Amorphous	Amorphous	Amorphous	Amorphous	Anatase	Orthorhombic

layer sample, the as-deposited sample shows no Raman peaks other than for the Si substrate (Figure 3.10 (b)). The sample annealed at T_a = 300 °C shows distinct peaks for the anatase phase of TiO_2. After annealing at T_a = 400 °C for 2 hours, a peak corresponding to the orthorhombic phase of WO_3 appears. For the two-layer GLAD sample, the spectra for the as-deposited sample and sample annealed at T_a = 300 °C show no distinct Raman peaks other than those from the Si background (Figure 4.4 (c)). However, after annealing at T_a = 400 °C, Raman peaks for the anatase phase of TiO_2 and for the orthorhombic phase of WO_3 can be seen in the spectra. These Raman results confirm our XRD patterns, and reveal the same phase changes for TiO_2 and WO_3 for all morphologies and temperatures with the structural changes of the three samples before and after annealing summarized in Table 4.1.

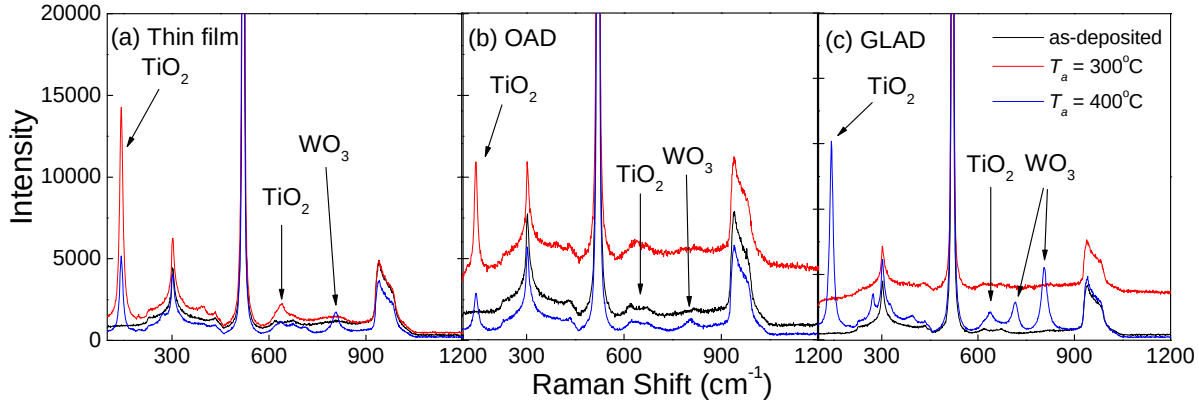

Figure 4.4 The Raman spectra of the as-deposited and annealed two-layer TiO_2/WO_3 samples: (a) thin film, (b) OAD nanorods, and (c) GLAD nanorods.

4.4 Optical Properties

The optical absorbance spectra for all two-layer samples are shown in Figure 4.5. Figure 4.5 (a) shows the two-layer thin film samples at all annealing temperatures. The oscillations that extend throughout the graph are from the constructive and destructive interference of light waves in the thin films. By visual inspection, we can see that the apparent wavelength absorption edge for the as-deposited sample starts around λ = 360 nm, and increases with annealing temperature. For the thin film sample annealed at T_a = 300 °C, the absorption edge slightly increases to λ = 370 nm, and for the sample annealed at T_a = 400 °C, the edge pushes further to λ = 390 nm. For the OAD two-layer samples, similar trends are observed (Figure 4.5 (b)). The as-deposited OAD sample has a wavelength absorption edge around λ = 350 nm, with the edge being slightly larger for the sample annealed at T_a = 300 °C. The spectrum for the OAD sample annealed at T_a = 400 °C shows a much broader absorption edge, starting around λ = 385 nm. In addition to the increased absorption edge, the tail of the spectrum is much larger for the sample annealed at T_a = 400 °C. For the GLAD samples, the spectra closely follow the results for the thin films (Figure 4.5 (c)). The as-deposited GLAD has an absorption edge around λ = 355 nm, the sample annealed at T_a = 300 °C has an edge around λ = 365 nm, and the sample annealed at T_a = 400 °C has an edge around λ = 370 nm. In addition to the lateral movement of the absorption spectra to higher wavelengths, the intensity of the absorbance for wavelengths $\lambda \leq$ 400 nm also increases with annealing temperature for every sample.

For all of the two-layer samples, the apparent wavelength absorption edge increases as the post-deposition annealing temperature increases, which means that the effective band gap decreases with annealing temperature. The thin film and GLAD samples show small increases in the band edge, where the OAD sample shows the largest increase after annealing at T_a = 400 °C.

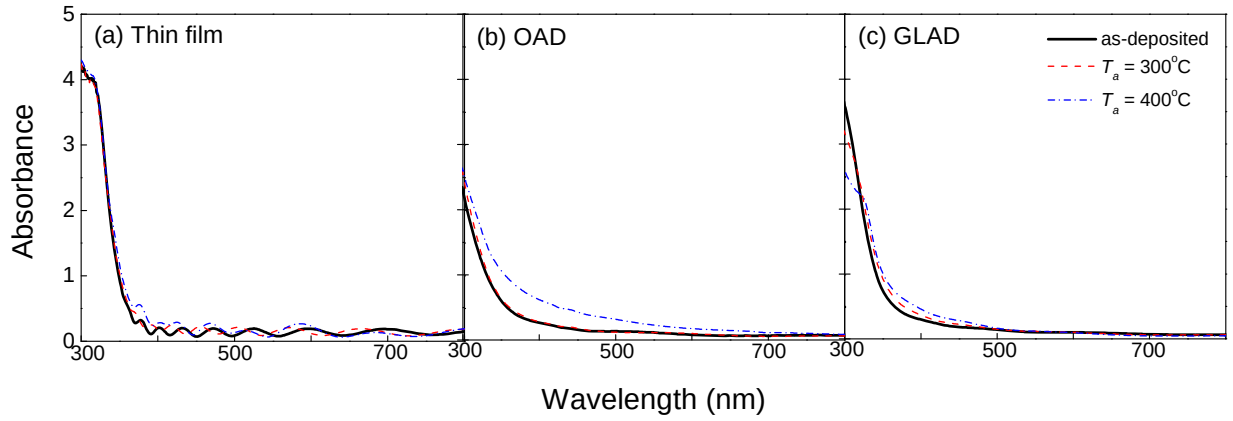

Figure 4.5 Absorption spectra for samples annealed at different temperatures for two-layer TiO_2/WO_3 samples: (a) thin film, (b) OAD nanorods, and (c) GLAD nanorods.

This reveals that the optical absorbance of light in these two-layered structures is morphology dependent.

4.5 Photo-Degradation Characterization

Representative absorbance spectra of MB solution over UV exposure time, t, for the thin film, OAD, and GLAD two-layer samples annealed at T_a = 300 °C are shown in Figure 4.6. The spectra all show characteristic peaks for methylene blue at λ = 664 nm and λ = 612 nm. After UV irradiation of the sample in the MB solution for 30-minute intervals, the absorbance in all the spectra decreases, with the thin film samples showing the least amount of decay and the GLAD samples showing the most decay. In order to find the decay rates for each sample, the intensity of the λ = 664 nm absorbance peak of MB was normalized by the absorbance at t = 0 and plotted against UV exposure time for all of the two-layer and single-layer structures, with the plots for the two-layer samples shown in Figure 4.7. From these plots, the decay rates were determined by fitting the data of the normalized MB absorbance intensity versus UV exposure time with a

first order exponential decay equation. The estimated decay rate κ for different two-layer samples annealed at different temperatures is summarized in Table 4.2. Also, in order to compare the effectiveness of the two-layer structures, the photo-degradation rates for single layer TiO_2 samples are all listed in Table 4.2.

The photo-degradation decay rates for the two-layer samples displayed some similarities to the single layer samples, but also had an interesting difference. The as-deposited two-layer thin film sample shows little degradation over time (Figure 4.7 (a)) with a decay rate estimated to be $\kappa = 1.80\times10^{-4}$ min^{-1}. The as-deposited OAD sample showed an improved degradation, with a decay rate $\kappa = 1.34\times10^{-3}$ min^{-1}, which is over 7 times that of the thin film, while the as-deposited GLAD sample showed superior photo-degradation abilities, with a rate $\kappa = 4.81\times10^{-3}$ min^{-1}. This rate is about 27 times the rate of the thin film sample. The increase in the decay rate for OAD sample is comparable to the TiO_2 surface area enlargement (5 times), but the decay rate for GLAD sample is far larger than the area increment, 27 versus 3.

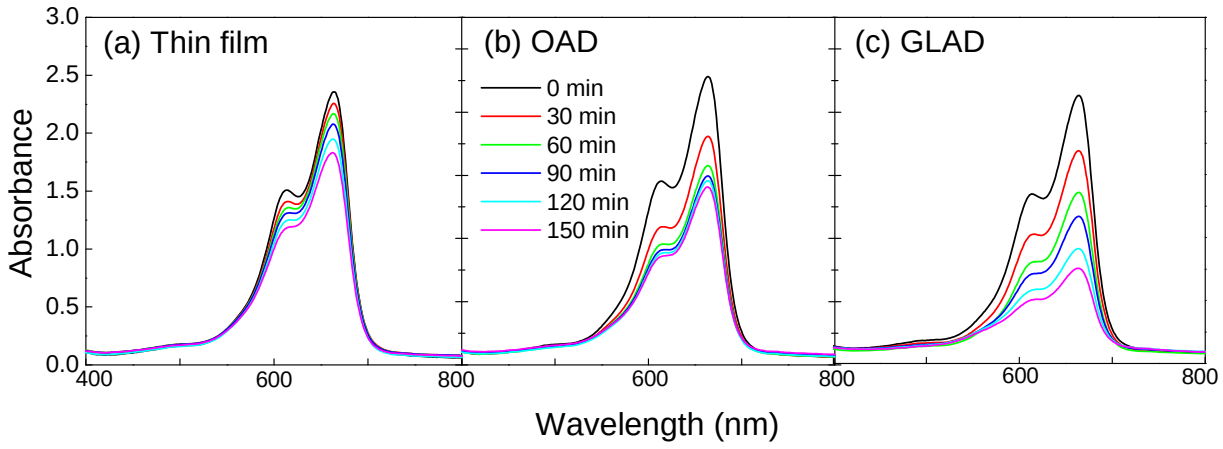

Figure 4.6 Absorption spectra of MB solution after sample irradiation for 30-minute intervals for two-layer samples: (a) thin film, (b) OAD nanorods, and (c) GLAD nanorods annealed at 300 °C.

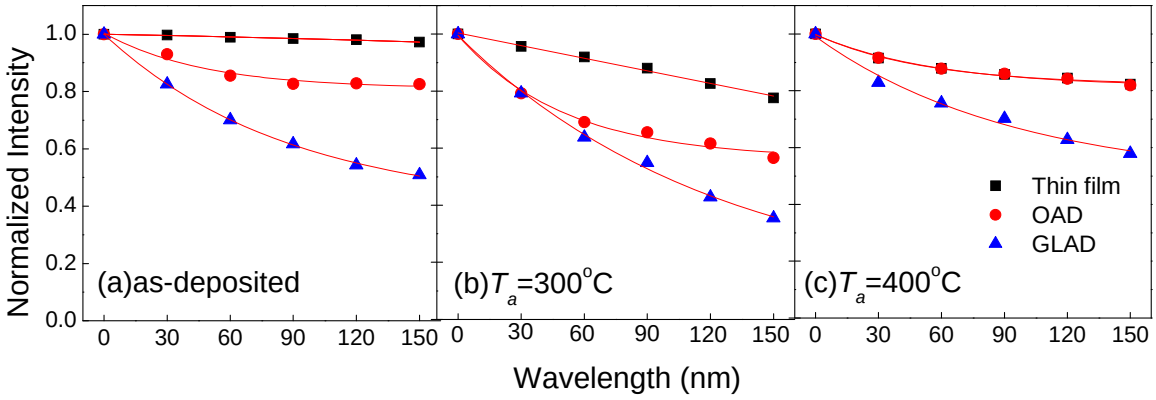

Figure 4.7 The normalized MB absorbance intensities of the λ = 664nm peak versus time (a) for the as-deposited TiO_2/WO_3 samples, (b) for the TiO_2/WO_3 samples annealed at 300 °C for 2 hours in air, and (c) for the TiO_2/WO_3 samples annealed at 400 °C for 2 hours in air. All of the curves correspond to the first-order exponential decay fittings, which were used to find the decay rate, κ.

A possible explanation for this huge enhancement in decay rate has to do with the interfacial area between the TiO_2 and WO_3 layers: the interfacial area between TiO_2 and WO_3 in GLAD structure is much larger than that in OAD structure, and the total number of charge

Table 4.2. Photo-degradation decay rate of MB solution for single layer TiO_2 and two-layer TiO_2/WO_3 nanostructures at different annealing temperatures

		As-deposited	**T_a = 300°C**	**T_a = 400°C**
Single layer samples	Thin Film	6.15×10^{-5} min^{-1}	3.22×10^{-4} min^{-1}	3.25×10^{-3} min^{-1}
	OAD	6.47×10^{-4} min^{-1}	8.08×10^{-4} min^{-1}	3.34×10^{-3} min^{-1}
	GLAD	4.33×10^{-4} min^{-1}	6.75×10^{-4} min^{-1}	1.80×10^{-3} min^{-1}
Two-layer samples	Thin Film	1.80×10^{-4} min^{-1} (2.9)*	1.64×10^{-3} min^{-1} (5.0)	1.22×10^{-3} min^{-1} (0.375)
	OAD	1.34×10^{-3} min^{-1} (2.1)	3.81×10^{-3} min^{-1} (4.7)	1.25×10^{-3} min^{-1} (0.374)
	GLAD	4.81×10^{-3} min^{-1} (11.1)	6.92×10^{-3} min^{-1} (10.2)	3.61×10^{-3} min^{-1} (2.0)

* The values in the bracket are the ratio of decay rate of the two-layer sample to that of their corresponding single layer sample.

separations is greatly enhanced, thus the decay rate increases significantly. This increment of interfacial area is due to the growth nature of OAD and GLAD. Figure 4.1 shows a simplified growth model to illustrate the interfacial areas of the OAD and GLAD nanorod arrays. For OAD process, since the substrate is held still and both the TiO_2 and WO_3 vapors come from the same angle, the TiO_2 nanorod layer is deposited directly on top of the WO_3 nanorod array as shown in Fig. 4.1 (a). The intersection of the two materials is estimated to be proportional to the diameter of the nanorod. For GLAD deposition, since the substrate continuously rotates azimuthally, the resulting nanorod density is much lower than that of the OAD nanorods ($10/\mu m^2$ comparing to $40/\mu m^2$), and the separation between two adjacent nanorods is much larger. Thus, although the incoming TiO_2 vapor still has the same incident angle as WO_3 vapor, it will have the opportunity to coat the top and side surface of the WO_3 nanorods, as shown in Figure 4.1 (b). Thus, a relatively high interfacial area between TiO_2 and WO_3 is predicted, compared to that of the OAD sample. According to Irie *et al*.,[21] this may be the primary reason for the high decay rate of GLAD sample.

For the two-layer samples annealed at T_a = 300 °C for 2 hours, the photo-degradation rates are all enhanced, shown by a larger rate constant for each sample (Figure 4.7 (b)). The two-layer thin films sample had a rate constant of $\kappa = 1.64\times10^{-3}$ min^{-1}, almost a 10-fold improvement compared to its as-deposited state, the OAD sample had a decay rate of $\kappa = 3.81\times10^{-3}$ min^{-1}, about 3 times better, and the GLAD sample had a decay rate of $\kappa = 6.92\times10^{-3}$ min^{-1}. However, for samples annealed at T_a = 400 °C, shown in Figure 4.7 (c), the photo-degradation rates for all the two-layer samples decreases, compared to the samples annealed at T_a = 300 °C. For the thin films, the decay rate is $\kappa = 1.22\times10^{-3}$ min^{-1}, while for the samples of OAD and GLAD, their decay rates dropped to $\kappa = 1.25\times10^{-3}$ min^{-1} and $\kappa = 3.61\times10^{-3}$ min^{-1}

respectively. This trend is not the same as the single layer samples. Clearly, the samples annealed at 300 °C give the best photo-degradation results. Structurally, the difference between the two-layer samples annealed at T_a = 300 °C and T_a = 400 °C is the phase change of WO_3, from amorphous to orthorhombic. It has been shown by Higashimoto *et al*. that the conduction band level of amorphous WO_3 is closer to that of the anatase TiO_2,[22,23] and so the photogenerated electrons can transfer between the two easier than when the conduction band for WO_3 is in the position for the orthorhombic phase. Our results confirm this assertion.

It is also very interesting to compare the decay rate of the two-layer samples to that of their corresponding single layer samples. The data in the brackets in Table 4.2 show the ratio of the decay rate of two-layer structure to that of single layer structure. Those ratios show some interesting trends: both the thin film and OAD samples show the same trend for annealing at different temperature, while the GLAD samples show a very different trend. For the thin film and OAD samples, the decay ratio is about 2.0-3.0 for the as-deposited samples, while the ratio increases to about 5 when the sample are annealed at T_a = 300 °C. The 2-3 times enhancement of the photocatalytic behavior due to the two-layer thin film is well documented in literature.[17~19] This is mainly due to the effect of electron-hole pair charge separation. Annealing at T_a = 300 °C, this ratio becomes more than doubled for both thin film and OAD samples, and from Table I, the TiO_2 layer becomes the anatase phase while the WO_3 layer is still amorphous for these two kind of samples. The only possible reason for such an improved ratio is due to better charge-separation at the TiO_2/WO_3 interface after the phase transition of TiO_2, and it is consistent with the results by Higashimoto *et al*. [22,23] However, after the samples are annealed at T_a = 400 °C, the ratio becomes smaller than unity, ~ 0.37, which means the two-layer samples are worse than single layer samples. The only difference for samples annealed at T_a =

400 °C is the phase change of WO_3 from amorphous state to the orthorhombic phase. This change clearly shows that the charge separation has been significantly reduced once the WO_3 layer becomes orthorhombic, and even produced a negative impact on the decay rate.

For the GLAD sample, the ratio for as-deposited nanorods is 11.1, and for annealed samples at T_a = 300 °C, the ratio is 10.2, which is not significantly different from the as-deposited samples. This is understandable since from Table 4.1 the structures of both TiO_2 and WO_3 layers did not change before and after annealing at T_a = 300 °C. However, this ratio is significantly higher than that of the thin film or OAD samples. As we discussed in above section, the significant increase of the decay rate for OAD samples could be due to additional TiO_2/WO_3 interfacial area formed during deposition. This result further demonstrates this idea. The ratio of samples annealed at T_a = 400 °C is significantly decreased, and this qualitatively agrees with the results from the thin film and OAD samples.

4.6 Optimizing TiO_2/WO_3 Photocatalysis With Core-Shell Nanorods

4.6.1 Core-shell comparison versus other TiO_2/WO_3 nanostructures

The previous section found that several factors can impact the photocatalytic performance of TiO_2 and TiO_2/WO_3 multi-layer nanostructures including the surface area of TiO_2, the interfacial area between TiO_2 and WO_3, and the respective crystal structures of both materials. It is possible to combine these three criteria to create an optimized photocatalytic nanostructure using two consecutive glancing angle depositions at different deposition angles and with different materials. By carefully selecting the deposition parameters and order of deposited materials, a WO_3-core TiO_2-shell nanostructure has been fabricated and has photocatalytic enhancement up to 70 times over amorphous single layer TiO_2 thin films, 13 times

enhancement over crystalline (anatase) TiO_2 thin films, and 3 times enhancement over c-TiO_2/a-WO_3 two-layer thin films, with $1/7^{th}$ the load of TiO_2. We believe that the mechanism for the photocatalytic enhancement is from the increased density of charge separated electron-hole pairs aided by the WO_3 layer, the interfacial area between the two layers, and the large surface area from the porous nanostructure.

The core-shell structure was fabricated through two consecutive GLAD depositions of different materials at different incident angles as shown in Figure 4.8. For the WO_3 deposition, the deposition rate was fixed at 0.4 nm/s, and for the TiO_2 deposition the rate was fixed at 0.3 nm/s. To deposit the WO_3 nanorod "core" structure, the GLAD procedure was used, with the substrate positioned $\alpha = 86^o$ from the incident evaporation direction and an azimuthal rotation speed of 0.5 rev/s. The deposition stopped when the QCM reached 5 μm. After this deposition, the samples were examined in an SEM to determine the height, h, and separation, d, of the nanorods which would determine the "shell" deposition angle θ_s, $\tan(\theta_s) = d/h$, according to the geometric shadowing effect. The substrate was then placed back into the chamber at an angle of θ_s with respect to the incident vapor flux, and TiO_2 was deposited at a rate of 0.3 nm/s with the substrate

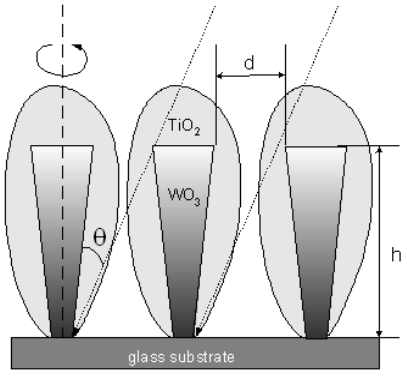

Figure 4.8 A sketch showing how the core-shell nanorod array was deposited using an electron-beam evaporation system.

rotating azimuthally at 0.5 rev/s until the QCM read 75 nm. After the depositions, some of the samples were annealed in air for 2 hours at T_a = 300 °C, and T_a = 400 °C, respectively. Figure 4.9 (a) shows a representative SEM cross-section image of the as-deposited WO_3-core nanorod array. All the nanorods stand on the surface vertically with a smaller diameter close to the bottom (Si substrate) and larger diameter on the top. From Figure 4.9 (a), we obtain h = 1.5 ± 0.1 μm, d = 280 ± 20 nm, and the average diameter at the bottom D_b of the nanorods is 25 ± 5 nm while the average diameter D_t at the top is 220 ± 10 nm. The density of the nanorod array is estimated as 9 rods/μm^2. Thus the "shell" deposition angle θ_s of TiO_2 is determined to be 11^o. Figure 4.9 (b) shows the cross-sectional SEM image of the nanorod array after TiO_2 deposition, and the nanorods appear fatter than WO_3-core nanorods shown in Figure 4.9 (a). The morphological parameters change to h = 1.6 ± 0.1 μm, D_b = 30 ± 5 nm, D_t = 330 ± 10 nm, and d = 150 ± 15 nm, with a density of roughly 9 rods/μm^2. The nanorod array has about the same

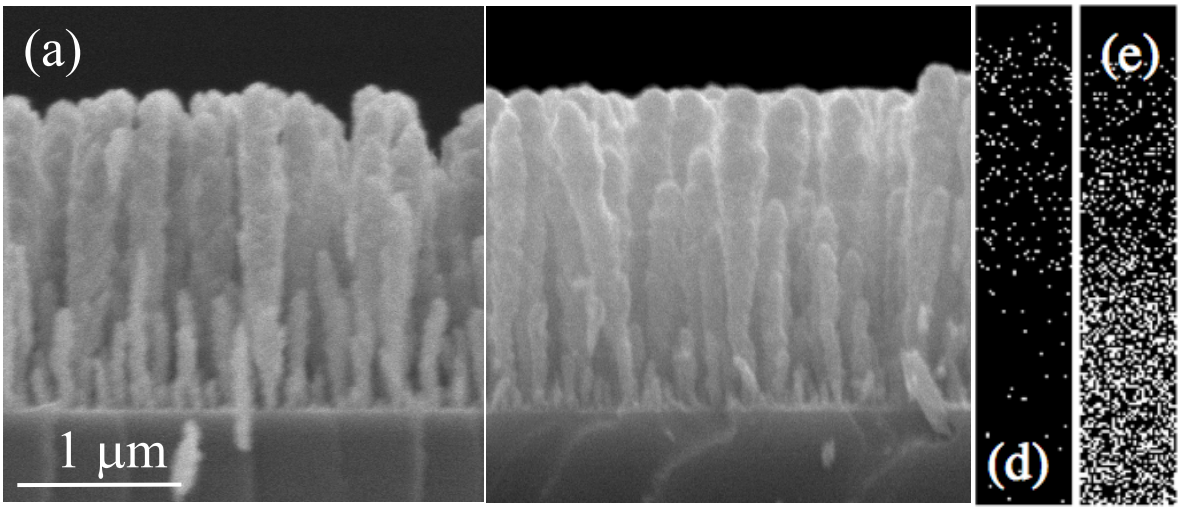

Figure 4.9 (a) Cross-section SEM image of the WO_3 "core" nanorod array. (b) Cross-sectional SEM image of core-shell nanorod array, revealing a vertical array of uniform nanorods after "shell" deposition. EDX mappings of Ti (c) and W (d) versus nanorod length.

density as the WO_3 "core" nanorods, revealing that the addition of TiO_2 did not change the overall lateral arrangement of the nanorod array. However, compared to the pure WO_3 nanorods, the core-shell nanorods became fatter and taller. To verify the distribution of the TiO_2 layer on top of the WO_3 nanorods, energy-dispersive X-Ray spectroscopy (EDX) mapping was used to find the composition of Titanium and Tungsten across a cross-sectional image of the nanorods (Figure 4.9 (d) and (e)). These elemental mappings shows both W and Ti are almost uniformly distributed among the nanorod array, with a higher density of W than Ti. The mapping for W extends down through the substrate since the EDX peak for W (M-α, 1.775 eV) is very close to Si (K-α, 1.740 eV), which was used as our substrate for EDX characterization. The mappings confirm that the TiO_2 "shell" is indeed coated along the WO_3 "core" nanorod, ensuring the intended core-shell morphology.

A detailed image of a single core-shell nanorod was observed by TEM, shown in Figure 4.10.

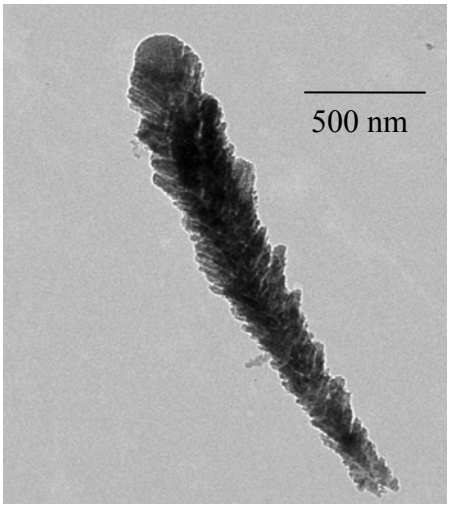

Figure 4.10 TEM image of a single WO_3-core/TiO_2-shell nanorod.

The image shows a single core-shell nanorod with $h \sim 1.4$ μm, $D_b \sim 50$ nm, and $D_t \sim 300$ nm. This image also shows that the nanorods are not uniform along their edges, rather they fan out and have a very porous surface. These results confirm our SEM estimations of the dimensions of each individual nanorod.

The crystal properties of the as-deposited and annealed core-shell nanorod arrays were determined by X-ray diffraction (XRD), and the corresponding XRD patterns are shown in Figure 4.11. The as-deposited sample shows no distinct diffraction peaks, corresponding to the amorphous phase for both materials. After annealing at T_a = 300°C, the XRD pattern shows sharp peaks at 25.5° and 48°, corresponding to the (101) and (200) crystal orientations of the anatase phase of TiO_2. No peaks are present for WO_3, showing that at T_a = 300°C the TiO_2 layer has become crystalline and the WO_3 layer is still amorphous. After further annealing at T_a = 400°C, distinct peaks appear at 22°, 23°, 24°, 28°, 34°, 51°, 54°, 55° corresponding to the (200), (020), (002), (112), (120), (420), (211), and (201) crystal orientations of the orthorhombic phase of WO_3.

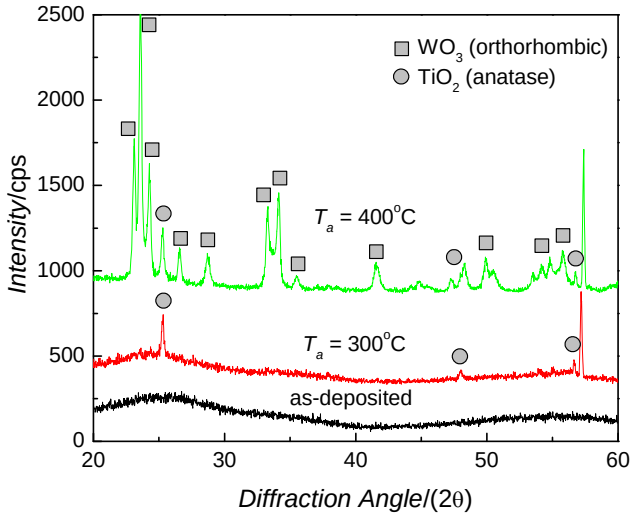

Figure 4.11 XRD patterns of the core-shell nanorod array for the as-deposited sample and the samples annealed at T_a = 300°C and T_a = 400°C, respectively.

The photocatalytic behavior of the annealed core-shell nanorods was measured by the photodegradation of methylene blue (MB) over UV irradiation time. The absorbance intensity of the λ = 664 nm peak, which is characteristic for MB, was used to determined the decay rate of the photocatalytic reaction. The MB absorbance spectra after irradiating the core-shell sample annealed at T_a = 300°C for 10 minutes intervals is shown in Figure 4.13. As the irradiation time increases, the two absorption peaks at λ = 612 nm and λ = 664 nm of the MB solution decreased, while the shape of the spectra kept the same. A similar trend was observed for the sample annealed at T_a = 400°C.

To determine the decay rate of the as-deposited and annealed core-shell samples, the intensity of the absorbance peak of MB at λ = 664 nm was plotted against irradiation time *t*, and is shown in Figure 4.14. Also included in the figure are decay rate plots for an amorphous TiO_2 thin film (500 nm thick), a crystalline (anatase) TiO_2 thin film (500 nm thick), a crystalline (anatase) TiO_2 nanorod array (1.5 μm long), and a crystalline TiO_2 (500 nm)/amorphous WO_3 (500 nm) two-layer thin film as a comparison.[18]

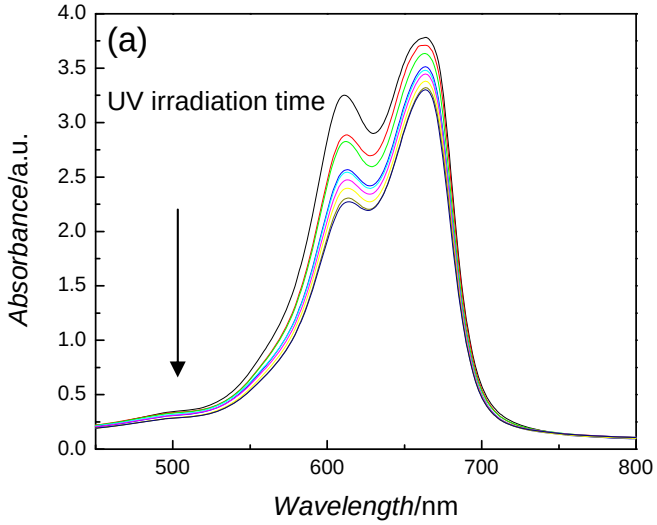

Figure 4.12 Absorbance spectra for MB solution over time after UV-irradiation of core-shell nanorod array annealed at T_a = 300°C. The UV irradiation time interval of each spectrum is 30 minutes. The arrow points to the time increasing direction.

From the exponential decay fittings, the decay rate for the core-shell sample annealed at T_a = 300°C was determined to be $\kappa = 4.33 \times 10^{-3}$ min^{-1}, and for the sample annealed at T_a = 400°C was $\kappa = 1.75 \times 10^{-3}$ min^{-1}.

Comparing these decay rates with amorphous TiO_2 thin films ($\kappa = 6.15 \times 10^{-5}$ min^{-1}), anatase TiO_2 thin films ($\kappa = 3.22 \times 10^{-4}$ min^{-1}), anatase TiO_2 nanorods ($\kappa = 2.51 \times 10^{-3}$ min^{-1}), and a crystalline TiO_2/amorphous WO_3 two-layer thin film ($\kappa = 1.64 \times 10^{-3}$ min^{-1}),[18] the decay rate of the 300°C annealed core-shell sample is roughly 70 times, 13 times, 2 times and 3 times better than each sample, respectively. In addition, compared to the TiO_2 thin film the amount of TiO_2 deposited onto the WO_3 "core" (~75 nm), is far less than that on the film (500 nm). The highest decay rate for the core-shell nanorod array results from two potential mechanisms: the high surface area of TiO_2 and the charge separation effect due to the TiO_2 and WO_3 interface.

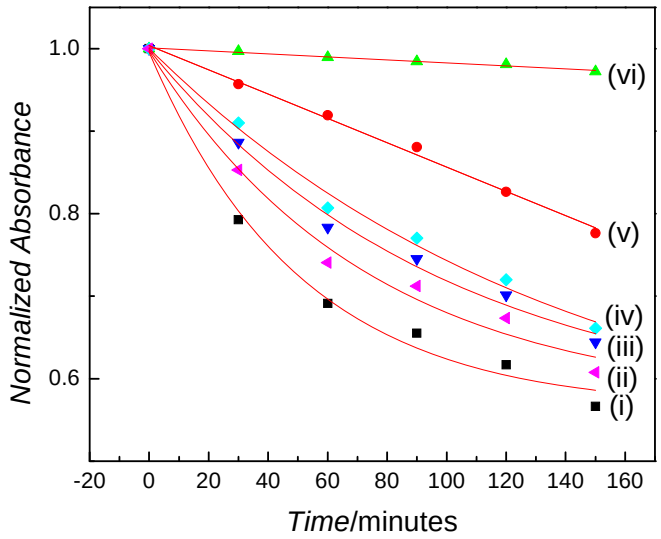

Figure 4.13 The plot of the absorbance of MB at the λ = 664 nm peak versus UV irradiation time for the (i) core-shell sample annealed at T_a = 300°C, (ii) 1.5 μm long TiO_2 nanorod array annealed at T_a = 500°C, (iii) core-shell sample annealed at T_a = 400°C, (iv) c-TiO_2/a-WO_3 two layer thin film (each layer 500 nm thick), (v) anatase TiO_2 thin film (500 nm thick), and (vi) amorphous TiO_2 thin film (500 nm thick).

Our experiments show that for pure TiO_2 nanorod arrays, the photo decay rate under the same experimental conditions increases proportionally with the nanorod length. Compared to the TiO_2 thin film sample, the surface area of TiO_2 in the core-shell structure is estimated to be about 3.5 times, and the surface area of the TiO_2 nanorod array with a length of 1.5 μm is estimated to be 7.5 times. Yet, the core-shell nanorod array has a doubled decay rate compared to the single TiO_2 nanorod array. Thus, we believe that one major reason for the enhanced decay rate of the core-shell structure could come from the charge separation effect, which means that the TiO_2 and WO_3 interface plays an important role. To further quantify this result, we can define a loading percentage for TiO_2 as the amount of the active photocatalyst used compared to the amount of the overall material used in the photocatalytic reaction. If we divide the reaction rate by this loading percentage, we can determine a relationship between the amount of TiO_2 used and the photodegradation abilities, with units ($nm^{-1}min^{-1}$), or decay rate per nm TiO_2. Calculating this ratio for each sample, the amorphous TiO_2 thin film has a ratio of 1.23×10^{-7} $nm^{-1}min^{-1}$, the anatase TiO_2 film has 6.44×10^{-7} $nm^{-1}min^{-1}$, the anatase TiO_2 nanorod array has 3.33×10^{-6} $nm^{-1}min^{-1}$, c-TiO_2/a-WO_3 has 3.28×10^{-6} $nm^{-1}min^{-1}$, the core-shell sample annealed at $T_a = 300^oC$ has 5.77×10^{-5} $nm^{-1}min^{-1}$, and the core-shell sample annealed at $T_a = 400^oC$ has 2.33×10^{-5} $nm^{-1}min^{-1}$. From these ratios we can see that the core-shell nanostructures are much more efficient in the amount of photodegradation abilities that can be extracted per nm of TiO_2 deposited. For the core-shell nanostructures annealed at $T_a = 300^oC$, this ratio is 470 times, 90 times, 17 and 18 times more efficient than the amorphous TiO_2 film, anatase TiO_2 film, anatase TiO_2 nanorods, and multi-layered TiO_2/WO_3 films. This huge improvement in the decay rate per amount of TiO_2 used can be directly correlated to the relatively large amount of interfacial area between TiO_2 and WO_3, which is optimized in this core-shell morphology. Although only $1/7^{th}$

the amount of TiO_2 is used in the core-shell structures compared to the thin films, the large interfacial area between the layers allows the charge separation effect to become dominant, as many charge carriers are able to directly transfer in between layers.

Using the GLAD method to create a novel core-shell heterogeneous nanostructure, we have been able to effectively enhance the overall photocatalytic properties of TiO_2. This versatile method allows for controlled growth of both the WO_3 "core" as well as the TiO_2 "shell", which maximizes the interfacial area between the two materials, but also optimizes the area of TiO_2 that is in contact with the solution. The results show that we have created a superior heterogeneous photocatalytic nanostructure that can out perform other two-layered nanostructures with much less the amount of the active photocatalyst, TiO_2.

4.6.2 Shell deposition angle dependence on the photocatalytic activity of core-shell nanorods

To further understand and investigate the effect of core-shell nanorods on photocatalytic performance, we have designed systematically different core-shell nanostructures. One of the most important issues is to see how the interfacial area affects the photocatalysts performance. Here, we can use the shadowing growth effect to systematically change the interfacial area, and measure the photocatalytic activity to determine their relationship. The WO_3 core nanorods were first fabricated by GLAD, identical to the previous section. The density of the nanorods was found to be 9 ± 2 rods/μm^2 and the average separation at the top of the nanorods is $d = 250 \pm 50$ nm. The WO_3 core nanorods had an average height of $h = 1.0 \pm 0.1$ μm with an average diameter at the top of $D_T = 300 \pm 50$ nm, and an average diameter at the bottom of $D_B = 125 \pm 25$ nm. With these morphological parameters, we were then able to determine several "shell"

deposition angles that would statistically coat the entire core nanorods ($\theta_s = 11^o$), three-quarters of the nanorods ($\theta_s = 15^o$), one-half of the nanorods ($\theta_s = 22^o$), and one-quarter of the nanorods ($\theta_s = 39^o$). We then deposited TiO_2 at these selected "shell" deposition angles, and measured the morphological parameters of each resulting nanorod array. For example, the WO_3 nanorods coated with TiO_2 deposited at $\theta = 39^o$, revealed a nanorod array with an average height of $h = 1.3 \pm 0.2$ μm and an average diameter at the bottom of $D_B = 125 \pm 25$ nm, and an average diameter at the top of $D_T = 375 \pm 50$ nm. For all of the quasi-core-shell nanorod arrays, the height and width at different heights was measured, and a log-scale plot for each sample is shown in Figure 4.15. From Figure 4.15, we are able to determine that the diameter of each nanorod array obeyed a power scaling law against the nanorod height, $D \propto h^p$, where the scaling exponent p was determined graphically for every sample. From these plots, we can see that the WO_3 core

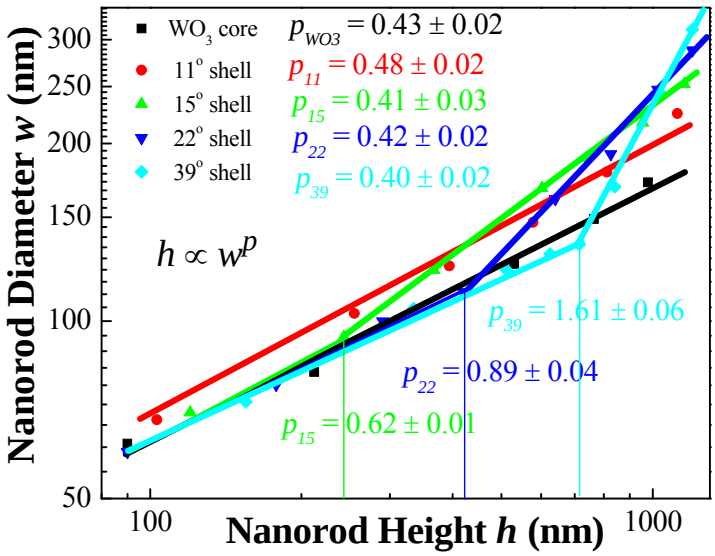

Figure 4.14 A log-scale plot of the average height and width of the core-shell nanorods, as well as the initial WO_3 core nanorod. The width scales with the height in one or two linear trends for each of the shell deposition angles.

nanorods and the nanorods with a "shell" deposited at $\theta_s = 11^o$ show a linear trend throughout the whole graph, with scaling exponent's of $p_{WO3} = 0.43 \pm 0.02$ and $p_{11} = 0.48 \pm 0.02$, respectively. However, for the samples that are partially covered with TiO_2 ($\theta_s = 15^o$, 22^o, 39^o), there are two distinct linear trends. The initial linear relationship is related to the morphology of the WO_3 nanorods that are uncovered by TiO_2, and we find $p_{15} = 0.41 \pm 0.03$, $p_{22} = 0.42 \pm 0.02$, and $p_{39} = 0.40 \pm 0.02$, which are very close (within error bar) of the uncoated WO_3 exponent. At a certain height for each nanorod array, the width increases more dramatically than at the base and diverges off with a new power law exponent. The sudden increase in width for these samples is attributed to the TiO_2 covering the WO_3 nanorods. For the nanorod array coated with a shell at $\theta_s = 15^o$, the diameter of the nanorods begin to diverge at around $h = 245$ nm, and the width continues to scale with the height with an exponent $p_{15} = 0.62 \pm 0.01$. For the nanorod array coated with a shell at $\theta_s = 22^o$, the diameter of the nanorods begin to diverge at around $h = 425$ nm, and the width continues to scale with the height with an exponent $p_{22} = 0.89 \pm 0.04$. For the nanorod array coated with a shell at $\theta_s = 39^o$, the diameter of the nanorods begin to diverge at around $h = 715$ nm, and the width continues to scale with the height with an exponent $p_{39} = 1.61 \pm 0.06$.

The measurement of the nanorod width and height gives a good illustration of the morphological parameters for each sample. In particular, if we assume the WO_3 core nanorod arrays are the same shape and size for every sample, we can use the measured parameters from the coated samples to estimate the interfacial area between the WO_3 and TiO_2 layers. Using the average height and diameter of the uncoated WO_3 nanorods, we can estimate the average surface area of a single nanorod to be 1.1×10^5 nm^2. The samples coated at a deposition angle of $\theta_s = 11^o$ show an increase in the diameter of the nanorods all the way from the bottom to the top, which is what

we expected from the deposition angle calculation, so we assume the entire WO_3 nanorod is coated with TiO_2, giving an approximate interfacial area of 1.1×10^5 nm^2, equal to the surface area of the uncoated nanorod array. For the sample coated at $\theta_s = 15^o$, we see the diameter start to increase dramatically around h = 245 nm, so we assume that at this point the nanorods are beginning to be covered with TiO_2. Assuming the whole nanorod above this point is covered with TiO_2 as well, we estimate the interfacial area for this sample to be 8.0×10^4 nm^2, or approximately 73% or the nanorod. Similarly, for the samples with a shell deposited at $\theta_s = 22^o$, and $\theta_s = 39^o$, we estimated the interfacial area to be 6.2×10^4 nm^2 and 3.0×10^4 nm^2, corresponding to 56% and 27% coverage, respectively. It is evident that as the shell deposition angle increases, the interfacial area between the TiO_2 and WO_3 layers decreases dramatically.

The optical properties for the as-deposited and annealed samples were investigated, from which the band gap energies were calculated. The reflection and transmission spectra were measured for each sample, and the representative spectra for all of the as-deposited samples are shown in Figure 4.16. From this graph, for both the reflection and transmission, we can see several oscillations in each spectra starting from the longer wavelengths going toward the smaller wavelengths, and at around λ = 380 nm the transmission and reflection spectra sharply decline. We believe the oscillations at the higher wavelengths are due to the interference caused by the nanorod layer, while the sharp decrease below λ = 380 nm is due to the absorbance of the material. To confirm this assumption, we calculated the absorption coefficient of each sample by plugging in the reflection and transmission spectra into the following relation (65,66),

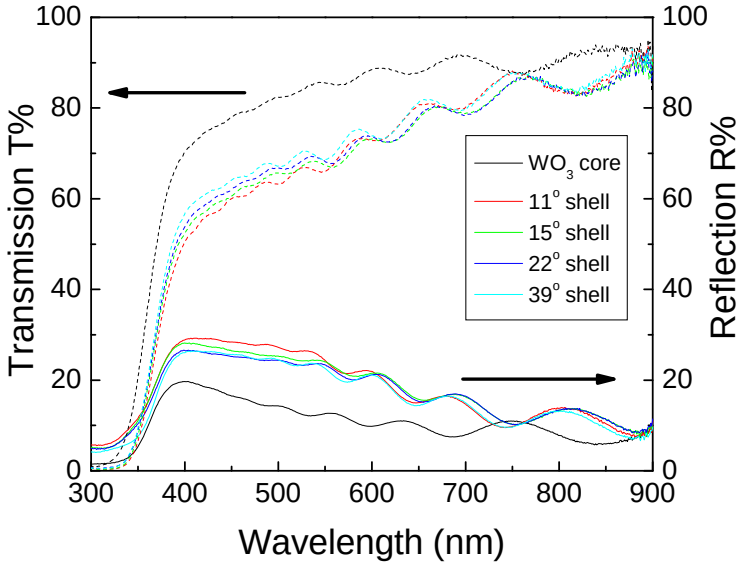

Figure 4.15 The reflection and transmission spectra for the core-shell samples deposited with different shell deposition angles.

$$\alpha d = \ln\left[\frac{(1-R)^2}{2T} + \left(\frac{(1-R)^4}{4T^2} + R^2\right)^{1/2}\right], \tag{3.6}$$

where d is the film thickness and R and T are the reflection and transmission spectra, respectively. Representative absorption coefficient spectra for the as-deposited samples are shown in Figure 4.16, with the inset showing a zoomed in profile of the lower wavelength range where the slope increases the most dramatically. For the WO_3 sample, the absorbance edge begins around λ = 380 nm and steadily increases toward smaller wavelengths while the absorbance edge beings around λ = 400 nm for the TiO_2 coated samples, and increases toward smaller wavelengths. For the samples that have TiO_2 covering more of the surface of the WO_3 nanorods (smaller θ_s), the absorbance edge is shifted to a slightly larger wavelength than for the samples with less of the WO_3 nanorods surface covered (higher θ_s). This trend shows that the

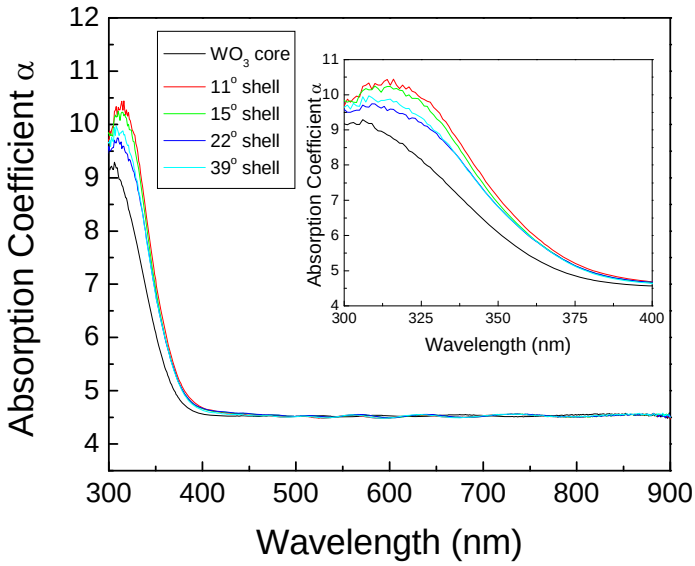

Figure 4.16 The calculated absorbance spectra for the various core-shell nanorod arrays with different shell deposition angles.

core-shell nanorod arrays with more of the WO_3 surface exposed to the air demonstrate optical behavior closer to the uncoated WO_3 nanorod samples. This indicates that the overall absorbance of the samples may be significant on the side-walls of the nanorods, which may be due the magnitude of the light rays that reflect off of the many walls of the porous nanostructures. This is evident in the samples that have a higher side-wall surface coverage of TiO_2 showing an extended spectral absorbance range that can be attributed to the optical properties of the shell material layer, where the nanorod arrays with less TiO_2 surface coverage show optical properties closer to the core WO_3 layer, which is more exposed.

The calculated absorbance of these samples can also help to determine the optical band gap of each sample. Using the absorbance found in equation (3.6), it is possible to plug this value into the following equation that can help to determine the band gap of each substance,

$$\alpha'(h\upsilon)^2 = A\left[(h\upsilon)^2 - E_g^2\right], \tag{3.7}$$

where $\alpha' = d\alpha/d(h\nu)$, $h\nu$ is the incident photon energy, A is the absorbance, and E_g is the band gap. This expression, derived by He *et. al.*,[43] takes into account the interference from the glass substrates, and is a modified version of the traditional equation used to determine the optical band gap of materials that,

$$\alpha h\upsilon \propto \left(h\upsilon - E_g\right)^2 \quad . \tag{3.8}$$

We use Eq. (3.7) to determine the band gap of our samples because it takes into account the reflection and refraction effects of the glass substrates. This equation can be used to determine the band gap of a material by plotting $\alpha'(h\nu)^2$ vs. $(h\nu)^2$, and extending the linear portion of the graph down through the x-axis. Where this line hits the x-axis is exactly the square of the band gap energy. We have plotted this for every sample, and as an example show the band gap determination for all of the as-deposited and annealed WO_3 samples in Figure 4.18.

From this plot we can see that as the annealing temperature of the WO_3 nanorods increases, the band gap decreases. For the sample at room temperature, we estimated the band gap energy to be E_g = 3.18 eV, and decreased to E_g = 3.07 eV, E_g = 3.06 eV, and E_g = 2.85 eV after annealing at T_a = 200°C, T_a = 300°C, and T_a = 500°C, respectively. This trend of the band gap decreasing with increasing annealing temperature is consistent with what we have found in literature. Similarly, we have found this trend to stay true for the TiO_2 samples as well, and have determined the band gap energies for each of the as-deposited and annealed core-shell morphologies, and put all these values into Table 4.3. From this table we can see two distinct trends for the band gap energies of each sample. First, as the temperature increases, the band gap energy for each core-shell sample decreases. We can attribute this to the overall band gap energy of the WO_3 core, since that material takes up a bulk of the volume of the nanostructures. Second, it is apparent that the effective band gap energies increase with an increase in the

interfacial area. This trend can be attributed to the optical properties and band gap energy of the TiO_2 shell. Typically TiO_2 has a bulk band gap of E_g = 3.2 eV (λ = 380 nm) and WO_3 has a bulk band gap energy of E_g = 2.8 eV (λ = 443 nm). However, when these materials are fabricated in nanostructures, the band gaps have been known to shift as a result of the morphological structure. In our case, the nano-sized WO_3 has shown a distinct blue shift towards smaller wavelengths, and the thin TiO_2 shell layer has shown a red shift towards larger wavelengths. These shifts can be due to structural defects within the deposited materials, the crystal structure of each material, and the surface structure of each layer.

It is well known that TiO_2/WO_3 multi-layered photocatalysts perform optimally when TiO_2 is crystalline, specifically in the anatase phase, and the WO_3 layer is amorphous. For all of our different core-shell samples we found this trend to be true, and the optimal photodecay rate was found after annealing at 300°C, which kept the TiO_2 layer in the anatase phase and the WO_3

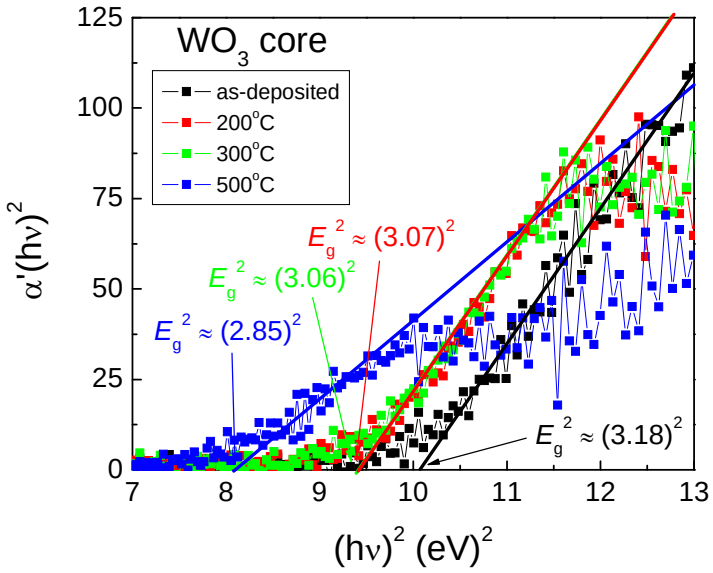

Figure 4.17 Plot of $\alpha'(h\nu)^2$ vs. $(h\nu)^2$, used to extract the band gap energy from the WO_3 core samples annealed at several temperatures.

Table 4.3. Band gap energies for the WO_3 GLAD nanorod arrays coated with TiO_2 at various deposition angles and annealed at different temperatures

	WO_3 core	**$\theta_s = 11^o$**	**$\theta_s = 15^o$**	**$\theta_s = 22^o$**	**$\theta_s = 39^o$**
As-deposited	3.18 eV	3.34 eV	3.29 eV	3.25 eV	3.20 eV
$T_a = 200^oC$	3.07 eV	3.25 eV	3.23 eV	3.19 eV	3.18 eV
$T_a = 300^oC$	3.06 eV	3.25 eV	3.21 eV	3.16 eV	3.16 eV
$T_a = 500^oC$	2.85 eV	3.15 eV	3.10 eV	3.08 eV	3.00 eV

layer amorphous. For our comparative study, we evaluated the photodecay rates for the samples annealed at 300°C in order to see how the optimized samples related to each other. To determine the photocatalytic behavior of the core–shell nanorods, the photodegradation of methylene blue (MB) under UV irradiation was measured. MB has two distinctive peaks at λ = 612 nm and λ = 664 nm which both decrease over UV irradiation time. Typically the absorbance intensity of the λ = 664 nm peak is used to determined the decay rate of the photocatalytic reaction. After several minutes of the photoreactions, the λ = 612 nm and λ = 664 nm peaks decreased steadily, but the overall shape of the peaks became more spread out and a bulge appeared around λ = 580 nm. This spectral shape remains constant after several hours of UV irradiation, and even after several days after degradation, so we take this shape to be the final baseline for the MB solution. In order to better quantify the peak height of the λ = 664 nm peak as a function of time, we fit this peak, as well as the λ = 614 nm peak with Gaussian curves at regular time intervals. We then use the peak height of these Gaussian curves at different times to calculate the decay rate of each sample. In Figure 4.19 we show the height of the Gaussian fit for the λ = 614 nm peak for

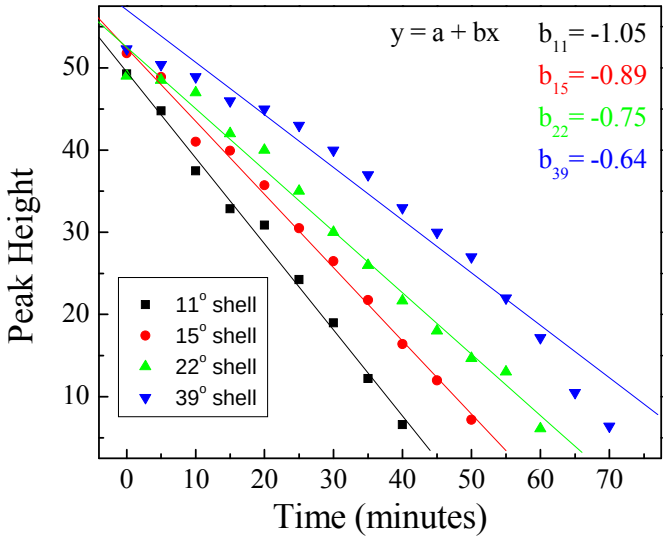

Figure 4.18 Plot of the $\lambda = 664$ nm peak that is fit from the Gaussian curves as a function of time for the angle-dependent core-shell samples.

each of the core-shell samples as a function of time, and fit the points with a linear trend. From this graph, it is apparent that the samples with more interfacial area between the WO_3 and TiO_2 layers degraded the MB solution faster than the samples with less interfacial area. This is shown best by comparing the slopes of each sample, which are $b_{11} = -1.05$, $b_{15} = -0.89$, $b_{22} = -0.75$, and $b_{39} = -0.64$ for the samples deposited at $\theta_s = 11^o$, 15^o, 22^o, and 39^o respectively. No decay fitting is shown for the WO_3 core samples because WO_3 does not photodegrade MB under UV light irradiation.

4.7 White-Light Photodegradations with Core-Shell Nanorod Arrays

In addition to investigating the photocatalysis of the various core-shell nanorod arrays under UV light irradiance, we examined the photodecay effects of visible-light induced photodegradations. Before performing the photodegradations, we irradiated the MB solution

with the visible light source to see if the solution would be photo-bleached without any sample and give us a false reading for the photodegradation. Figure 4.20 shows the absorbance value of the λ = 664 nm peak over time while irradiating the solution with a halogen lamp having a peak intensity at λ = 633 nm of 500 μW for one hour, and then increasing the intensity to 200 mW for another hour. This figure shows that under 2 hours of visible light irradiance, including one hour of light intensity higher than the solar spectrum, the MB solution does not degrade. This is very important to note, so that we can confirm once we put our samples in and irradiate them with the visible light, that all of the photodegradation is being initiated by the samples and not the photo-bleaching of the solution itself.

We began the visible light photodegradation experiments by fabricating core-shell nanorod arrays with a WO_3 core deposited by GLAD. This core nanorod array was identical in morphology to the samples discussed in section 4.6.1. The WO_3 nanorods were then coated with TiO_2 deposited at an angle of $\theta_s = 11^o$, to ensure maximum interfacial area between the two materials, and thus maximum photocatalytic performance as explained in section 4.6.2. The samples were then placed into a clear cuvette which was filled with 35 μM MB solution, and the absorbance of the solution was measured perpendicular to the nanorod samples, identical to all previous photodegradation experiments.

The core-shell samples were irradiated by visible light at various different powers, and the absorbance peak of the λ = 664 nm peak for MB was plotted over time for each power intensity in Figure 4.21. The light intensities were measured at the wavelength λ = 633 nm, which was very close to the peak intensity of the visible light spectrum, shown in Figure 4.22.

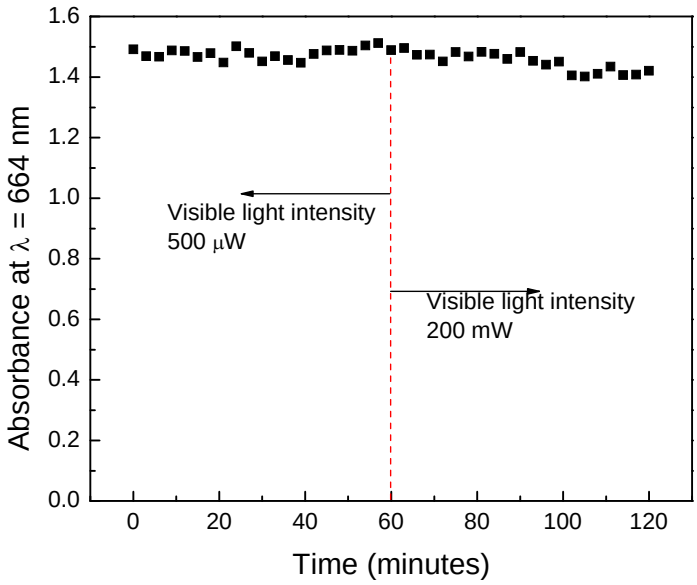

Figure 4.19 The absorbance peak of MB solution at $\lambda = 664$ nm is plotted over time during two successive hours of visible light irradiance at two power levels, 500 μW and 200 mW.

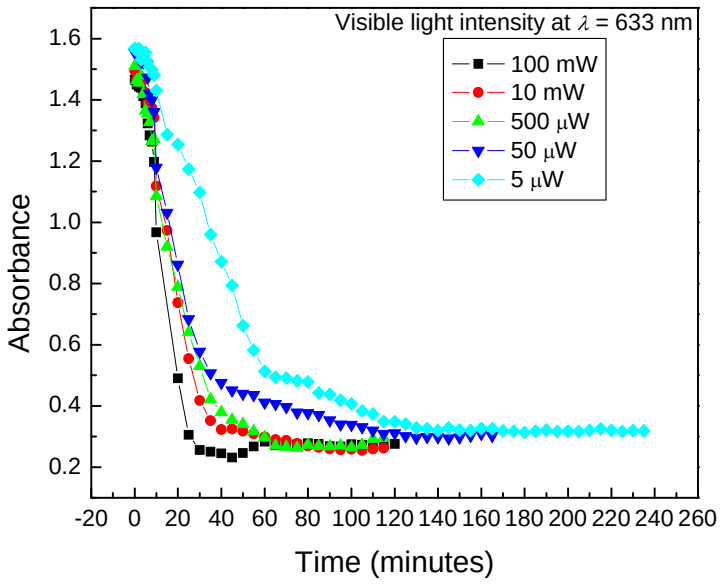

Figure 4.20 The absorbance of the $\lambda = 664$ nm peak for MB was plotted for various visible light intensities as a function of time.

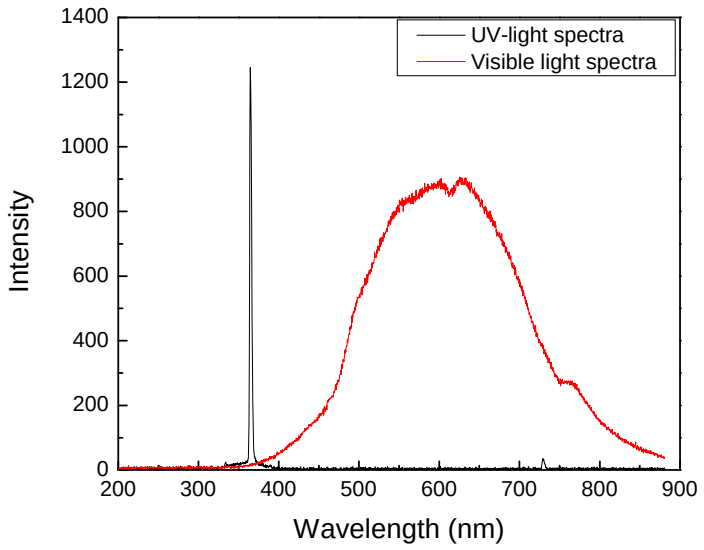

Figure 4.21 The spectra for the visible light source as well as the UV light source used in previous experiments.

The results show that for several different intensities of visible light, the core-shell nanorod arrays are able to effectively degrade the MB solution. In addition, the photodegradation of the MB solution occurred quicker for higher intensities of light, and slower for the less intense light. This is in agreement with the theory of photoexcitation and photodegradation detailed in Chapter 1, which relate the intensity of the incident light to the density of photogenerated charge carriers, and thus photocatalysis. The more intense light creates more electron-hole pairs, and thus can create more chemical reaction pathways to degrade the MB solution. What is particularly interesting to note, is the low level of visible light intensity that could be used to degrade the MB solution. For example, we were able to fully degrade the MB solution within 2 hours while only using 5μW of power. The average light intensity of the sun is 100mW/cm^2, therefore it seems that using these core-shell samples to degrade MB and possible other organic material dissolved in water can be achieved readily using sunlight as the excitation.

4.8 Conclusions

In this chapter, we examined the photocatalytic behavior of various TiO_2/WO_3 heteronanostructures. By starting with very simple morphologies such as two-layer thin films and working up to complex core-shell nanorod arrays, we were able to determine several factors that impact the photocatalytic activity of heterostructred nano-photocatalysts. First, the active surface area of TiO_2 still plays a large part in the photocatalytic activity, as every nanorod structure we fabricated performed better than the two-layer thin film. Second, the relative crystal structure of the TiO_2 and WO_3 materials played a pivotal role in their photocatalytic efficiency. The optimized crystal ratio for photocatalytic performance was found to be with TiO_2 in the anatase phase, and WO_3 in the amorphous phase, which is consistent with previous reports in literature. Next, we found that the interfacial area between the WO_3 and TiO_2 layers was important in the improved photocatalytic performance. In particular, the larger the interfacial area between the two materials corresponded to the largest increase in photoactivity. Lastly, we found that a two-layer TiO_2/WO_3 core-shell nanorod array is able to photodegrade MB solution very efficiently under visible light irradiation, as opposed to the traditional use of UV light. This last result can be beneficial for using direct sunlight to drive photocatalytic reactions instead of UV lamps that can be dangerous and consume power.

CHAPTER 5

OAD AND GLAD NANOSTRUCTURES FOR PHOTOELECTROCHEMICAL WATER SPLITTING

5.1 Introduction

Photoelectrochemical cells (PECs) utilizing photo-active semiconductors have shown great promise for water splitting and alternative energy generation. Some of the most popular materials that have been used are TiO_2, WO_3, and ZnO. However, the current fabrication methods to prepare these materaisl to be suitable for use in a PEC system offer little morphological control, and have shown limited cell efficiencies. In this chapter, we will explore using OAD and GLAD deposition techniques for these materials, and investigate their morphological, optical, crystalline, and electrochemical properties.

5.2 TiO_2 Photoelectrochemical Cells

Dense and aligned TiO_2 nanorod arrays have been fabricated using oblique angle deposition on indium tin oxide conducting substrates. We have demonstrated the first use of these dense TiO_2 nanorod arrays as working electrodes in photoelectrochemical cells used for the generation of hydrogen by water splitting. A number of experimental techniques including UV-visible absorption spectroscopy, X-ray diffraction, high resolution scanning electron microscopy, energy dispersive X-ray spectroscopy and photoelectrochemistry have been used to characterize

their structural, optical, and electronic properties. Both UV-visible and incident-photon-to-current-efficiencies measurements showed their photoresponse in the visible was limited, but with a marked increase around ~400 nm. Mott-Schottky measurements gave a flat band potential (V_{FB}) of +0.20 V, a carrier density of $4.5x10^{17}$ cm^{-3}, and a space charge layer of 99 nm. Overall water splitting was observed with an applied overpotential at 1.0 V (versus Ag/AgCl) with a photo-to-hydrogen efficiency of 0.1 %. The results suggest that these dense and aligned one-dimensional (1-D) TiO_2 nanostructures are promising for hydrogen generation from water splitting based on PEC.

5.3 Results and Discussion

The TiO_2 nanorods were deposited at room temperature (RT), and then annealed in open air conditions at 550 °C. During annealing they underwent a phase transition from amorphous to the anatase crystal structure. XRD spectra show vastly different crystallographic signatures from the as deposited to the fully annealed TiO_2 nanorod samples (Figure 5.1). During the OAD process the substrate was held at RT throughout the deposition onto Si wafers, and in turn showed an amorphous XRD pattern without a trace of representative diffraction peaks. Upon open-air calcinations at 550 °C diffraction peaks were seen at 25.27 ° and 47.96 °. These peaks correspond to the (101) and (200) planes of the anatase crystal phase of TiO_2. The relatively small number of detectable diffraction peaks can be attributed to the thinness of the film at 1 μm, in comparison to 220 μm TiO_2 nanotubes which showed an improved signal-to-noise ratio.[45]

EDS data, which provided information about elemental composition, was collected during HRSEM imaging (Figure 5.2). The O peak at 0.5 keV (O Kα) was by far the most dominant since both the substrate, ITO and the material of interest (TiO_2) contain oxygen. Ti

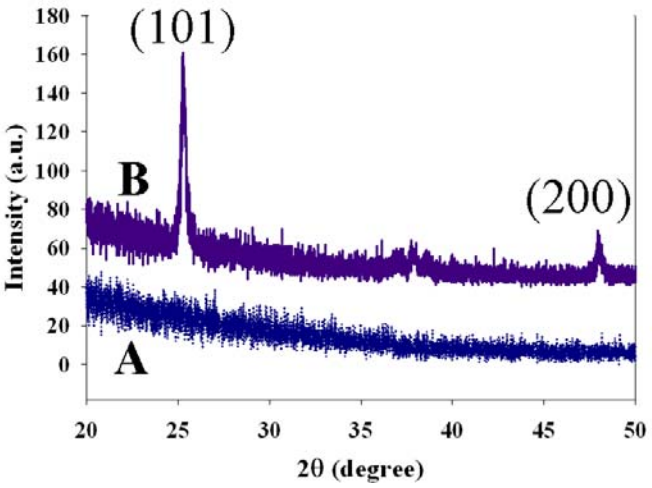

Figure 5.1 XRD plots for the as-deposited and annealed TiO_2 nanorod arrays

peaks at 4.5 keV (Ti Kα) and 4.9 keV (Ti Kβ) had similar counts compared to the signal coming from the substrate.

Peaks arising from the ITO conducting substrate on soda lime glass include Na (Na Kα), Si (Si Kα) and In (In Lα, Lβ, Lγ). No trace of carbon was found during EDS measurements, indicating the lack of hydrocarbon contamination during processing.

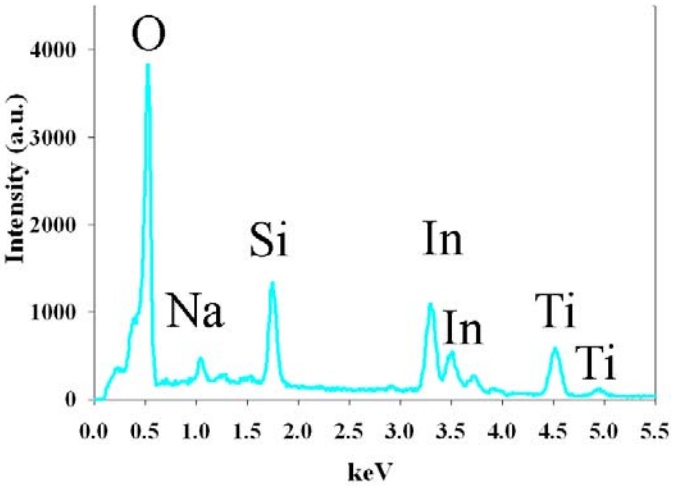

Figure 5.2 EDS spectra for the TiO_2 nanorod array deposited on ITO coated glass substrates

Examination of the TiO_2 nanorods by HRSEM showed several distinct features arising from the OAD technique (Figure 5.3). The first striking feature is that, due to the high angle of the incident adatom plume to the substrate (α= 86 º), the nanorods are tilted from the substrate at an angle of approximately 75 º from substrate normal (Figure 5.3 (a)). Figure 5.3 (a) is actually taken normal to the substrate, but appears to be tilted due to this oriented growth. Overall length of the nanorods was found to be fairly uniform and in the range of 800-1100 nm. A wide distribution existed in the width of the nanorods and was measured to be in the general range of 45-400 nm. The TiO_2 nanorods widen from the base to the tip due to a feathering effect. When examined at higher magnifications, the nature of the surface of the nanorods becomes more apparent. The TiO_2 nanorods display steps and flanges along their surface with a surface topography that is not uniform. The overall surface area of an individual nanorod is thus much higher than that of a nanorod with smooth or uniform surface. Overall density of the TiO_2 nanorods is on the order of $25x10^6$ mm^{-2}, and the relatively high porosity is expected to be useful for PEC applications.

UV-visible absorption spectra of both as deposited TiO_2 nanorods and annealed TiO_2 nanorods at 550 °C show similar absorptive trends (Figure 5.4). As deposited amorphous thin films show little absorption in the visible region (<400 nm), and abruptly increases around 400 nm with an overall absorption of 0.5 at 360 nm (Figure 5.4 (a)). After annealing at 550 °C in open-air conditions there is a subtle increase in the absorption in the visible region starting at 550 nm. Unlike the unannealed edition, they also have a shoulder at ~ 350 nm and an optical density (OD) of 0.8 at 360 nm. The crystallization of TiO_2 is responsible for these changes, since the as-deposited sample is amorphous with an undefined band gap, and after annealing a definite band gap is achieved.

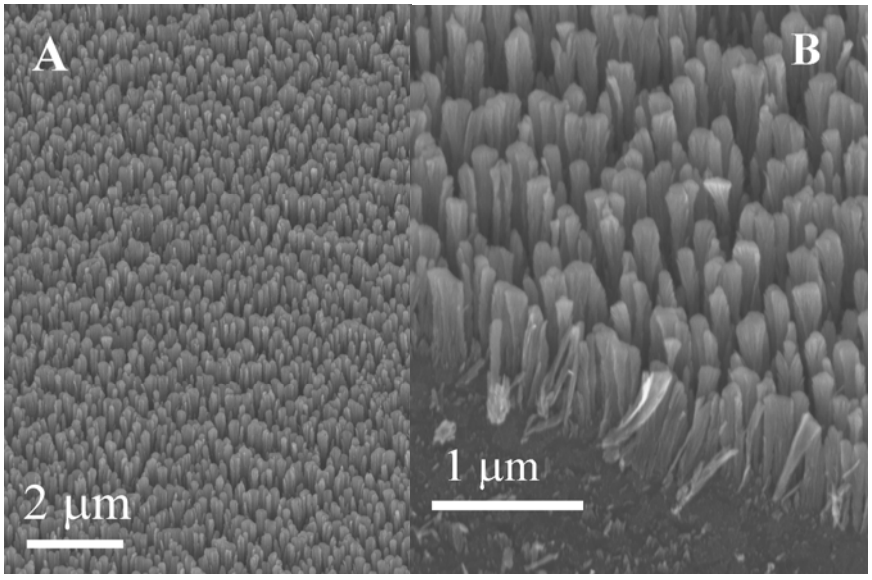

Figure 5.3 Top-view HRSEM images of the TiO_2 nanorod arrays

The band gap of the annealed sample was measured using the relationship,

$$\alpha'(h\nu)^2 = A\left[(h\nu)^2 - E_g{}^2\right] \tag{5.1}$$

where $\alpha' = d\alpha/d(h\nu)$, is the first derivative of absorbance α with respect to $h\nu$. The plot is shown in Figure 5.4 (b). Where this relationship becomes linear and crosses the x-axis is known to correspond to the band gap of the material. For the annealed TiO_2 nanorod sample, the band gap was calculated to be 3.27 eV (380 nm), which is very close to the bulk band gap of 3.2 eV.

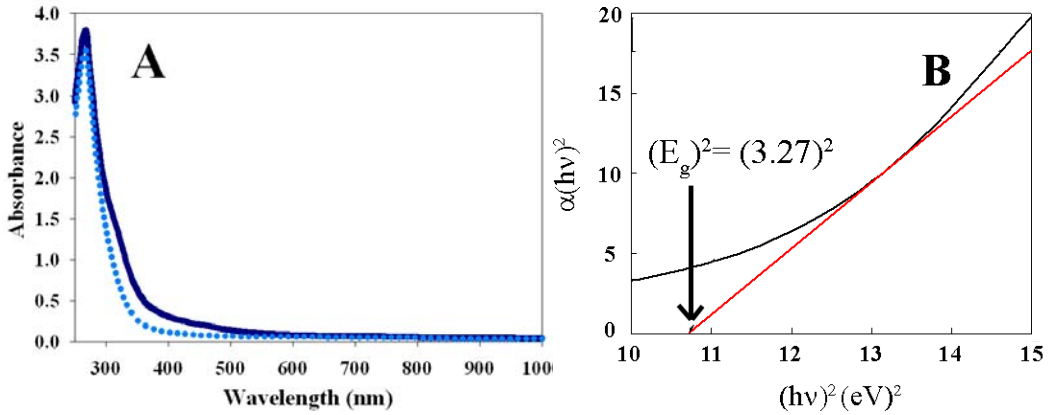

Figure 5.4 (A) The absorbance spectra for the as-deposited and annealed TiO_2 nanorod samples, and (B) the plot of $\alpha'(h\nu)^2$ vs. $(h\nu)^2$ used to determine the optical band gap energy of the annealed sample.

5.4 PEC Characterization and Water Splitting

Linear sweep voltammetry is a common electrochemical technique to examine charge carrier characteristics at the semiconductor-electrolyte interface for n and p-type materials (SEI).[87] A set of linear sweep voltammagrams were measured in a 0.5 M $NaClO_4$ electrolyte solution buffered with phosphate buffer (PB) to pH=7.0 (Figure 5.5). In order to verify that no leakage current was present, a dark current linear sweep was performed in a blackened room from –0.5 V→1.5 V, and showed minute current in the 10^{-9} Acm^{-2} range until approximately 1.4 V where a pronounced increase due to water splitting begins. With an illuminated TiO_2 nanorod cell at AM 1.5 ($100mWcm^{-2}$), there is a pronounced photocurrent (I_{PH}) starting at –0.2 V that continues to increase and has a I_{PH} of 15 μAcm^{-2} at 0.5 V. The I_{PH} does not saturate completely and continues to gradually increase to a I_{PH} of 18 μAcm^{-2} at 1.0 V.

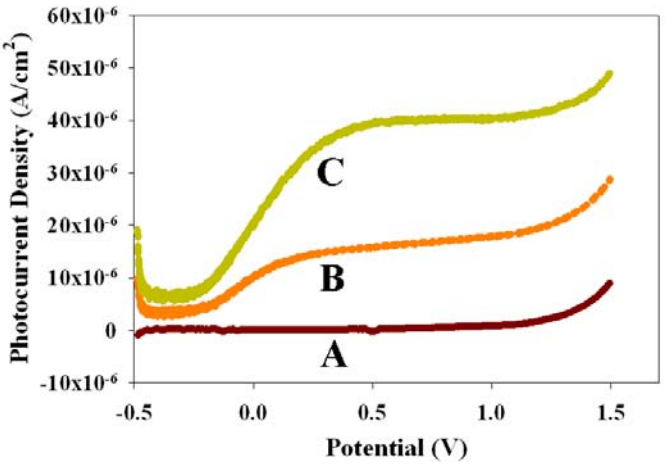

Figure 5.5 Linear sweep voltammagrams taken at a 10 mV/s scan rate in a 0.5 M $NaClO_4$ electrolyte solution with a Ag/AgCl reference electrode, a Pt coiled counter electrode, and a TiO_2 nanorod array working electrode. **(A)** A linear sweep voltammagram in complete darkness showing little background dark current in the scan region of -0.5 V to 1.5 V. **(B)** A linear sweep voltammagram at an illumination at AM 1.5 (100 mW/cm^2) reveals a photoresponse as early as -0.2 V and a photocurrent by ~0.5 V at 15 $\mu A/cm^2$. There is a continued increase in I_{PH} to 18 $\mu A/cm^2$ by 1.0 V. **(C)** An increase of the illumination to 230 mW/cm^2 (2.3 x AM 1.5) shows an above linear increase of I_{PH} to J_{LIGHT} relationship with a saturation photocurrent at 0.5 V with 40 $\mu A/cm^2$.

The increase of I_{PH} at –0.2 V indicates that there is good charge separation upon illumination, but an optimized depletion layer is not fully formed until 0.5 V→1.0 V, where the photocurrent saturates in the ~15 μAcm^{-2}-18 μAcm^{-2} range. Increasing of the incident white light power to 230 $mWcm^{-2}$ (2.3 x AM 1.5) showed a paralleled increase in I_{PH}. In this case, the saturation was observed at ~0.5 V and remained saturated with no further increase in I_{PH}. The saturated photocurrent at 230 $mWcm^{-2}$ was measured to be 40 $\mu A/cm^{-2}$, which is an increase of 166 % in comparison to the AM 1.5 illumination at 0.5 V. The larger than linear increase could be attributed to poorer charge separation at AM 1.5 and that the overall photocurrent was not optimized due to a higher rate of electron-hole recombination or surface trapping. The enhanced performance at 230 $mWcm^{-2}$ could be due to an increased electric field produced in the depletion layer because of the additional photogenerated excitons at the SEI. This increased electric field would in turn localize holes at the surface of the n-type TiO_2 nanorods more efficiently, and allow the photogenerated electrons to be vectorially transported through the long axis of the nanorods and collected at the back-contact.

To examine the photoresponse over time, amperometric I-t curves were collected with light on/off cycles at AM 1.5 (100 $mWcm^{-2}$) and 230 $mWcm^{-2}$ (2.3 X AM 1.5) at 1 V (Figure 5.6). At AM 1.5 the increase in I_{PH} peaked quickly during initial illumination to ~ 25 μAcm^{-2}, and then decreased to a steady-state of 15 μAcm^{-2} after 30 seconds. At 230 $mWcm^{-2}$ the behavior is similar except that the initial I_{PH} spike was at 52 μAcm^{-2}, and decayed to a steady-state value around 35 μAcm^{-2}. The second on-cycle saw a less pronounced spike to 37 μAcm^{-2} and more gradual photocurrent decay to 35 μAcm^{-2}. The types of decay profiles observed at both power densities can be attributed to recombination of charge carriers at surface sites of the TiO_2 nanorods.[88] Strikingly, I_{PH} vs. J_{LIGHT} on the TiO_2 nanorod electrode continues to linearly

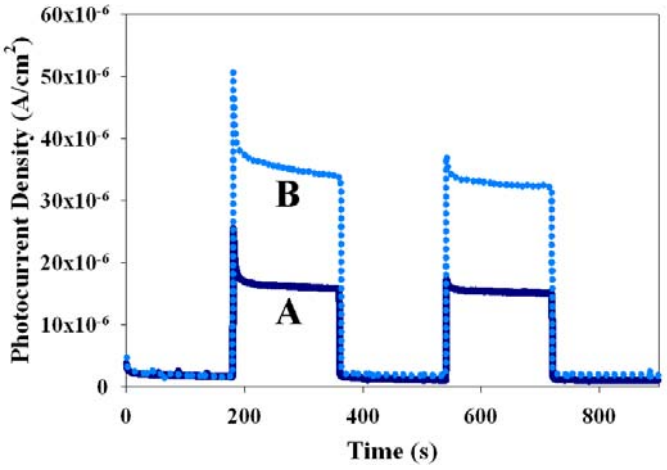

Figure 5.6 Amperometric I-t curves of the TiO_2 nanorod arrays at an applied external potential of 1.0 V in a 0.5 M $NaClO_4$ electrolyte with 180 second on/off cycles. **(A)** I-t curve photoresponse data at AM 1.5 illumination with an immediate photoresponse spike, and then an I_{PH} decay profile to 15 μA/cm^2. **(C)** I-t curve data with an increased linear I_{PH} to J_{LIGHT} relationship at a substrate irradiance of 230 mW/cm^2 with a large photoresponse spike and a decay profile to a steady state I_{PH} of 35 μA/cm^2.

increase at 230 mWcm^{-2} when compared to100 mW/cm^2. There is a direct correlation in the increased steady state I_{PH} (133 %) to the increased irradiance (130%) on the PEC cell. Of practical importance would be the ability to use such a system with solar concentrators, and increase the I_{PH} accordingly. The upper limit to this I_{PH} vs. J_{LIGHT} linear relationship has not been found, but continuing examinations are underway.

AC impedance measurements performed in the dark provide information about the intrinsic electronic properties of the semiconductor in contact with the electrolyte solution. Based on the Mott-Schottky plot ($1/C^2$ vs. V), one can extrapolate the position of the flatband potential V_{FB} from the *X*-intercept, which was found to be +0.20 V (versus Ag/AgCl) at pH=7.0 (Figure 5.7). The capacitance of the semiconductor is described by the Mott-Schottky equation from Section 5.2. An examination into the Mott-Schottky behavior of nanoporous TiO_2 via theoretical and experimental routes revealed different behavior from that of the classic semiconductor electrode model.[82] The inherent differences mentioned were that of the contact made by the

semiconductor to the conducting substrate (indium tin oxide, ITO) and the interaction of the electrolyte throughout the semiconductor network. Taking those aspects into consideration the capacitance relationship was defined by

$$\frac{1}{C^2} = \left(\frac{2}{e_o \varepsilon \varepsilon_o N_d} \right) \left[(V - V_{FB}) - \frac{kT}{e_o} \right] + \frac{1}{C_H{}^2} \quad , \tag{4.7}$$

where C_H is the Helmholtz capacitance.[82,89] While it was found that the V_{FB} shifted negatively from their study, the slope $2/(e_o \varepsilon \varepsilon_o N_d)$ is unaffected and the donor density can still be described by equation (A.2). The V_{FB} of +0.2 V (versus Ag/AgCl) is anodic in comparison to other TiO_2 nanoparticle and nanowires systems reported in the literature.[82,89] In the case of TiO_2 nanoparticle systems, the coverage of the conducting substrate is small (less than 20%) with an electric field that penetrates only 1 particle deep.[82] We believe the case is different for the dense TiO_2 nanorods produced by OAD. Our measured V_{FB} value of +0.2 V can be understood by an increased capacitance of dense TiO_2 nanorod arrays as well as a larger coverage area of the ITO substrate by the TiO_2.[82]

The donor density N_d is derived by the slope of the Mott-Schottky plot and is calculated via theequation found in Section 4.2. With an ε value of 50 based upon a nanoporous model,[82] the donor density, N_d, was then calculated to be 4.5×10^{17} cm^{-3} for our TiO_2 nanorod array system. In comparison, for TiO_2 nanowires produced by a solvo-thermal route, a N_d value of 2×10^{18} cm^{-3} has been reported.[89] Their relatively high carrier density was attributed to a high level of defects caused by oxygen vacancies. The carrier density of our OAD TiO_2 nanorod system can also be attributed to oxygen vacancies, and the results also suggest that the level of defects is lower when producing TiO_2 nanorods via OAD than through the solvo-thermal route. The increase in I_{PH} at 230 mW/cm^2 is strong evidence that the carrier density positively affects

photocurrent generation, and will need to be further studied at higher light intensities. The thickness of the space charge layer in the semiconductor-electrolyte can also be derived from the Mott-Schottky plot relationships and is described in Section 5.2. A potential of 1.0 V was chosen to calculate the space charge region because of the lack of dark current at that potential. According to equation (A.3), the thickness of the space charge layer has been calculated to be 99 nm, significantly smaller than the 1 μm thickness of the TiO_2 nanorod film. When the space charge thickness is smaller than the film thickness, then an increase of photocurrent as a function of space charge thickness should be observed.[90]

IPCE measurements were performed in the photoactive wavelength regime for the TiO_2 nanorod arrays. IPCE action spectra essentially measures the amount of photogenerated electrons which are collected at the back contact per photon irradiated on the PEC surface.

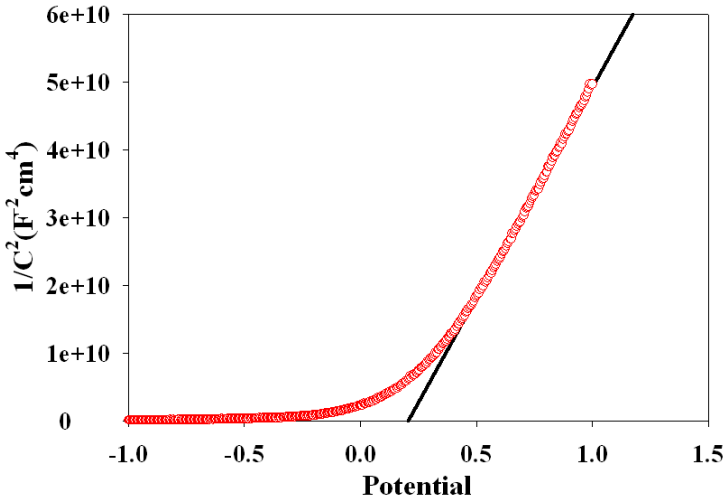

Figure 5.7 A Mott-Schottky plot of $1/C^2$ versus applied potential (V) in complete darkness at a frequency of 10000 Hz and an AC current of 7 mV. From the extrapolated linear portion of the Mott-Schottky plot the V_{FB} was determined to be 0.20 V (versus Ag/AgCl) at a pH=7.0. From the Mott-Schottky plot further information was attained with a calculated donor density of 4.5 $x10^{17}/cm^3$ and a space charge layer thickness of 99 nm.

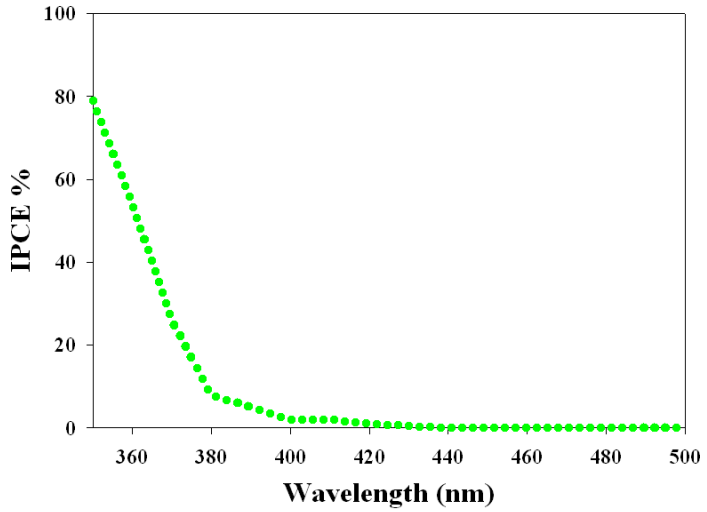

Figure 5.8 IPCE action spectra of the TiO_2 nanorod arrays in the region from 350-500 nm reveals a drastic increase in photogenerated electron collection at the backcontact due to illumination above the bandgap. Prior to 400 nm there is little photoresponse, and this changes drastically with an IPCE % of 79% at 350 nm and 54% at 360 nm. This drops immediately to an IPCE % of only 2% at 400 nm, due to the below bandgap photon energy.

The photoresponse of the TiO_2 nanorod arrays was minimal until 400 nm, and then sharply increased once bandgap illumination had been reached (Figure 5.8). At 400 nm the IPCE was 2% due to the weak absorption below the bandgap energy of 3.27 eV (380 nm). This increased to 8 % at 380 nm, and peaked at 350 nm with an IPCE of near 79% due to strong absorption. A lack of appreciable light below 350 nm from the light source prevented accurate data collection in the 300-340 nm range. The IPCE measurements were reflective of the UV-vis absorption spectrum with an increase in photoresponse as wavelengths were blue shifted from 400 nm. Overall the greatest correction that needs to be considered is the lack of absorbance by the TiO_2 nanorod arrays in the visible region. While the direct irradiance was measured to be 100 $mWcm^{-2}$, several mechanisms for optical loss should be addressed. Reflection is a significant source of optical loss, from the light striking the pyrex PEC container (external reflection), reflection off of the ITO conducting substrate (internal reflection), and reflection off

of the TiO_2 nanorods. We have conservatively placed the amount of reflection losses at 20%. Absorption and scattering is also an optical loss pathway, including absorption and scattering by the pyrex container and the electrolyte solution, which are estimated to be 5%. Overall the reflective, scattering, and absorptive optical losses are about 25%, which reduce the effective irradiance to about 75 mW/cm^2. The limited spectral overlap between the absorption of the TiO_2 PEC cell and the light emission profile of the Xe lamp is the most significant correction. Of the approximate 75 $mWcm^{-2}$ of available light, only about 5% is within the absorptive region between 350-400 nm where TiO_2 absorbs with an average OD of about 0.5. With these corrections, we estimate an effective J_{LIGHT} of 3.15 mW/cm^2. The overall photon-to-hydrogen efficiency is then calculated to be about 0.1% at an applied potential of 1.0 V with a current density of 18 μAcm^{-2}. While the current conversion efficiency is relatively low, it is clearly not yet optimized with respect to many important parameters. For instance, the thinness of the TiO_2 nanorod film coupled with the large bandgap of anatase TiO_2 leaves significant room for improvement in the realm of increasing the nanorod length and enhancing photoresponse in the visible with schemes such as doping or sensitization.[38] An important positive factor of the TiO_2 nanorod arrays is that photogenerated carriers have a high collection rate at the back contact as was observed with an IPCE of 79% at 350 nm and 54% at 360 nm. The good photocurrent production can be attributed to the vectorial charge transport through the long axis of the TiO_2 nanorods and the limited losses caused by electron-hole recombinations and surface trapping. The density of the TiO_2 nanorods ($25x10^6$ mm^{-2}) on the ITO substrate makes efficient use of the available surface area, and allows for more water splitting sites per unit space. These features are unique for photoelectrodes composed of high density, aligned 1-D nanorod arrays and can be further studied to increase the overall water splitting efficiency.

5.5 Conclusions

In summary, TiO_2 nanorods have been fabricated using oblique angle deposition on conducting substrates and used as working electrodes in PEC studies for hydrogen generation from water splitting. The nanorod arrays have been characterized using a combination of spectroscopic, microscopy, and photoelectrochemistry techniques. The nanorods are generally well-ordered, dense, and uniform in length and orientation. With an applied overpotential at 1.0 V and near UV excitation, PEC hydrogen generation from water splitting has been successfully demonstrated. In the future, studies will be conducted to quantitatively compare the PEC performance of TiO_2 nanorod arrays produced by OAD with various lengths and with different strategies to enhance visible absorption including doping and sensitization.

CHAPTER 6

CONCLUSIONS AND FUTURE WORK

In this dissertation, the photocatalytic and photoelectrochemical properties of TiO_2, WO_3, and ZnO nanostructures fabricated by oblique angle deposition and glancing angle deposition were investigated. It was found that by carefully and systematically controlling the morphology and combination of these materials, that the photocatalytic efficiency, and water splitting efficiencies can be improved over there existing performance.

Specifically, by combining TiO_2 and WO_3 nanostructures, a charge separation effect can be achieved that keeps photogenerated electron-hole pairs open for a longer than normal time. It was found that the porosity, surface area, interfacial area, and relative crystalline properties of each material played an important role in the improvement of photocatalysis. Furthermore, by depositing TiO_2 and WO_3 through two consecutive glancing angle depositions, a core-shell nanorod array can be fabricated that has shown significant improvement over single layer photocatalysts, as well as other multi-layered nanophotocatalysts. The improvement in this structures photocatalytic performance is directly related ot the interfacial area between the two layers, which agrees with our theoretical assumptions.

Utilizing OAD and GLAD techniques to create TiO_2 and ZnO nanostructures has also shown the ability to produce effective water-splitting photoanodes. TiO_2 OAD nanorods were fabricated and were the first of their kind to be used in a PEC cell, and showed the ability to

effectively split water under solar radiation. Similarly, various ZnO nanostructures were fabricated by OAD, GLAD, and PLD, which showed unique photoelectrochemical properties, and the ability to effectively split water with different efficiencies.

Because there are so many factors that play important roles in the materials science of photocatalysts and photoelectrochemical water splitting, there is ample room to improve on this work in the future. In particular, combining TiO_2, WO_3, and ZnO with different materials, such as Fe_2O_3 can possibly lead to a greater charge separation effect and improved photocatalysis. In addition, doping these structures with N for example, can introduce several lattice defect sites that can act as electron or hole traps, which can prolong the life-time of the photogenerated charge carriers. Besides the materials properties, morphological advances can be made with nanophotocatalysts that can improve the functionality of those materials, such as tri-layer, or hierarchal nanostructures that exploit a high surface area, and interfacial area between material layers.

REFERENCES

1. Honda, A.K., Fujishima, Nature A. Fujishima, K. Honda, *Nature* **238**, 37 (1972)
2. Fujishima, A., Hashimoto, K., Watanabe H., *TiO_2 Photocatalysis: Fundamentals an Applications*; BKC, Inc.: Tokyo, 1997
3. Kolasinski, K. *Surface Science: Foundamtions of Catalysis and Nanoscience*; John Wiley and Sons Ltd.: London, 2002
4. Linsebigler, A., Lu, G., Yater Jr., J. *Chem. Rev.* **1995**, *95*, 735~758
5. Li, S.S. *Semiconductor Physical Electronics*; Plenum Press: New York, 1993
6. Schockley, W., Read Jr., W.T. *Phys. Rev.* **1952**, *87*, 835~842
7. O. Khaselev, J.A. Turner, *Science* **1998**, 280, 425-427
8. T. Bak, J. Nowotny, M. Rekas, C.C. Sorrell, *Int. J. Hydrogen Energy* **2002**, 27, 991-1022.
9. A. Hagfeldt, M. Gratzel, *Chem. Rev.* **1995**, 95, 49-68.
10. K. Rajeshwar, *J. Appl. Electrochem.* **2007**, 37, 765-787.
11. K.S. Ahn, Y.F. Yan, S.H. Lee, T. Deutsch, J. Turner, C.E. Tracy, C.L. Perkins, M. Al-Jassim, *J. Electrochem. Soc.* **2007**, 154, B956-B959.
12. J.H. Park, S. Kim, A.J. Bard, *Nano Lett.* **2006**, 6, 24-28.
13. J.H. Park, A.J. Bard, *Electrochem. Solid State Letters* **2006**, 9, E5-E8.
14. J.H. Park, A.J. Bard, *Electrochem. Solid State Letters* **2005**, 8, G371-G375.
15. C. Santato, M. Odziemkowski, M. Ulmann, J. Augustynski, *J. Am. Chem. Soc.* **2001**, 123, 10639-10649.

16. C. Santato, M. Ulmann, J. Augustynski, *J. Phys. Chem. B* **2001**,105, 936-940.

17. A. Wolcott, T.R. Kuykendall, W. Chen, S.W. Chen, J.Z. Zhang, *J. Phys. Chem. B* **2006**, 110, 25288-25296.

18. C. Santato, M. Ulmann, J. Augustynski, *Adv. Mater.* **2001**, 13, 511-514.

19. A.M. Morales, C.M. Lieber, *Science* **1998**, 279, 208-211.

20. X.F. Duan, Y. Huang, Y. Cui, J.F. Wang, C.M. Lieber, *Nature* **2001**, 409, 66-69.

21. J.T. Hu, M. Ouyang, P.D. Yang, C.M. Lieber, *Nature* **1999**, 399, 48-51.

22. G.K. Mor, K. Shankar, M. Paulose, O.K. Varghese, C.A. Grimes, *Nano Lett.* **2006**, 6, 215-218.

23. A.J. Frank, N. Kopidakis, J. van de Lagemaat, *Coord. Chem. Rev.* **2004**, 248, 1165-1179.

24. M. Paulose, G.K. Mor, O.K. Varghese, K. Shankar, C.A. Grimes, *J. Photochem. Photobi. A: Chem.* **2006**, 178, 8-15.

25. E.C. Scher, L. Manna, A.P. Alivisatos, *Phil. Trans. R. Soc. Lond.* **2003**,361, 241-255.

26. L. Manna, E.C. Scher, A.P. Alivisatos, *J. Amer. Chem. Soc.* **2000**, 122, 12700-12706.

27. L. Vayssieres, *Adv. Mater.* **2003**, 15, 464-466.

28. L. Vayssieres, M. Graetzel, *Angew. Chem.* **2004**, 43, 3666-3670.

29. L. Vayssieres, K. Keis, S.E. Lindquist, A. Hagfeldt, *J. Phys. Chem. B* **2001**, 105, 3350-3352.

30. Y. Li, F. Qian, S. Gradecak, Y. Wu, H. Yan, H. Yan, D.A. Blom, C.M. Lieber, *Nano Lett.* **2006**, 6, 1468-1473.

31. S. Gradecak, F. Qian, Y. Li, H.G. Park, C.M. Lieber, *Appl. Phys. Lett.* **2005**, 87, 17, 173111.

32. T. Kuykendall, P. Ulrich, S. Aloni, P.D. Yang, *Nature Mater.* **2007**, 6, 951-956.

33. D.A. Boyd, L. Greengard, M. Brongersma, M.Y. El-Naggar, D.G. Goodwin, Nano *Lett.* **2006**, 6, 2592-2597.

34. J.D. Driskell, Y. Liu, S.B. Chaney, X.J. Tang, Y.P. Zhao, R.A. Dluhy, *J. Phys. Chem. C* **2008**, 112, 895-901.

35. W. Smith, Z.Y. Zhang, Y.P. Zhao, *J. Vac. Sci. Tech. B* **2007**, 25, 1875-1881.

36. Y.P. He, J.X. Fu, Y. Zhang, Y.P. Zhao, L.J. Zhang, A.L. Xia, J.W. Cai, *Small* **2007**, 3, 153-160.

37. Y.P. Zhao, D.X. Ye, G.C. Wang, T.M. Lu, *Nano Lett.* **2002**, 2, 351-354.

38. A.C. van Popta, J. Cheng, J.C. Sit, M.J. Brett, *J. Appl. Phys.* **2007**, 102, 1, 013517.

39. M.J. Colgan, B. Djurfors, D.G. Ivey, M.J. Brett, *Thin Solid Films* **2004**, 466, 92-96.

40. A.C. van Popta, J.C. Sit, M.J. Brett, *Appl. Opt.* **2004**, 43, 3632-3639.

41. M. Suzuki, T. Ito, Y. Taga, *Appl. Phys. Lett.* **2001**, 78, 3968-3970.

42. O. Zywitzki, T. Modes, P. Frach, D. Glöss, *Surface & Coatings Technology*, **202**, 2488~2493 (2008)

43. Y.-P. He, Z.-Y. Zhang, Y.-P. Zhao, *Journal of Vacuum Science and Technology B* **26**, 1350 (2008)

44. W. Smith, Y.-P. Zhao, *Journal of Physical Chemistry C*, **112**, 19635 (2008)

45. T. Karabacak, J.P. Singh, Y.-P. Zhao, G.-C. Wang, T.-M. Lu, *Physical Review B*, **68**, 125408 (2003)

46. Y. P. He, Z. Y. Wu, L. M. Fu, C. R. Li, Y. M. Miao, L. Cao, H. M. Fan, B. S. Zou, *Chem. Mater*. **15**, 4039 (2003)

47. A. Mills, J. Wang, *Journal of Photochemistry and Photobiology A: Chemistry*, **127**, 123 (1999)

48. A. Houas, H. Lachheb, M. Ksibi, E. Elaloui, C. Guillard, J.-M. Herrmann, *Applied Catalysis B: Environmental* **31**, 145 (2001)

49. J.P.S. Valente, P.M. Padilla, A.O. Florentino, *Chemosphere*, **64** 1128 (2006)

50. J.-Q. Chen, D. Wang, M.-X. Zhu, C.-J. Gao, *Desalination*, **207** 87 (2007)

51. A.F. Caliman, C. Cojocaru, A. Antoniadis, I. Poulis, *J. Hazard. Mater.*, **144**, 265 (2007)

52. H. Ted Chang, N.-M. Wu, F. Zhu, *Wat. Res.*, **34**, 407 (2000)

53. I. Tinoco, K. Sauer, J. Wang, J. Puglisi, *Physical Chemistry : Principles and Applications in Biological Sciences*. (Upper Saddle River, New Jersey : Prentice Hall, 2002) 619.

54. J. H. Chen and G. H. Lu, *Nanotechnology* 17, 2891, (2006)

55. W. Smith, W. Ingram, Y.-P. Zhao, *Chemical Physics Letters***, 479**, 270 (2009)

56. J. Tang, Z. Zou, J. Yin, J. Ye, *Chemical Physics Letters* **382**, 175 (2003)

57. T. Ohno, M. Akiyoshi, T. Umebayashi, K. Asai, T. Mitsui, M. Matsumura, *Applied Catalysis A* **265**, 115 (2004)

58. Y. Li, M. Ma, X. Wang, G. Chen, *Catalysis Communications* **10**, 1985 (2009)

59. J. Sa, M. Fernandez-Garcia, J.A. Anderson, *Catal. Commun.* **2008**, *9*, (1991)

60. H. Tada, K. Teranishi, Y.-I. Inubushi, S. Ito, *Langmuir* **16**, 3304 (2000)

61. Y.-C. Lin, C.-H. Lin, *Environmental Progress* **27**, 496 (2008)

62. T. Hirakawa, P. Kamat, *Journal of the American Chemical Society*, **127**, 3928 (2005)

63. D. Wang, J. Zhao, B. Chen, C. Zhu, *Journal of Physics: Condensed Matter* **20**, 085212 (2008)

64. T. Ohsaka, F. Izumi, Y. Fujiki, *Journal of Raman Spectroscopy* **7**, 321 (1978)

65. K. Gao, *Physica Status Solidi B* **244**, 2597 (2007)

66. K.J. Lethy, D. Beena, R. Vinod Kumar, V.P. Mahadevan Pillai, V. Ganesan, V. Sathe, *Applied Surface Science* **254**, 2369 (2008)

67. Y.P. He, Y.P Zhao, *Journal of Physical Chemistry C* **112**, 61 (2007)

68. H. Irie, H. Mori, K. Hashimoto, *Vacuum* **74**, 625 (2004)

69. S. Higashimoto, Y. Ushiroda, M. Azuma, *Top. Catal.* **47**, 148 (2008)

70. S. Higashimoto, N. Kitahata, K. Mori, M. Azuma, *Catalysis Letters* **101**, 49 (2004)

71. H. Xu, G. Vanamu, Z. Nie, H. Konishi, R. Yeredla, J. Phillips, Y. Wang, *Journal of Nanomaterials* **2**, 1 (2006)

72. J. Sa, M. Fernandez-Garcia, J.A. Anderson, *Catalysis Communications* **9**, 1991 (2008)

73. C. Shifu, C. Lei, G. Shen, C. Gengyu, *Powder Technology* **160**, 198 (2005)

74. A.M. Salem, Y.A. El-Gendy, G.B. Sakr, W.Z. Soliman, *J. Phys. D: Appl. Phys.* **41** (2008) 025311

75. J.I. Pankove, *Optical Processes in Semiconductors*, Prentice-Hall, Englewood Cliffs, NJ 1971

76. K.S. Ahn, S. Shet, T. Deutsch, C.S. Jiang, Y.F. Yan, M. Al-Jassim,J. Turner, *J. Power Sources* **2008,** 176, 1, 387-392.

77. F. Oba, A. Togo, I. Tanaka, J. Paier, G. Kresse, *Phys. Rev. B* **2008,** 77, 24, 245202.

78. V. Ischenko, S. Polarz, D. Grote, V. Stavarache, K. Fink, M. Driess, *Adv. Funct. Mater.* **2005,** 15, 12, 1945-1954.

79. K.S. Ahn, Y.F. Yan, S.H. Lee, T. Deutsch, J. Turner, C.E. Tracy, C.L. Perkins, M. Al-Jassim, *J. Electrochem. Soc.* **2007**, 154, B956-B959.

80. C.F. Windisch, G.J. Exarhos, *J. Vac. Sci. Technol.,A.* **2000,** 18, 4, 1677-1680.

81. Hagfeldt, A.; Gratzel, M., Light-Induced Redox Reactions In Nanocrystalline Systems. *Chemical Reviews* **1995,** 95, 1, 49-68.

82. F. Fabregat-Santiago, G. Garcia-Belmonte, J. Bisquert, P. Bogdanoff, A. Zaban *J. Electrochem. Soc.* **2003,** 150, 6, E293-E298.

83. Schottky, W., *Z. Phys.* **1942,** 118, 539.

84. H.L. Wang, T. Lindgren, J.J. He, A. Hagfeldt, S.E. Lindquist, *J. Phys. Chem. B* **2000,** 104, 24, 5686-5696.

85. B. Oregan, M. Gratzel, *Nature* **1991,** 353, 6346, 737-740.

86. T. Bak, J. Nowotny, M. Rekas, C.C. Sorrell, *Int. J. Hydrogen Energy* **2002**, 27, 10, 991-1022.

87. R. Memming, *Semiconductor Electrochemistry* Weinheim, Wiley-VCH, **2001**.pp. 41-43

88. J.E. Kroeze, T.J. Savenije, J.M. Warman, *J. Amer. Chem. Soc.* **2004**, 126, 7608-7618.

89. G. Wang, Q. Wang, W. Lu, J.H. Li, *J. Phys. Chem. B* **2006**, 110, 22029-22034.

90. R. Beranek, H. Tsuchiya, T. Sugishima, J.M. Macak, L. Taviera, S. Fujimoto, H. Kisch, P. Schmuki, *Appl. Phys. Lett.* **2005**, 87, 24, 243114.

APPENDIX A

NOVEL ZNO NANOSTRUCTURES FABRICATED BY PLD, OAD, AND GLAD FOR PHOTOELECTROCHEMICAL WATER SPLITTING

A.1.1 ZnO Nanostructured Photoanodes

Photoelectrochemical cells based on traditional and nanostructured ZnO thin films are investigated for hydrogen generation from water splitting**.** The three ZnO electrodes were deposited by two methods, pulsed laser deposition (PLD) and electron beam evaporation. The structures that were fabricated by pulsed laser deposition were a traditional thin film and an oblique angle deposition thin film, while the glancing angle deposition sample was made by electron beam deposition. Pulsed laser deposition is based on a target material being ablated by high energy laser pulses in an ultra high vacuum or in a controlled gas environment. The resulting adatom plume subsequently deposits material onto the substrate of choice, perpendicular to the adatom stream (Figure A.1). The oblique angle and glancing angle deposition methods are based on a physical vapor deposition technique and are implemented by positioning the substrate at a large angle with respect to the incident vapor flux of the evaporated material. The vapors initially randomly nucleate on the surface of the substrate, and a so-called geometric shadowing effect helps the tall islands to grow taller, thus forming a porous structure.

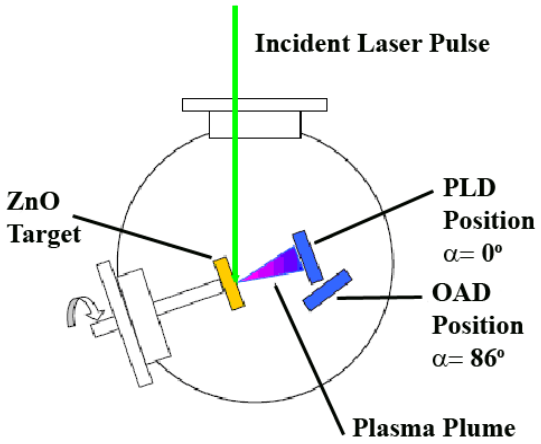

Figure A.1 This general illustration depicts the process by which pulsed laser deposition, oblique angle deposition and glancing angle deposition is performed. An incident pulsed laser (Nd:YAG) ablates a target material, which in turn creates an adatom plume which deposits onto a substrate at an angle normal to the substrate (α= 0º) for pulsed laser deposition. During oblique angle deposition the substrate is turned to α= 86º which allows for a shadowing effect to occur. Glancing angle deposition samples were produced with an electron beam as the ablation tool, with a substrate angle of α= 86º, and also a rotation of the substrate at 0.5 revolutions/minute.

For oblique angle deposition, the substrate remains fixed at a large angle, and the shadowing effect builds a porous nanofishscale structure. For glancing angle deposition, the substrate is rotated azimuthally with a constant speed, and an even more porous nanostructure is formed. For the pulsed laser deposition and oblique angle deposition thin films, ZnO (99.99%, Alfa Aesar) targets were initially prepared by pressing ZnO powder into disks approximately 3cm in diameter and 1 cm thick under ~10,000 psi by a hydraulic press. The pellets were then annealed in air at 1000 ºC for 2 hours in a furnace. The hardened pellets were then stuck with silver paste to the target carousel inside the pulsed laser deposition/oblique angle deposition chamber. Opposite the ZnO target, we placed several substrates, and then evacuated the chamber to a base pressure of ~10^{-7} Torr. For pulsed laser deposition experiments, an Nd:YAG laser (Spectra Physics Mountain View, CA) was used at a wavelength of 355 nm, with an average power of ~4.76 Watts and a deposition time of 2 hours. The incident laser beam was at

a 45º angle with respect the ZnO target plane. During deposition, an O_2 pressure of 6.3×10^{-3} Torr was attained in the chamber. The substrates used were Si wafers (100), glass, and FTO conducting substrates. The FTO substrates were used for photoelectrochemical characterization. The resulting plasma plume ejected off the ZnO targets was deposited on the substrates adjacent to the target. For the pulsed laser deposition thin films, the substrates were positioned perpendicular to the evaporation plume. For the oblique angle deposition thin films, the substrates were positioned 86^o from the evaporation plume.

The glancing angle deposition samples were fabricated in a custom-built electron beam deposition system. The source materials used to deposit were pre-made hardened pellets of ZnO (99.9%, Alfa Aesar) with no other gases present in the chamber during depositions, and chamber background pressure was at $1\text{-}2\times10^{-6}$ Torr. For the glancing angle deposition, the substrate was positioned 86° from the vapor incident direction and the substrate was also rotated azimuthally at a constant rate of 0.5 rev/second. The growth rate and thickness of the deposition were both monitored by a quartz crystal microbalance (QCM) facing the vapor flux direction directly. The deposition rate was fixed at 0.4 nm/s. All of the pulsed laser deposition, oblique angle, and glancing angle deposition samples were annealed at 550 °C in open air conditions with a Leister heat gun (Switzerland, CH-6056) prior to various experiments.

A.2.1 Results and Discussion

The crystalline structure of the ZnO PEC cells depends on the deposition technique and annealing process. For the PLD ZnO thin films on glass slides, the as-deposited XRD pattern has one diffraction peak at 34.4^o, which corresponds to (002) crystal phase of the ZnO wurtzite structure (Figure A.2 (a)). Overall, the appearance of only one diffraction peak of low intensity is

consistent with a mostly amorphous material. After annealing at 550 °C in open air conditions, four XRD peaks arise at 31.5°, 34.4°, 36.3° and 56.6° which are assigned to the (100), (002), (101) and (110) crystal facets, all representative of the ZnO zincite phase (wurtzite structure). Consequently, it is evident that the increase of diffraction peaks, along with the intensity of the (100) peak is a result of a phase transition from a largely amorphous state to a crystalline one. For the OAD ZnO nanoplatelet films on glass slides, both the as-deposited and annealed samples only have a single diffraction peak at 34.4 °, corresponding to the (002) crystal facet of ZnO (Figure A.2 (b)). However, the (002) peak for the annealed OAD nanoplatelet films have an increased intensity over that of the as-deposited sample and has a sharper peak profile. This feature reveals that the OAD nanoplatelet films, both as-deposited and annealed, have a crystal structure that is highly oriented. Contrarily, GLAD ZnO nanoparticle films have a drastically different XRD pattern, and have more crystal facets satisfying the Bragg requirements. Deposition of GLAD ZnO nanoparticle films were performed on fluorine-tin oxide (FTO) conducting substrates, thus representative FTO peaks are observed with the as-deposited samples. The major diffraction peaks at (100), (002), (101) and (110) are prominent with very sharp features after annealing at 550 °C (Figure A.2 (c)). Overall, the omnidirectional growth of the ZnO nanoparticles on the FTO substrate allows for a randomized orientation. The increased sharpness and intensity of the zincite crystal phase peaks is attributed to this larger number of ZnO nanocrystallites satisfying the Bragg requirements.

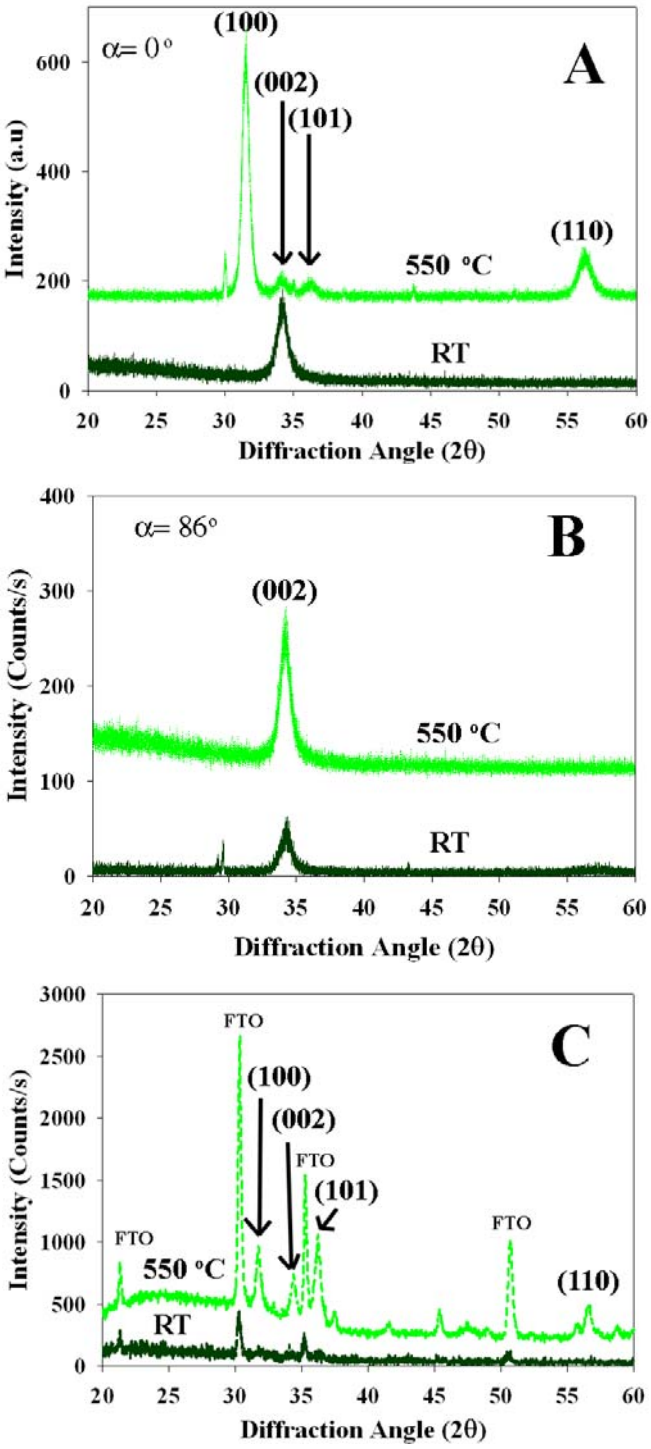

Figure A.2 XRD patterns of the as-deposited ZnO films at room temperature (RT) and after annealing at 550 ºC in open air conditions. **(A)** Pulsed laser deposition thin film, **(B)** oblique angle deposition film and **(C)** glancing angle deposition ZnO nanoparticle film deposited on FTO conducting substrates.

High resolution scanning electron microscopy (HRSEM) and SEM images detail the morphological differences of PLD thin film, OAD nanoplatelet and GLAD nanoparticle ZnO films. SEM images of ZnO thin films produced by PLD reveal the formation of a dense structure with grain sizes of ca. 200 nm (Figure A.3 (a)). A portion of the thin film was displaced and allowed for a glimpse into the nature of the interface morphology between the FTO conducting substrate and ZnO. Due to the rough topography of the FTO, the ZnO then replicates that texture, and produces a templated semiconductor-substrate interface (Figure A.3 (a) and (b)). SEM images at a sample angle tilt of 25º reveal the dense nature of the film, and also the underlying FTO substrate (Figure A.3 (b)). ZnO thin films produced by PLD were found to be 500 nm in thickness (not shown). In contrast to the PLD samples, the directed growth of OAD produces an overlaid ensemble of oval shaped nanoplatelets forming a fishscale like pattern (Figure A.3 (c)). Individual ZnO nanoplatelets were ca. 950 nm by 450 nm, and were made up of agglomerated ZnO crystallites with an increased porosity due to the shadowing growth mechanism of the OAD technique (Figure A.3 (d)). OAD ZnO nanoplatelet films also had an average thickness of 500 nm measured via HRSEM images (not shown). Alternatively GLAD nanoparticle films produced by electron beam deposition, were an interconnected network of 15-40 nm diameter nanoparticles with a high level of nanoporosity (Figure A.3 (e) and (f)). The interconnected ensemble produced a very contoured surface with areas of stalagmite like features and a high surface-to-volume ratio. GLAD films that were examined had a thickness of 500 nm as well to allow for comparative PEC studies.

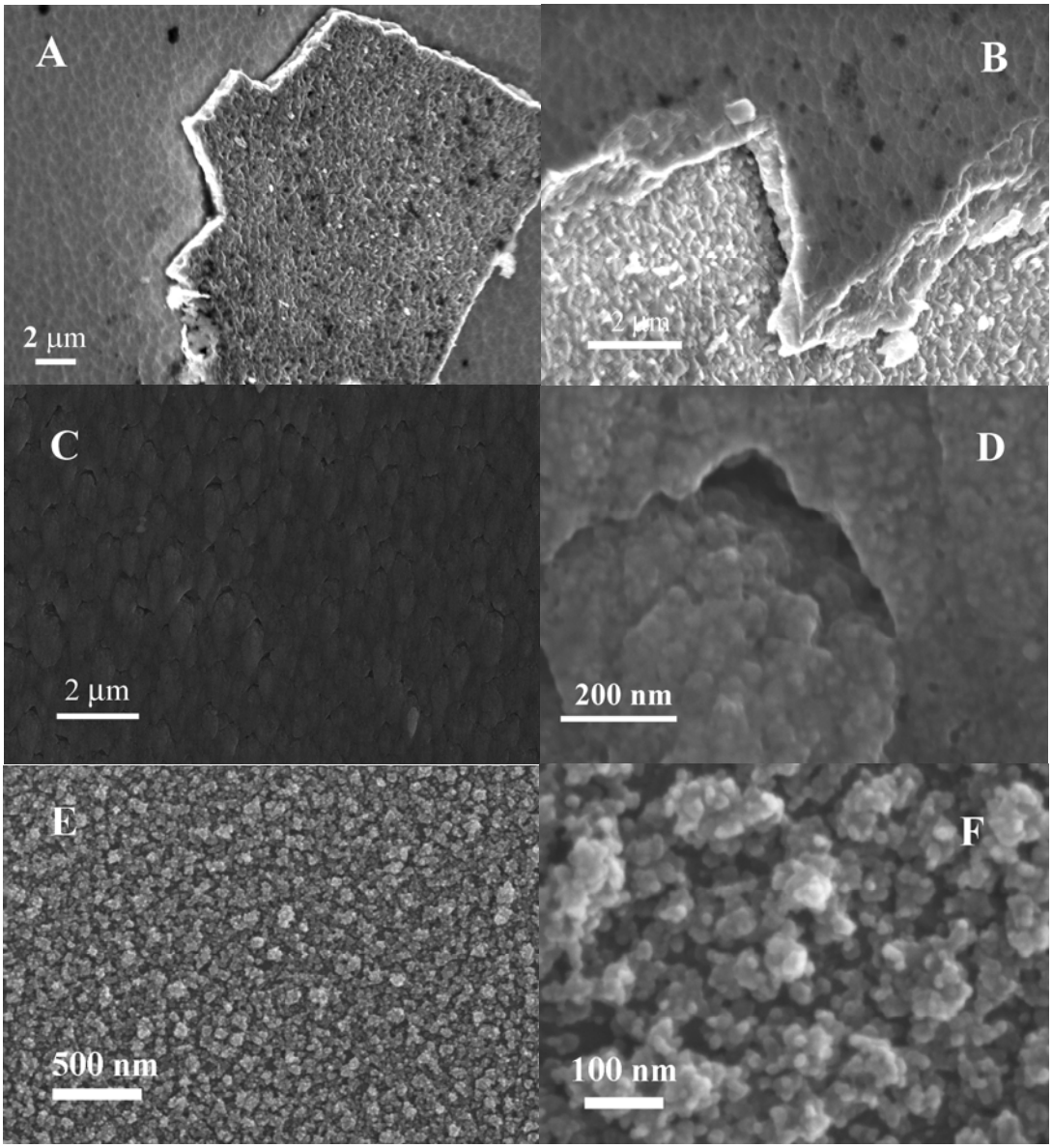

Figure A.3 SEM/HRSEM images of the collection of pulsed laser deposition, oblique angle deposition and glancing angle deposition ZnO thin film samples deposited on FTO conducting substrates. **(A)** and **(B)** SEM images of pulsed laser deposition ZnO thin films on FTO conducting. **(C)** and **(D)** The oblique angle deposition ZnO nanoplatelet thin films are observed to have increased porosity due to the geometric shadowing effect. **(E) and (F)** SEM images of the ZnO nanoparticle (NP) thin films produced by glancing angle deposition reveal an increase in nanporosity on the FTO substrate.

Depending upon the deposition technique utilized, the state of coloration of the films varied before and after annealing. PLD thin films, for instance, were a transparent brownish-yellow tone after their deposition at room temperature (RT). Intrinsic ZnO has a bulk bandgap of 3.3 eV, and should therefore be optically colorless.[76] However, the level of defects allows for weakly absorbing states typically due to Zn interstitial sites and oxygen vacancies.[77,78] UV-visible absorption spectra of as-deposited PLD ZnO thin films had a red-shifted optical transition out to ca. 680 nm, a gradual increase throughout the visible until a plateau at 400 nm, and a continued absorptive increase in the UV region (Figure A.4 (a)). This optical response was also observed in incident-photon-to-current-conversion-efficiency (IPCE) action spectra, which will be discussed later. After annealing of the PLD thin films at 550 ºC, the overall coloration of the films remained a transparent brownish-yellow hue. The absorption spectra changed slightly with a similar increase starting in the 650 nm range and gradually increasing until 400 nm, wherein a steep increase due to photoexcitation above the intrinsic bandgap occurred (Figure A.4 (b)). Conclusively, it is apparent that PLD thin films were defect heavy, and due to the dense nature of the films, defects were not able to anneal out at 550 ºC in open air conditions.

ZnO OAD nanoplatelet films were colorless, with a slight opaqueness to them after deposition at RT. Their optical absorption spectra represented this well with little absorption throughout the visible region, and a drastic increase after 400 nm when bandgap photoexcitation was reached (Figure A.4 (a)). Subsequent annealing at 550 ºC showed little overall change to the ZnO nanoplatelets appearance or the UV-vis spectrum (Figure A.4 (b)). After annealing at 550 ºC, no absorbance is observed in the visible wavelengths, with an increased absorptive profile after 380 nm. At 350 nm there is an observed plateau of absorbance, and a sharp increase until 300 nm.

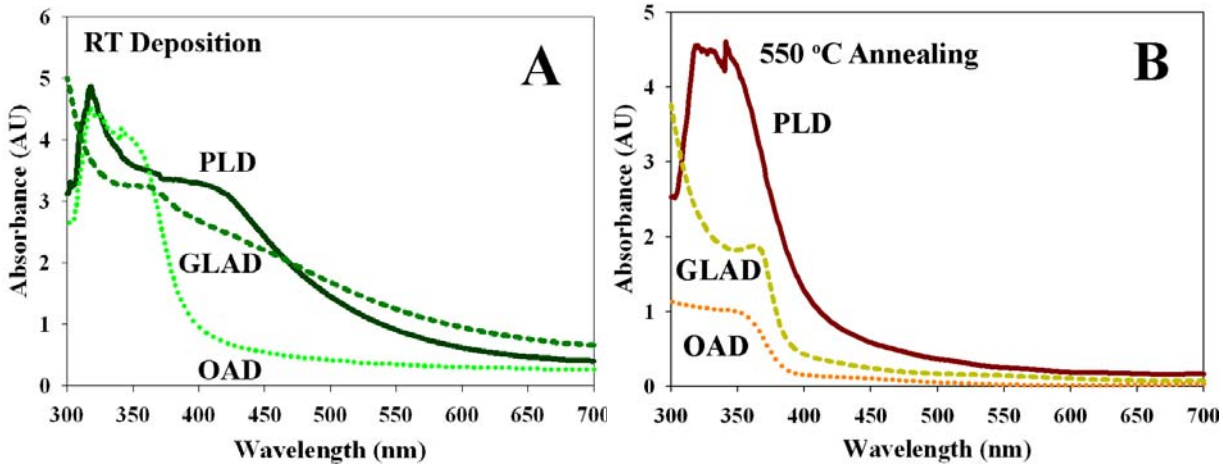

Figure A.4 UV-visible absorption spectra of the **(A)** as-deposited and **(B)** annealed ZnO on FTO substrates by pulsed laser deposition, oblique angle deposition and glancing angle deposition techniques.

The behavior of the ZnO GLAD films was different than both the PLD thin films and OAD nanoplatelet films. At RT deposition, the GLAD nanoparticle films were a dark brown tone and optically transparent, very similar to the appearance of the PLD thin films (Figure A.5 (a)). The as-deposited GLAD films have absorption throughout the visible starting at 700 nm, and continue to increase until a shoulder near 360 nm (Figure A.5 (a)). At elevated annealing temperatures from 100-400 ºC the ZnO nanoparticle films retained their dark brown appearance, indicative of a defect heavy ZnO (Figure A.5 (b)). In stark contrast to both PLD and OAD films, the GLAD nanoparticle films became optically transparent and colorless at a threshold annealing temperature of 550 ºC within a matter of thirty seconds (Figure A.5 (c)). After annealing, the UV-vis absorbance of the ZnO GLAD films blue-shifted drastically to an absorption onset of ca. 400 nm with a peak residing at 360 nm (Figure A.4 (b)). The photophysical evidence for the ZnO GLAD nanoparticle films unequivocally shows that defects introduced during the deposition process at RT were removed at an annealing temperature of 550 ºC. We believe this change in the defect content of the nanoparticle films was due to the overall nanoporosity of the

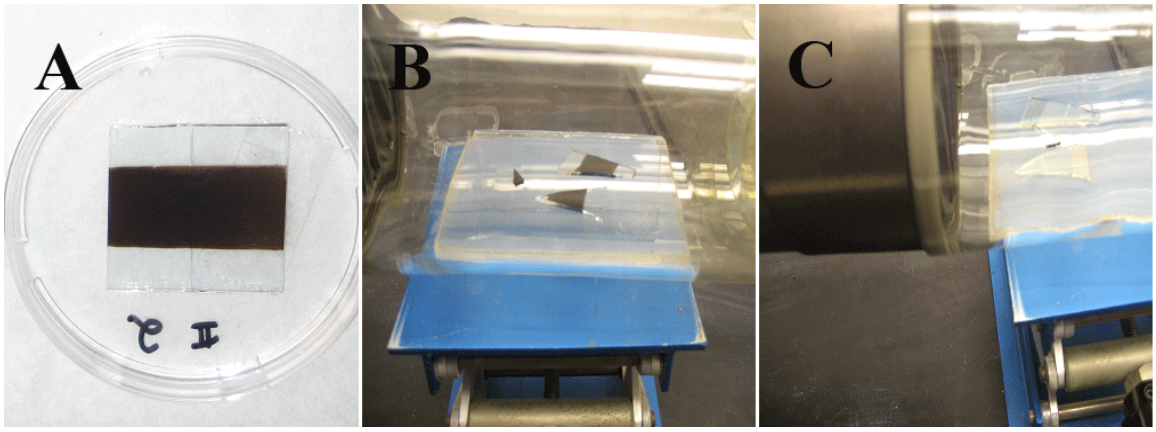

Figure A.5 During the annealing process a series of photographs are taken to show the phase transition of the glancing angle deposition samples from RT **(A)**, 400 ºC **(B)** and 550 ºC **(C)** in a Leister heat gun. The brownish tone of the ZnO glancing angle deposition samples remain up until 550 ºC wherein they become colorless within about 30 seconds when placed in close proximity to the heating element **(C)**.

film in conjunction with the high surface-to-volume ratio of the 15-40 nm nanoparticles. Oxygen vacancies are the most likely cause for the mid-bandgap optical transitions, and their subsequent removal at elevated temperatures is apparent in open air conditions.

A.2.2 Photoresponse and Photoelectochemical Water Splitting

The PEC results demonstrate successful hydrogen generation based on photocurrent response from nanostructured ZnO films with different morphologies and defect levels. At high current density, hydrogen generation can be visualized in terms of gas bubble formation on the cathode (Pt coil) and simultaneously oxygen bubble formation on the active photoanode. The hydrogen generation efficiency clearly depends on the film properties, including porosity, morphology, defect density, and optical absorption spectrum. All samples were fashioned into PEC cells after annealing at 550 ºC to increase the stability of the PEC cells and increase charge transport properties. Fundamental impedance properties were investigated to deduce properties such as the flatband potential (V_{FB}), donor density (N_d), and space charge layer (W).

Electrochemical impedance measurements were performed in dark conditions in 0.5M $NaClO_4$, with phosphate buffer to pH=7.4 and a Ag/AgCl reference electrode. Impedance measurements allow for the derivation of capacitance at the semiconductor-electrolyte-interface (SEI) and is described by a Mott-Schottky plot ($1/C^2$ vs. V). The Mott-Schottky equation is described by

$$\frac{1}{C^2} = \left(\frac{2}{e_o \varepsilon \varepsilon_o N_d} \right) \left[(V - V_{FB}) - \frac{kT}{e_o} \right] \quad \text{(A.1)}$$

wherein e_o is the fundamental charge constant, ε is the dielectric constant of ZnO (8.5),[79] ε_o is the permittivity of vacuum, N_d is the donor density, V is the electrode applied potential, V_{FB} is the flatband potential, and $\frac{kT}{e_o}$ is a temperature dependent correction term. Flatband potentials were found by the extrapolation of the linear portion of $1/C^2$ vs. V to the x-axis (Figure A.5). ZnO PLD, OAD and GLAD PEC cells had V_{FB} of -0.29V, -0.28V and +0.20V, respectively. Both the PLD and OAD V_{FB} are in the range found for sputtered and sol gel ZnO thin films that had V_{FB} values in the range of -0.3 to -0.4 V.[80] The anodic shift of the V_{FB} to +0.20V in the ZnO GLAD nanoparticle PEC cells is due to the depletion of charge from the 15-40 nm nanoparticles. The depletion of charge can be understood by the theoretical description of the potential drop ($\Delta\phi_o$) across small particles and a change of band bending properties.[81] This phenomenon can occur when the particle radius and space charge layer (W) are of similar size.[81] Theoretical and experimental Mott-Schottky studies of nanocrystalline TiO_2 SEI on FTO substrates, have also described anodic shifts of V_{FB} position as a function of substrate surface coverage.[82] From the Mott-Schottky plots, one is also able to calculate the donor density N_d based on the slope via the equation,

$$N_d = -\left(\frac{2}{e\varepsilon_o\varepsilon}\right)\left(\frac{d(1/C^2)}{dV}\right)^{-1} \quad . \tag{A.2}$$

In our study we found donor densities for ZnO PLD, OAD and GLAD PEC cells to be 3.2×10^{16} cm^{-3}, 2.8×10^{17} cm^{-3} and 1.4×10^{16} cm^{-3}, respectively. Previous studies on magnetron sputtered ZnO films by Ahn *et al.* reported N_d values of 4.6×10^{16} cm^{-3} and 1.8×10^{16} cm^{-3} for unannealed and annealed ZnO, respectively.[79] Unintuitively, the donor densities of PLD PEC cells were lower than the OAD nanoplatelet cells, even though the PLD cells were a brownish-yellow hue and the OAD cells had an opaque colorless appearance. The brownish-yellow hue is indicative of a higher density of defects for the PLD thin films. Coincidentally, the brown ZnO GLAD nanoparticle films became colorless after annealing, and in turn had a lower donor density (compared to both PLD and OAD films). We believe the high surface-to-volume ratio and nanoporosity aided in the removal of oxygen vacancies and Zn interstitials.

An important aspect of the SEI is the phenomenon of band bending and the formation of a space charge layer (Schottky barrier).[81,83] In the case of ZnO, an n-type semiconductor, a depletion layer will develop under applied anodic conditions. Depletion layer characteristics are typically described as the removal of the majority charge carrier (electrons) from the SEI, and the subsequent localization of holes at the SEI. The space charge layer is derived from the Mott-Schottky plot through the expression,

$$W = \left[\frac{2\varepsilon\varepsilon_o(V - V_{FB})}{e_o N_d}\right]^{1/2} \quad , \tag{A.3}$$

wherein V is the applied potential at the working semiconductor electrode.[83] At an applied potential (V) of +1.0 V the calculated space charge layers were found to be 195 nm, 65 nm and 235 nm for the PLD, OAD and GLAD PEC cells, respectively (Figure A.6). When the space

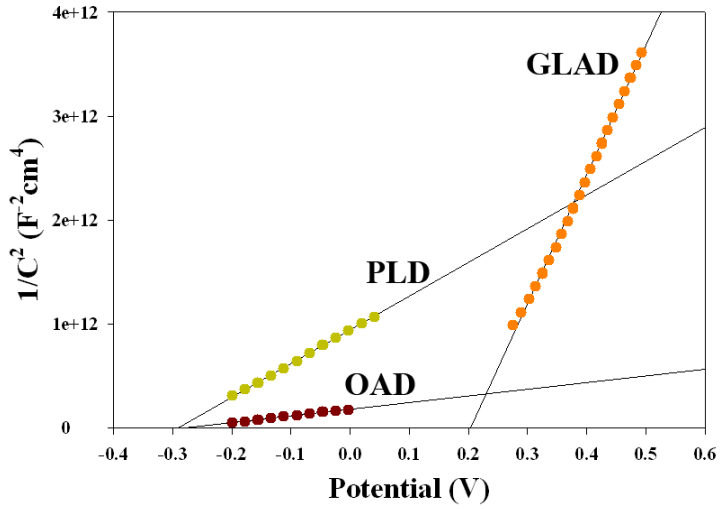

Figure A.6 Mott-Schottky plots of the three samples show changes of flatband potential (V_{FB}), donor density (N_D), and space charge layer (W) based on deposition technique. Pulsed laser deposition, oblique angle deposition and glancing angle deposition ZnO samples have V_{FB} of -0.29 V, -0.28 V and +0.20 V, N_D of 3.2×10^{16} cm^{-3}, 2.8×10^{17} cm^{-3} and 1.4×10^{16} cm^{-3} and W of 165 nm, 95 nm and 235 nm, respectively. Porosity, semiconductor electrolyte interaction and defect density all play critical roles in the varying degrees for all three parameters.

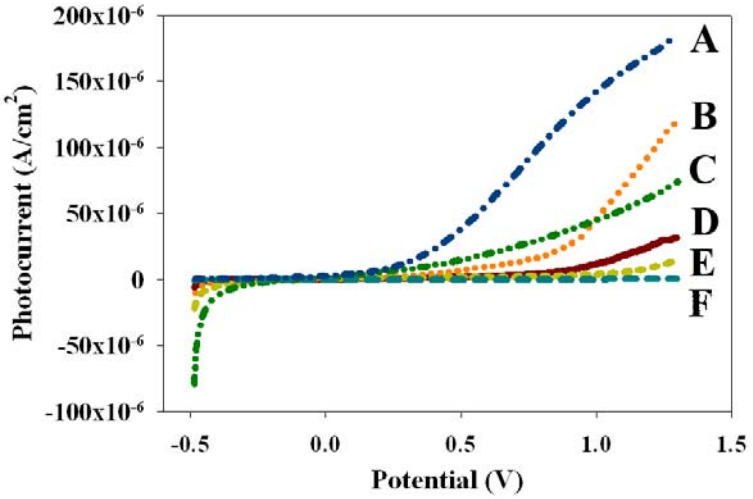

Figure A.7 Linear sweep voltammagrams in the dark and 100 mW/cm^2 (AM 1.5) are performed in a 0.5 M NaClO4 solution buffered to pH= 7.4. Photocurrent measurements under AM 1.5 (100 mW/cm^2) for glancing angle deposition **(A)**, pulsed laser deposition **(B)**, and oblique angle deposition **(C)** all show significant photoresponse, but the glancing angle deposition nanoparticle samples have superior characteristics with a photocurrent of 142 $\mu A/cm^2$ at 1.0 V in comparison to the pulsed laser deposition and oblique angle deposition samples. The pulsed laser deposition **(D)** and oblique angle deposition **(E)** samples show increased dark current under the bias of +0.8 V to +1.1 V while glancing angle deposition **(F)** sample shows no discernible dark current.

charge layer is smaller than the film thickness (500 nm), we expect to see no limiting photocurrents, and this is what was observed (Figure A.6).[35, 36] Linear sweep voltammagrams measurements under dark and illuminated (100mW/cm^2) conditions were found to be highly dependent on the deposition technique used. Firstly, the ZnO PLD cells under dark conditions showed a marked increase in dark current at ~+0.8 V, which continued to increase linearly up to +1.3 V (Figure A.7). The ZnO PLD thin films had by far the largest background current, which may be attributed to the level of defects in the dense film, and incomplete coverage of the FTO conducting substrate. Photocurrent was generated in the PLD thin film at ca. +0.4 V, where it increased gradually until +0.8 V, and then steeply increased until +1.3 V. Initial photocurrent (I_{PH}) generation beginning at +0.69 V anodic of the flatband potential is an indication of photogenerated electron-hole recombination, and an under developed space charge region.[84] A I_{PH} of 45.9 μA/cm^2 was in turn generated at an applied potential of +1.0 V after which a space charge layer of 195 nm was formed. The I_{PH} continued to increase after +1.0 V and there was no limiting photocurrent.

ZnO OAD nanoplatelet PEC cells had a reduced dark current until +1.0 V wherein the electrolytic oxidation of water occurs. Under illumination at 100 mW/cm^2 (Air Mass (AM) 1.5), I_{PH} was initially generated at +0.25 V, and increased near linearly up to a I_{PH} of 44.9 μA/cm^2 at +1.0V (Figure A.7). Efficient collection of electrons at the backcontact occurred at +0.58 V anodic of V_{FB}, and is due to an increased microporosity and semiconductor-electrolyte interaction in the ZnO nanoplatelet system. There was no limiting photocurrent in the range of anodic potentials examined for the OAD cells.

The ZnO nanoparticle system produced by GLAD was superior in its overall PEC properties with a small background current ($\leq$ 0.25 μA/cm^2 at 1.0 V) and immediate I_{PH}

generation at +0.2 V, indicative of a more efficient diffusion of carriers through the nanoparticles to the back-contact (Figure A.7). With a larger space charge layer of 235 nm, electron-hole recombination was reduced and a photocurrent of 142.5 μA/cm^2 at +1.0 V was observed. The hopping mechanism, inherently used to describe interconnected nanoparticle systems such as the Graetzel cell, allowed for greater carrier mobility.[85] The increased surface-to-volume ratio of the 15-40 nm ZnO nanoparticles along with the decreased number of defects after annealing at 550 ºC aided the PEC performance as well.

Incident-photon-to-current-conversion efficiency (IPCE) measurements were calculated based upon the equation

$$IPCE = \frac{1240 * I_{PH}}{\lambda * J_{LIGHT}} \quad , \tag{A.4}$$

where I_{PH} is the photocurrent in μA/cm^2, λ is the incident wavelength of light and J_{LIGHT} is the incident irradiance in μW/cm^2. Overall, the three systems behaved in a similar manner with the PLD thin film having a weak visible response out to 640 nm (Figure A.8). The PLD cells had an increased IPCE% after 400 nm, but then dropped from 9.7 % at 360 nm to 2.3 % at 350 nm. The OAD and GLAD PEC cells behaved more traditionally with no visible photoresponse, and a steep increase after 400 nm and an IPCE % at 350 nm of 12.9 % and 16.0 %, respectively (Figure A.8).

Water splitting was observed at an applied potential of +1.0 V for the ZnO PLD, OAD and GLAD PEC cells resulting in a photon-to-hydrogen efficiency of 0.1 %, 0.2 % and 0.6%, respectively. The photon-to-hydrogen efficiency is calculated via the expression

$$\eta_c = \frac{I(1.23 - V_{BIAS})}{J_{LIGHT}} \quad , \tag{A.5}$$

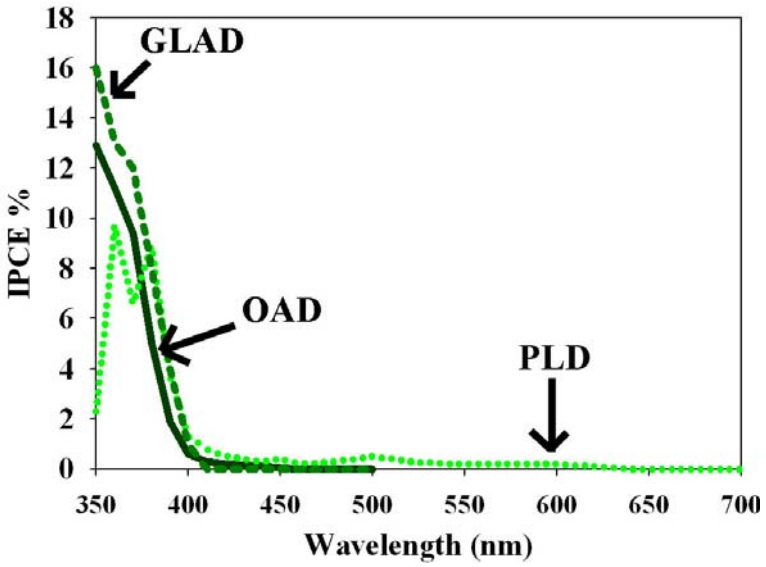

Figure A.8 Incident-photo-to-current-conversion efficiency (IPCE) action spectra at an applied potential of 0.5 V for the pulsed laser deposition (•••), oblique angle deposition (—) and glancing angle deposition (---) ZnO films show varied degrees of photoresponse.

wherein I is the photocurrent, V_{BIAS} is the applied external bias and J_{LIGHT} the incident light irradiance.[86] These reported values were obtained with a corrected J_{LIGHT} based on the spectral output of the Xe lamp system and absorbance profiles of the three separate PEC cells. The integrated spectral overlap of the Xe lamp in the UV is approximately 5%, as estimated from individual irradiance measurements made through the UV-visible spectrum at various wavelengths. The uncorrected, total measured irradiance during these measurements was a standard 100 mW/cm^2 or Air Mass 1.5 (AM 1.5). Therefore, 5 mW/cm^2 is used as the J_{LIGHT} for both OAD and GLAD cells. This correction was calculated because only UV radiation is actively absorbed by both samples as indicated by both UV-visible absorbance (Figure A.5) and IPCE % action spectra (Figure A.8). PLD thin films, with a weak extended visible absorption, had an increased corrected irradiance of 10 mW/cm^2. This increase reflects the inherent optical response that needs to be accounted for with PLD thin films (Figure A.5 and A.8). Losses

relating to reflection, absorption by the PEC experimental cell and electrolyte are neglected in the measurement of J_{LIGHT} in this study.

While the PLD thin films and OAD nanoplatelet cells showed consummate photon-to-hydrogen efficiencies of 0.1% and 0.2%, the GLAD nanoparticle system showed a three-fold increase to 0.6 %. This is attributed to increased nanoporosity of the ZnO GLAD films and increased semiconductor-electrolyte interaction that is beneficial to PEC performance and water splitting. Consequently, transport of photogenerated carriers in the GLAD nanoparticle PEC cells could be aided in part by a larger space charge region that promotes the separation of photogenerated electron/holes at the SEI. Increased I_{PH} seen in linear sweep voltammagrams and IPCE action spectra reveal that the interconnected nanoparticle system is superior for photogenerated charge transport. Possible routes to increase photoresponse and efficiency, especially in the visible, are the utilization of doping and quantum dot sensitization.

These PEC studies have shown that I_{PH} generation and hydrogen generation efficiency are a function of porosity, morphology and defect concentration based on deposition technique. The defect heavy ZnO PLD thin films showed extended photoresponse due to oxygen vacancies and Zn interstitials, compared to OAD and GLAD PEC cells. The GLAD and PLD also responded differently to annealing in terms of changes in the density of defects and coloration. The dependence on morphology, surface-to-volume ratio and defect level suggests the importance of controlling the nanostructures to tailor their fundamental properties for optimal hydrogen generation applications. Our study reinforces that charge transport via a hopping mechanism (diffusion) in nanoparticle based systems does aid in water splitting. Enhanced electron-hole

separation due to depletion layer formation is a critical player because of the large surface-to-volume ratio of the 15-40 nm ZnO interconnected nanoparticle network. Further studies developing various ranges of porosity and nanoparticle diameter can further optimize such a photoelectrochemical system in the immediate future.